

DETECTION OF CHEMICAL COMPOUNDS USING AMPLIFIED FIBER LOOP RING-DOWN SPECTROSCOPY

by

Jessica Litman

A thesis submitted to the Department of Chemistry

In conformity with the requirements for

the degree of Master of Science

Queen's University

Kingston, Ontario, Canada

(September, 2011)

Copyright ©Jessica Litman, 2011

Abstract

Cavity ring-down spectroscopy (CRDS) is an absorption spectroscopic technique. In CRDS the concentration of an analyte is determined by measuring the reduction in finesse of an optical cavity made from two highly reflective ($R > 99.9\%$) mirrors once a sample is introduced. Optical loss is traditionally determined from the exponential intensity decay of a short laser pulse that was injected into the cavity. This decay is the longest for an empty, high finesse cavity and is reduced when the sample absorbs or scatters light.

In this project, the optical cavity is made from fiber optic waveguides and the light source is a continuous wave (cw) diode laser. It is used to detect analytes such as acetylene, ammonia and other amines through their overtone absorption in the telecom region at 1500 nm. The experiment is done by increasing the ratio of desired loss (extinction caused by the sample), to undesirable loss (from the waveguide or solvents) through amplification of the ringdown signal using an erbium doped fiber amplifier (EDFA). The EDFA is inserted into a fiber-optic loop and its gain is increased above the lasing threshold. The gain of the, now lasing, fiber loop is "clamped" to a high and constant value, thereby removing unwanted gain fluctuations, and all losses in the loop are compensated for. If one now inserts a laser light pulse at the lasing wavelength of the loop it would circulate through the loop indefinitely, whereas a light pulse at a wavelength that is being absorbed by an analyte would experience a decrease with time at a rate that depends only on the magnitude of the sample absorption. By enclosing the sample gap with a gas cell both acetylene and ammonia have been detected down to ~ 25 ppm and ~ 5.9 Torr respectively. Subsequently, a 1% solution of aminotoluene was detected in an interrogation volume of 5.65 μL by having inserted a fiber with a hole drilled in it as the sample gap. At

present, the drilled fiber has been replaced with photonic crystal fiber such that small volumes of gases may be detected with a longer effective path length.

Acknowledgements

First and foremost I would like to thank my supervisor Professor Hans Peter Looock for his never faltering guidance and support throughout the past few years. I appreciate all the opportunities I was given to present my work at research symposia and for the chance to do research abroad. I am also grateful for his continuous insight and enthusiasm towards my project and for believing in me.

I am greatly indebted to Dr. Jack Barnes for being incredibly patient with me over the years, teaching about the basis of my project and the laboratory equipment we used, and finally for his help building the technical aspects of our project. Additionally, I would like to acknowledge Dr. Helen Waechter for her friendship and for sharing her knowledge about fibers and CRD with me. I wish to thank the other members of our group whose friendships I greatly appreciated: Dr. Wei Guo, Stephen Walker, Jeff Crouse, Klaus Bescherer, Piyumie Wickramasinghe, John Saunders, Marian Dreher, Adrienne Cheung, Grant Ongo and Bithun Sarkar.

I would also like to say a very special thank you to Annette Keys for being continuously awesome. As well as to my committee members Dr. Natalie Cann and Dr. Stephen Brown for their constructive input throughout the course of my degree.

In my final years spent in Kingston I was lucky to have become friends with Julia Van Drunen, Rebecca Holmberg and Victoria Bloom who were always there when I needed them and could always make me smile, even on the worst of days.

I would like to thank my brother Richard for the countless hours of entertainment his moving to Kingston provided me with - it was great to be in the same city with you. Valerie for being both my sister and best friend, you make me very proud. My parents for their continuous support, guidance and love - words cannot describe how grateful I am.

Finally, I would like to thank my grandparents for inspiring me to work hard and to be a better person, I love you very much.

Table of Contents

Abstract.....	ii
Acknowledgements.....	iv
Table of Contents.....	vi
List of Figures.....	viii
Chapter 1 Introduction and Literature Review.....	1
1.1 Beer-Lambert Law.....	3
1.2 Absorption spectroscopy.....	4
1.3 Cavity Ring-Down Spectroscopy.....	9
1.4 Continuous Wave - CRDS.....	17
1.5 Phase Shift - CRDS.....	19
1.6 Fiber Cavity Ring-Down Spectroscopy.....	28
1.6.1 Fiber Loop Ring-Down Spectroscopy.....	33
1.7 Amplified CRDS.....	40
Chapter 2 Theory.....	46
2.1 The Erbium Doped Fiber Amplifier.....	46
2.1.1 Dynamics of Optical Amplification.....	47
2.1.2 The Shape of the Spontaneous Emission Spectrum.....	51
2.2 Background relating to Hollow-Core Photonic Band-gap Fibers.....	53
2.2.1 Overview.....	53
2.2.2 Types of HC PBGs.....	57
2.3 Background of Acetylene.....	58
2.3.1 The Ro-Vibrational Acetylene Spectrum.....	58
2.3.2 Nuclear Spin Statistics of Acetylene.....	64
2.4 Background of Ammonia.....	68
2.4.1 Ammonia Ro-Vibrational Transitions.....	70
2.4.2 Determining the partial pressure of Ammonia in an ammonium hydroxide solution.....	76
Chapter 3 Experimental.....	78
3.1 Experimental Overview.....	78
3.2 The Gas Cell.....	83
3.3 Hollow-Core Photonic Band-Gap Fibers as Gas Sensors.....	86
3.4 Fiber with a Hole.....	88

3.5 Measurements	91
3.6 Equipment Used.....	93
Chapter 4 Results and Discussion.....	95
4.1 The Experimental Setup with the Gas Cell Interface.....	96
4.1.1 Optimization at 1550 nm.....	96
4.1.2 Optimization at 1530-1535 nm.....	98
4.1.3 Relaxation Oscillations	100
4.1.4 Detection of Acetylene	102
4.1.5 Detection of Ammonia.....	108
4.2 The Experimental Setup with the Hollow-Core Photonic Band-Gap Sensor	111
4.2.1 The Initial HC PBG Interface	111
4.2.2 The Second HC PBG Interface	114
4.3 The Experimental Setup with the Fiber with a Hole Interface.....	120
4.3.1 The Watch Glass Setup.....	121
4.3.2 The Teflon Trough Interface and Improvements	122
Chapter 5 Conclusion and Future Endeavours.....	124
5.1 The optical setup.....	124
5.2 The Gas Cell	127
5.3 The HC-PBG fiber Interface	128
5.4 The Fiber with a Hole Interface	130
5.5 Final comments.....	131
References.....	132

List of Figures

Figure 1. Schematic of a typical single pass absorption spectroscopy setup.....	6
Figure 2. Multipass absorption cells.....	8
Figure 3. Traditional optical cavity for pulsed CRDS.....	13
Figure 4. A common setup for CW CRDS.....	13
Figure 5. Exponential decay of pulsed laser light within a ring-down cavity.....	14
Figure 6. CRDS spectrum of the O ₂ $b(v=1)$ - $X(v=0)$ band taken with a one wavenumber bandwidth laser in a 60 cm long cavity.....	16
Figure 7. Experimental scheme of a phase-shift fiber loop ring-down experiment.....	21
Figure 8. Multiexponential decay of light injected into a 25.6 m multimode fiber loop at $\lambda=800$ nm.....	26
Figure 9. A linear fiber cavity formed by adding two mirror elements and a fiber ring cavity made by bending the fiber into a loop.....	30
Figure 10. Different types of sensor elements used in fiber cavity ring-down spectroscopy.....	32
Figure 11. Increase in the absorption path length compared to single pass absorption in microfluidic devices.....	35
Figure 12. A custom built interface used to direct liquid between fiber ends and to couple light from the light source into the loop.....	39
Figure 13. Amplified fiber loop ring-down cavity using an erbium doped fiber amplifier.....	44
Figure 14. 100 μ s ring-down trace in a gain-clamped fiber cavity when the fiber's lasing wavelength and the pulse's wavelength are near coincidence.....	44
Figure 15. The three level pumping scheme that an EDFA utilizes to produce spontaneous and stimulated emission.....	48
Figure 16. The spontaneous emission and lasing action spectrum produced by the EDFA used in our experiment.....	49
Figure 17. Light being guided in an optical fiber through total internal reflection.....	55
Figure 18. A cross-section of a HC PBG that guides light through the air filled core by periodic constructive interference of the light in the cladding.....	56
Figure 19. The molecular axis of acetylene, lying along the z coordinate.....	63
Figure 21. The P and R branches of the acetylene $\nu_1 + \nu_3$ combination band at 298 K.....	67
Figure 22. The assigned, unassigned and calculated $2\nu_3$ and $\nu_1 + \nu_3$ transitions for ammonia.....	74
Figure 23. Gain stabilization using a secondary lasing loop.....	79

Figure 24. The amplified two loop setup.....	81
Figure 25. A photo of the experimental setup.....	82
Figure 26. Side and top view of the stage.....	85
Figure 27. A photograph of the HC PBG used as the gas-sensing device in the current setup.....	87
Figure 28. HC PBG – SM fiber interface.....	87
Figure 29. A single mode fiber with a hole drilled in it.....	88
Figure 30. The fiber with a hole taped down onto a watch glass and the Teflon trough with side grooves to thread the fiber through.....	90
Figure 32. Ring-up trace of the outer-loop.....	97
Figure 33. An Allan Variance plot - this shows the stability of the setup over time.....	99
Figure 34. A relaxation oscillation seen in the outer loop.....	101
Figure 35. Spectrum of the acetylene P(11) – P(15) rotational lines on the $\nu_1+\nu_3$ combination band.....	104
Figure 36. (a) The experimentally recorded P(13) line of acetylene at a concentration of 1000 ppm overlaid with a calculated and iteratively fit Voigt lineshape.....	105
Figure 37. P(13) line taken at concentrations ranging from 1000 ppm to 25 ppm.....	107
Figure 40. The first HC PBG – SMF28 interface.....	112
Figure 41. The EDFA spontaneous emission curve when the HC PBG sensor is inserted in the outer loop.....	116
Figure 42. A HC PBG end that has been cleaved using a guillotine fiber cleaver.....	117
Figure 43. The nearly cleaved HC PBG and the cleaved HC PBG on carbon tape.....	119
Figure 44. The chemical structure of aminotoluene (benzylamine).....	121
Figure 45. Preliminary results for the detection of a 1% solution of aminotoluene.....	122

List of Tables

Table 1. Fundamental vibrational modes of acetylene.....	59
Table 2. Fundamental vibrational modes of ammonia.....	72
Table 3. Experimental values of partial pressures (pp) of ammonia and water	77

List of Abbreviations

ARROW – Anti-resonant Reflecting Optical Waveguide
ASE - Amplified Spontaneous Emission
BPF – Band Pass Filter
CE – Capillary Electrophoresis
CRDS – Cavity Ring-down Spectroscopy
CW – Continuous Wave
DAQ – Data Acquisition
DDCI – 1,1'-diethyl-4,4'-dicarbocyanine Iodide
DFB laser – Distributed Feedback Laser
DIAL – Differential absorption LIDAR
DMSO – Dimethyl Sulfoxide
ECDL – External Cavity Diode Laser
EDFA – Erbium Doped Fiber Amplifier
FBG – Fiber Bragg Grating
FCRDS – Fiber Cavity Ring-down Spectroscopy
FIB – Focused Ion Beam
FLRD – Fiber Loop Ring-down
FT-IR – Fourier Transform Infrared
FSR – Free Spectral Range
FWHM – Full Width Half Maximum
GRIN Lenses – Graded Index Rod Lenses
HC PBG – Hollow-Core Photonic Band-Gap
HITRAN – High Resolution Transmission
HPLC – High Performance Liquid Chromatography
HSA – Human Serum Albumin
INO – Institute National d'Optique
LIDAR – Light Detection and Ranging

LPG – Long Period Grating
NBO – Non-bridging Oxygen
NIR – Near Infrared
NIST – National Institute of Standards and Technology
OSA – Optical Spectrum Analyzer
PDMS – Polydimethylsiloxane
PMMA – Polymethyl methacrylate
PMT – Photomultiplier Tube
PS -CRDS – Phase Shift Cavity Ring-down Spectroscopy
RI – Refractive Index
SMF – Single-mode Fiber
SOA – Semiconductor Optical Amplifier
TDL – Tunable Diode Laser
UV – Ultraviolet
VI – Virtual Instruments
VOA – Variable Optical Attenuator

Chapter 1

Introduction and Literature Review

Cavity ring-down spectroscopy (CRDS) is an absorption spectroscopic technique. In CRDS the concentration of an analyte is determined by measuring the reduction in finesse of an optical cavity made from two highly reflective ($R > 99.9\%$) mirrors once a sample is introduced. Optical loss is traditionally determined from the rate of the exponential intensity decay of a short laser pulse that is injected into the cavity. CRDS is thus insensitive to intensity fluctuations in the light source and the detector since one is recording the time it takes for the light intensity to decay to $1/e$ of its initial value - not the attenuation in intensity after passing through the sample.

This decay is the longest for an empty, high finesse cavity and is reduced when the sample absorbs or scatters light. Cavities with mirrors that have a reflectivity greater than 99.9% are useful for their ability to achieve sensitivities as low as $\alpha_{\min} = 10^{-11} \text{ cm}^{-1}$ for the detection of gases, liquids and aerosol particles; however, their large volumes (microliters) make them incompatible for the detection of samples in nanoliter to picoliter volumes. For this purpose, fiber loop ring-down spectroscopy (FLRDS) is advantageous since it allows for detection volumes that are on the order of, or less than, the fiber dimensions (picoliters). In practice this technique is best used in conjunction with separation systems which have microliter sample volumes and detection volumes that do not exceed a few tens of nanoliters, such as capillary electrophoresis and microfluidic devices. Conversely, FLRDS suffers from significantly higher (worse) detection limits (i.e. $\sim \alpha_{\min} = 0.1 \text{ cm}^{-1}$) compared to mirror-based CRDS (i.e. $\sim \alpha_{\min} = 10^{-11} \text{ cm}^{-1}$) since fibers have intrinsically higher losses than highly reflective mirrors and light coupling elements such as splices, connectors and couplers further reduce the light guiding

efficiency in the loop. In this thesis it is demonstrated that one can compensate for these losses by converting the system from a passive to an active loop through the insertion of an optical amplifier. In theory such a system should be able to obtain detection limits comparable to that of mirror-based CRDS, if the added gain can compensate for all undesired losses.

This chapter will take a look at the evolution of absorption spectroscopy to amplified fiber loop ring-down spectroscopy by discussing the theoretical properties of the techniques and by reviewing their respective relevant literature sources. Chapters 2 and 3 will discuss the experimental setup used and how it was characterised with different sensor interfaces. Chapter 3 will present a brief overview of the population kinetics in an erbium doped fiber amplifier (EDFA) as well as the light guiding characteristics in both traditional solid core optical fibers and hollow-core photonic band-gap fibers (HC PBGs). Chapter 4 presents the experimental results taken in the gas and liquid phases with a discussion of the improvements that can be made to the system and the experiments that can be conducted in the future. Finally, Chapter 5 will review the preceding chapters and summarize the future endeavours of the project.

1.1 Beer-Lambert Law

The Beer-Lambert law expresses the relationship between the transmission of light through a substance to its absorption coefficient, α or α' and to its path length, ℓ . The absorption coefficient of a sample is important because it allows one to determine the concentration, C , and molar absorptivity, ε , of the species as well as its number density, N , and absorption cross section, σ for liquids and gases respectively. These relationships can be seen in equations 1.1.1, 1.1.2 and 1.1.3, where one can interconvert between α and α' with a multiplicative constant that accounts for the difference between base 10 and base e .¹

$$T = \frac{I}{I_0} = 10^{-\alpha\ell} = 10^{-\varepsilon\ell C} \quad 1.1.1$$

$$T = \frac{I}{I_0} = e^{-\alpha'\ell} = e^{-\sigma\ell N} \quad 1.1.2$$

$$\alpha = \varepsilon C = \frac{N}{1000 \ln 10} \sigma \quad 1.1.3$$

1.2 Absorption spectroscopy

One of the most straightforward and non-invasive ways of determining the absolute concentration and/or absolute cross-section of a gas, liquid or solid is by laser absorption spectroscopy. Absorption spectroscopy uses the Beer-Lambert law to measure the attenuation of light traveling through a sample by comparing the initial intensity of the incident light (I_o) to the transmitted intensity (I), where ℓ is the optical path length of the sample and α is the absorption coefficient of the sample. Thereafter, one can use the absorption coefficient to determine the extinction cross-section of the sample. ¹

$$\alpha(\nu) = \sum N_i \sigma_i(\nu) \quad 1.2.1$$

where $\sigma(\nu)$ is the extinction cross-section, N is the number of molecules per unit volume and ν is the frequency of the light. In its simplest form absorption spectroscopy involves a single pass through the sample (Figure 1). To correct for light source intensity fluctuations the incident laser light can be split into a sample and reference beam - for example using a beam splitter. One detector records the intensity of the reference beam as the background, while the other fraction passes through the sample before it is detected - this portion of the light is subtracted from the background signal. This technique is useful for detecting compounds *in situ*; however, it suffers from low sensitivity since the absorption only attenuates a small portion of the incident light in comparison to the large background signal.

Fourier transform infrared (FT-IR) spectroscopy is a way of correcting for background fluctuations, while having excellent frequency resolution. ^{1,2} This technique uses a Michelson

interferometer, which splits the incoming beam at a beamsplitter. The beams are reflected at a stationary and a moveable mirror respectively and recombined at the beamsplitter where they interfere with one another depending on the change in position of the moving mirror. The interferogram is “decoded” via a Fourier transformation – a mathematical operation that decomposes a signal into its constituent frequencies (Equation 1.2.2).² The spectral resolution depends on the travel of the moveable mirror (i.e. typically a few millimeters) and is in the range of fractions of a wavenumber. The FT spectroscopy technique is useful since it measures all frequencies simultaneously. It works best for long wavelengths since the accuracy of the measurement is related to the relative precision with which the mirror can be moved.

$$\begin{aligned}
 f(t) &= \int_{-\infty}^{\infty} F(\nu) \exp(2\pi i \nu t) d\nu \\
 F(\nu) &= 2 \operatorname{Re} \int_0^{\infty} f(t) \exp(2\pi i \nu t) dt
 \end{aligned}
 \tag{1.2.2}$$

To increase the sensitivity of the system one must extend the path length by either extending the absorption cell or by folding the beampath multiple times through the sample. Physically increasing the length of the sample cell is a technique known as long path absorption spectroscopy. While this technique delivers increased sensitivity, kilometer long path lengths are impractical for a laboratory setting. Conversely, one may employ a multipass absorption technique, where the incident beam transmits through the sample multiple times to “effectively” increase the path length. This allows for high detection sensitivity in a smaller sample volume. Multipass absorption cells come in a variety of forms. The most basic and least effective multipass cell is the Fabry-Perot absorption cell, i.e. an optical cavity comprised of two flat mirrors (Figure 2 (a)). The incident light enters at one end of the cell and travels along the length

of it by reflecting back and forth between the two mirrors such that it eventually exits from the opposite end. The total number of passes depends on the incident angle with respect to the refractive index of the absorbing medium; it is hard to achieve more than 50 passes. The more popular and effective White cells and Herriott cells are comprised of spherical mirrors (Figures 2(b) and (c)). White cells differ from Herriott cells by spacing its mirrors at twice their focal length while the latter separates them by less than their focal length. White cells are easy to align but they only enhance the absorption path by a factor of 150; Herriott cells offer an enhancement factor of 300. Herriott cells operate by injecting light through an off-axis hole in one of the mirrors, where light traverses through the cavity in a Lissajous pattern and exits through the same hole. ¹

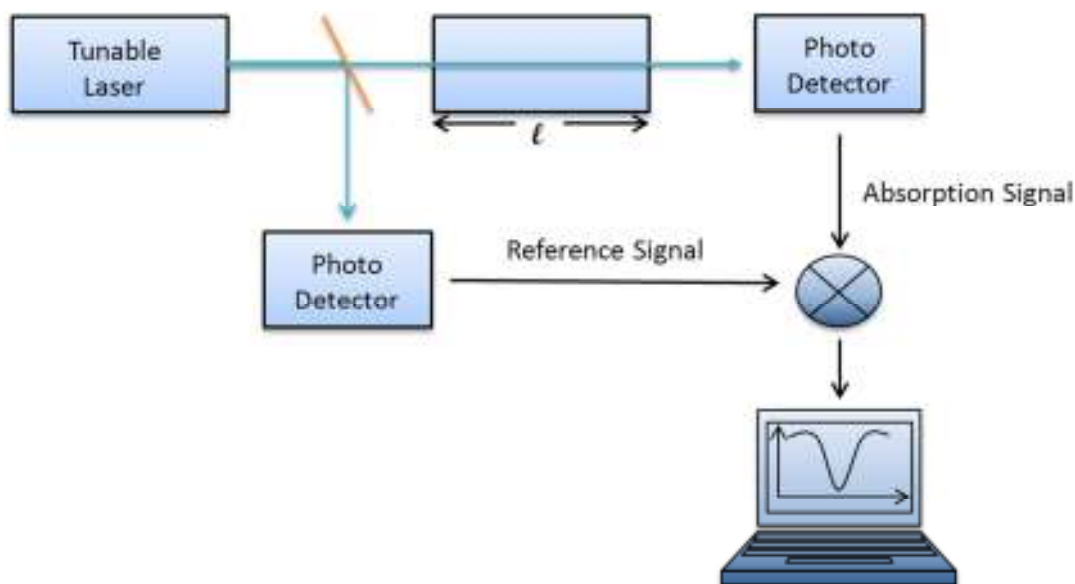


Figure 1. Schematic of a typical single pass absorption spectroscopy setup. Monochromatic light is emitted from a tunable laser and split into two separate beams via a beam splitter. Half of the light is sent to a photo detector to be used as the reference signal and then rest of the light is sent

through the absorption cell and detected as the absorption signal. Detection electronics extract a sample peak by subtracting the absorption signal from the reference signal.

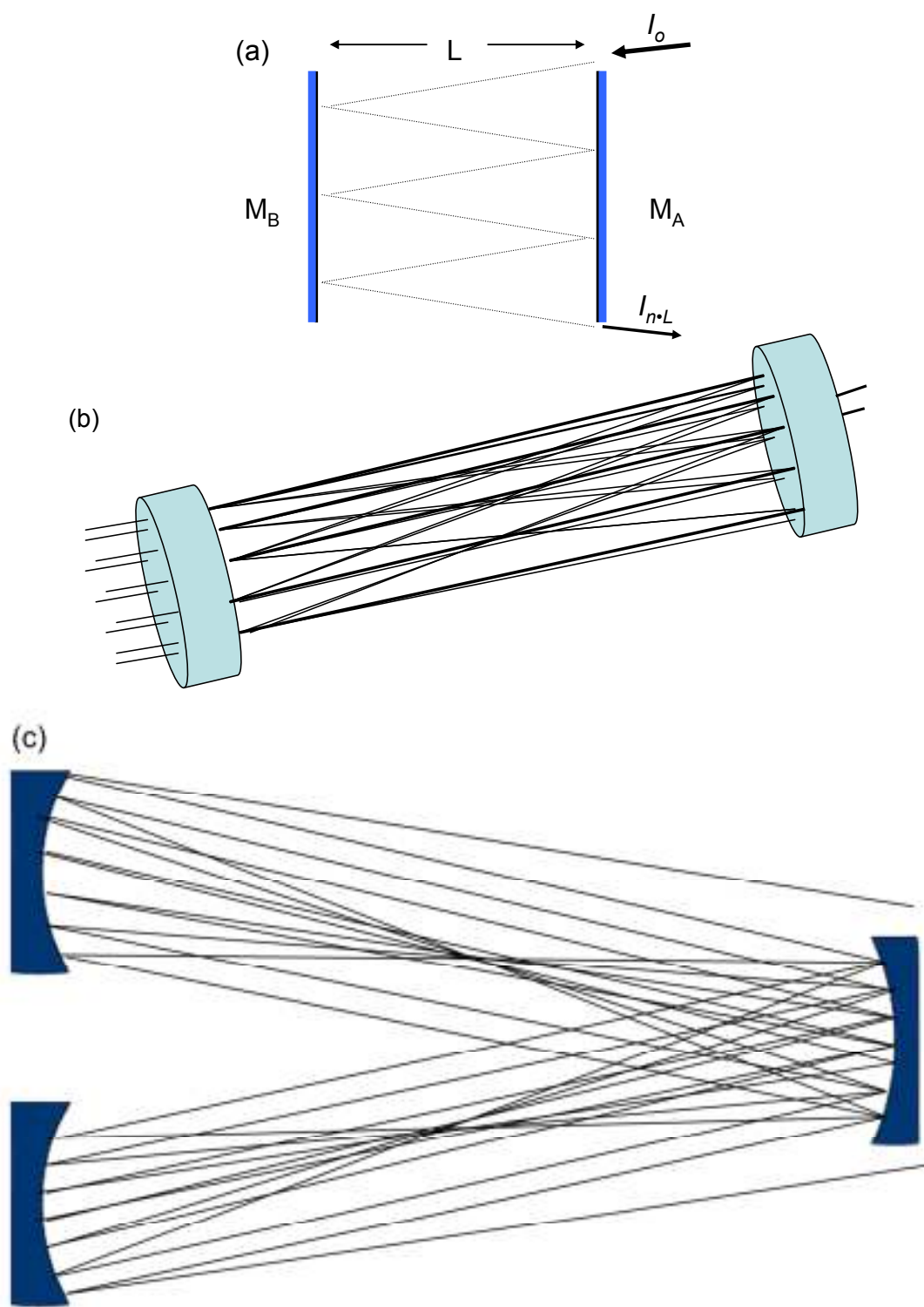


Figure 2. Multipass absorption cells. **(a)** Fabry-Pérot **(b)** Herriott cell **(c)** White cell.

1.3 Cavity Ring-Down Spectroscopy

The main limitation of direct absorption spectroscopy is its comparably low sensitivity, since one is measuring a small attenuation in transmitted light on top of a large background. The Beer-Lambert law states that the sensitivity of the concentration measurement dI/dC increases with the absorption path length. In some cases one may physically enhance the absorption path to several kilometers, as is done in Light Detection and Ranging (LIDAR) or in Differential absorption LIDAR (DIAL), or effectively do so by allowing the incident light to pass through the sample many times. As described above multipass cells effectively increase the absorption path length of a sample by passing the incident beam through the sample up to ~ 150 times without it overlapping on itself. They are relatively simple to align and have a significantly higher sensitivity than direct absorption spectroscopy; however, cavity ring-down spectroscopy (CRDS) delivers the greatest sensitivity with a simple setup. In addition, no calibration of the (possibly frequency dependent) intensity of the lightsource or detector response is necessary.³

CRDS is a sensitive absorption technique that typically measures the rate of decay of a light pulse confined in an optical cavity. This is done by coupling a short laser pulse into the optical cavity, which consists of two highly reflective mirrors ($R > 99.9\%$), and measuring the small fraction of light that leaks out from the second mirror in the setup (Figure 3). The mirrors are on mounts whose positions may be finely adjusted; when they are properly aligned, the laser pulse may decay exponentially in the cavity with a decay constant that can be as long as microseconds. Trapping the pulse in the cavity for this length of time allows the pulse to make thousands of round trips between the mirrors, thus resulting in a path length that is several kilometers long while maintaining a relatively small sample volume. Each round trip the light

takes reduces its intensity by a fraction that depends on the cavity losses, and the detector therefore measures an exponential decay of light intensity. Figure 4 shows the train of discrete pulses whose peak intensities make up the exponential decay that is seen by the detection electronics.⁴ One obtains the rate of absorption by comparing the time it takes for the pulse to “ring-down” (i.e. decay to 1/e of its initial intensity) in an empty cavity to its ring-down time (RDT) with a sample present. In an empty cavity the ring-down time is solely determined by the reflectivity, $R(\nu)$, of the mirrors and the optical path length, d , between the mirrors.³ The intensity of the light exiting the cavity follows the Beer-Lambert law and the resulting exponential decay can be fitted to Equation 1.3.1, where $I(\nu)$ is the initial intensity of the incident light and $\tau(\nu)$ is the lifetime of the light, otherwise known as the ring-down time. $\tau(\nu)$ can be expressed as the absorption path length divided by the product of speed of light, c , and the cavity losses. Equation 1.3.2 expresses the relationship between $\tau(\nu)$ and its contributing losses in greater detail, where α_i is the absorption coefficient of the sample, t_r is the roundtrip time, T is the transmission per roundtrip and $|\ln(R_{eff})|$ is the effective loss factor of the cavity itself. In cavities consisting of two or more mirrors R_{eff} is largely given by the product of the mirror reflectivities $R_{eff} = R_1 R_2$ ^{3,5}

$$I_{CRD}(t) \propto \int_0^\infty I(\nu) e^{\frac{-t}{\tau(\nu)}} d\nu \quad 1.3.1$$

$$\tau(\nu) = \frac{d}{c[|\ln(R_{eff})| + \alpha(\nu)l]} = \frac{-t_r}{\ln(T)} \quad 1.3.2$$

It is imperative that the frequency of the laser light entering the cavity resonates with the cavity modes for efficient light insertion to occur. An optical cavity has both longitudinal and transverse modes. ⁶ Equation 1.3.3 shows the spacing of the longitudinal modes, otherwise known as the free spectral range (FSR). Equation 1.3.4 gives the transverse mode spacing where m and n are respectively the x and y plane transverse modes. ⁷

$$\Delta \nu = \frac{c}{2d} \quad 1.3.3$$

$$\nu_{m,n} = \left(\frac{c}{\pi d} \right) \arctan \left\{ \frac{d}{[d(2r-d)]^{1/2}} \right\} \quad 1.3.4$$

Longitudinal modes have a larger full width at half-maximum (FWHM) when measured in the frequency domain. It is also easier to couple light into longitudinal modes since they accept a larger laser bandwidth compared to transverse modes. It is desirable to couple as much light as possible into these modes to achieve longer ring-down times and to increase sensitivity; on the other hand, when the optical cavity losses decrease so does the FWHM of the longitudinal modes. This relationship is known as the finesse of the cavity and is shown in equation 1.3.5 where ρ is the fraction of the circulating power lost after one round trip. ¹

$$F = \frac{\pi}{2 \arcsin \left(\frac{1 - \sqrt{\rho}}{2\sqrt{\rho}} \right)} \approx \frac{\pi}{1 - \sqrt{\rho}} \approx \frac{\pi}{1 - \rho} \quad 1.3.5$$

The approximation in Equation 1.3.5 holds for low loss, i.e. high finesse, cavities. The quality factor of the cavity, Q , relates to the ring-down time by $2\pi\nu$ and to the finesse of the cavity by the resonance frequency divided by the FSR. ¹

$$Q = 2\pi\nu\tau \quad 1.3.6$$

$$Q = \frac{\nu}{FSR} F \quad 1.3.7$$

When using pulsed light the mode structure of a cavity can cause a number of problems. The excitation of both longitudinal and transverse modes results in mode beating and oscillations in decay curve, which makes it hard to accurately determine the ring-down time. As well, if the modes are too widely spaced then molecular absorption features may fall between them and be missing from the spectrum.³ To minimize these effects a stable optical cavity ($0 < d < r$) is used with a near-continuum mode structure (i.e. the ratio of the transverse to longitudinal mode spacing is irrational).⁸ This type of cavity used in conjunction with a pulsed laser whose bandwidth is larger than the mode spacing, such that in theory all frequencies are coupled into the cavity with an equal probability. As a result of so many modes being excited, the modulation depths of the beats seen in the ring-down transients are dramatically reduced.⁷ While the setup of pulsed CRDS is simple, it is limited by the spatial resolution of the transverse modes and the ultimate sensitivity that can be obtained from the mode beating effects on the ring-down transient.

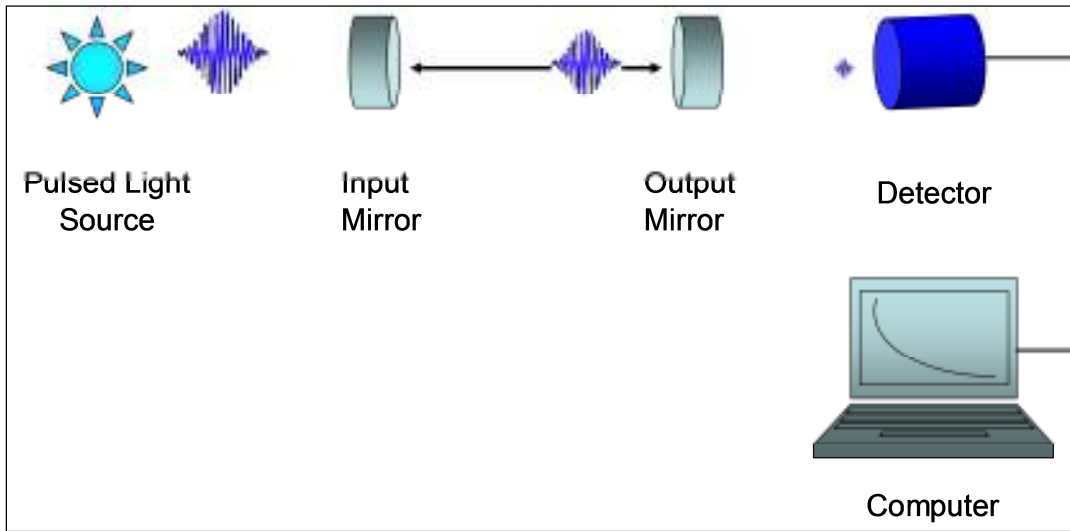


Figure 3. Traditional optical cavity for pulsed CRDS

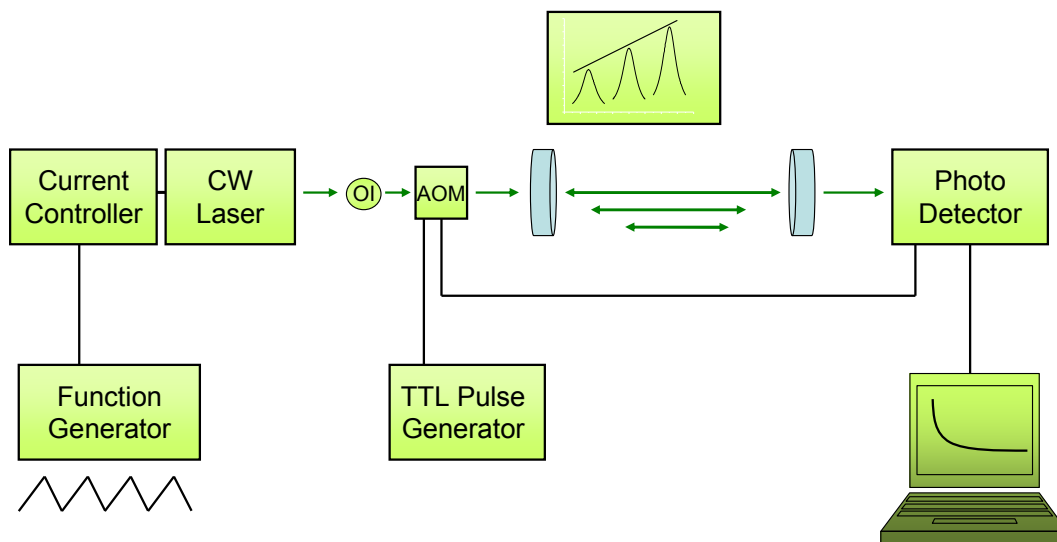


Figure 4. A common setup for CW CRDS. The current of the laser is modulated such that the laser's frequency is ramped through the cavity's FSR and comes into resonance with multiple longitudinal modes. Once the modes reach a specified intensity, light is deflected away from the cavity by the acousto optical modulator (AOM) and the ring-down time is recorded. Since the cavity is linear an optical isolator (OI) is placed in front of the laser to protect it from a large quantity of optical feedback.

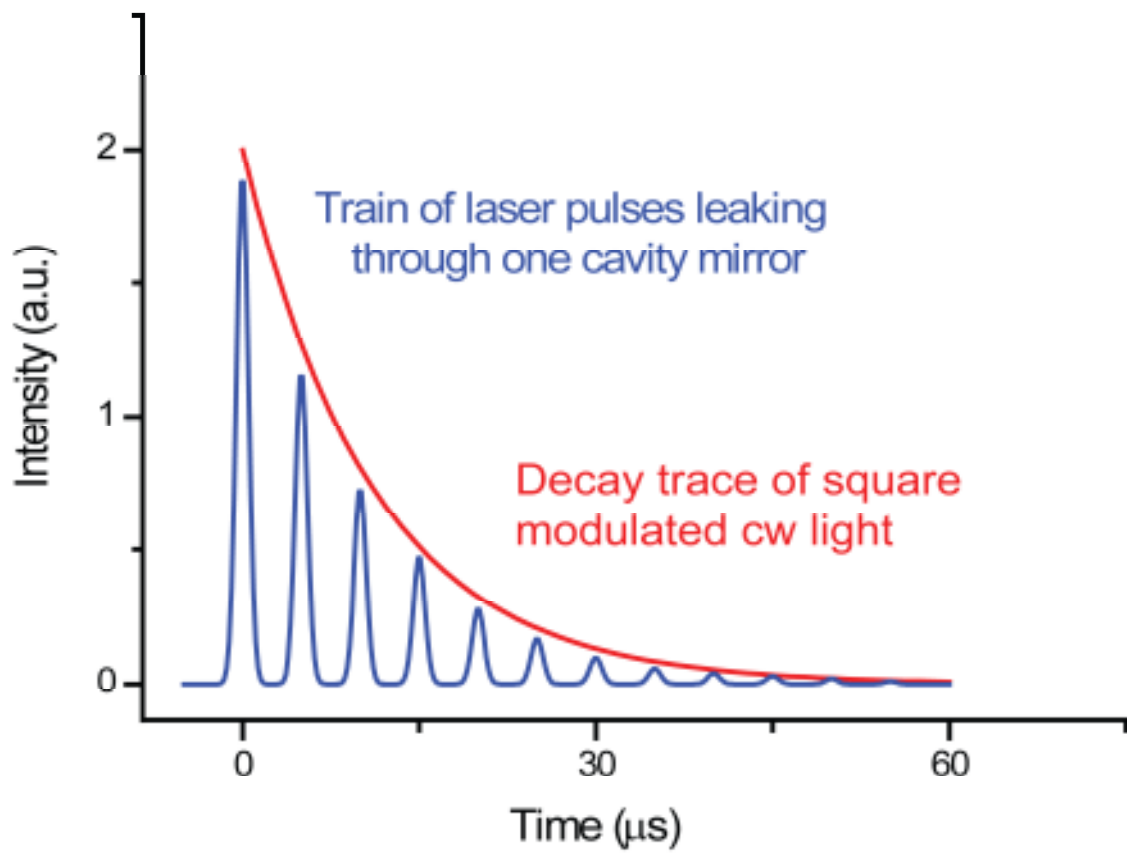


Figure 5. Exponential decay of pulsed and square modulated cw laser light within a ring-down cavity.

CRDS took root in 1980 when Herbelin et al. measured the lifetime of the light in an optical cavity to determine the reflectance of the cavity mirrors.⁹ By intensity modulating a continuous wave (cw) light beam they were able to measure the phase shift induced by the reflection losses of the mirrors. This technique is now known as Phase Shift (PS) - CRDS and is often used to measure gases, liquids and particles in mirror based optical cavities as well as in the comparatively more lossy fiber-loop cavities.¹⁰⁻¹³ In 1984, Anderson et al. expanded the concept of exciting an optical cavity with a cw light source by switching off the light source when its intensity reached a preset threshold value and subsequently measured the intensity decay time.¹⁴ Although the purpose of this experiment was to measure mirror reflectivity, it was later realized that cw-CRDS is one of the most sensitive forms of CRDS when exciting single longitudinal modes of the ring-down cavity.³ Originally, neither of these two early CRDS experiments used any mode matching techniques; cavity excitations occurred via coincidences of the laser frequency coming into resonance with one of the narrow cavity modes.³

Later, O'Keefe and Deacon performed the first pulsed CRDS experiment in 1988 and recorded an absorption spectrum of the weak $b^1\Sigma_g^+(\nu=1,2) \leftarrow X^3\Sigma_g^-(\nu=0)$ bands of molecular oxygen.¹⁵ This experiment showed that one can avoid mode-matching complications, as well as the need for fast electronics to switch off and monitor intracavity intensity, when using a pulsed laser. The results showing the weak forbidden $O_2 b^1\Sigma_g - X^3\Sigma_g$ transition can be seen in Figure 6.

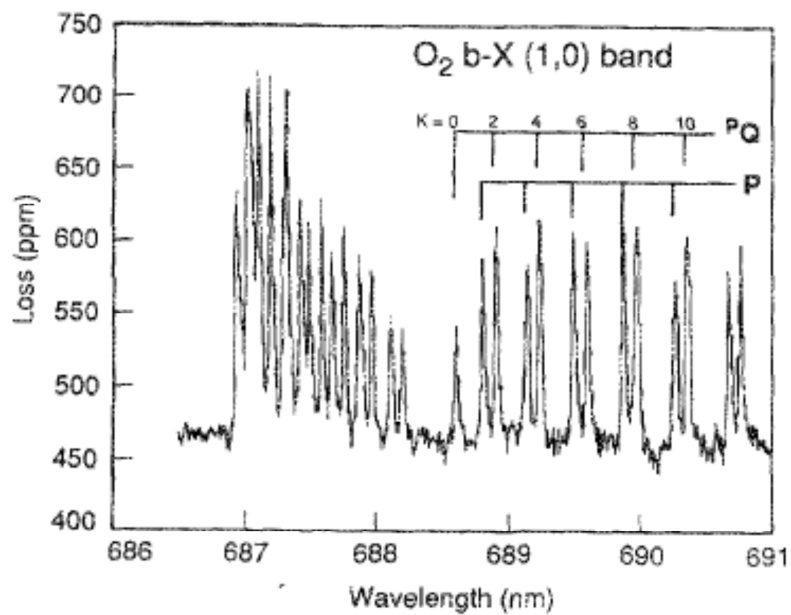


Figure 6. CRDS spectrum of the O₂ $b(v=1)$ - $X(v=0)$ band taken with a one wavenumber bandwidth laser in a 60 cm long cavity. The spectrum was taken in room air. Reproduced from O'Keefe et al.¹⁵

1.4 Continuous Wave - CRDS

In order for pulsed CRDS to be successful, the bandwidth of the pulse must be wide enough to overlap one or more longitudinal cavity modes, thus it must be wider than the cavity's free spectral range (FSR).³ In general, pulsed CRDS uses lasers with bandwidths of approximately 3 GHz and cavities that are a few tens of centimeters long (FSR \sim 5 GHz).¹⁶ While this technique has proven itself to be successful for studying the spectroscopy of weak gas transitions¹⁷⁻²⁰, as well as for detecting radical species in flames,⁸ in diamond deposition reactors,²¹ and for ions in a discharge,²² its resolution is limited by the cavity's FSR. One of the most obvious ways to increase the resolution is to make use of the high spectral density of the transverse cavity modes. However, this compromises the relative ease of pulsed CRDS experiments with complications such as transverse mode beating, multiexponential decays, and, consequently, fluctuations in the decay rate.^{23,24} To avoid such problems one can increase the resolution by expanding upon the cw-CRDS technique that was first used by Anderson *et al.*, in 1984.¹⁴ In Anderson's experiment narrow bandwidth cw light from a He-Ne laser was injected into the optical cavity such that it came into a coincidental resonance with one of the cavity modes. When the intensity of the light inside the cavity exceeded a predefined threshold, a triggering system switched a Pockels cell that interrupted the laser and recorded the ring-down transient.³ This opened up the possibility to obtain high signal to noise ratios by efficiently injecting single frequency cw light tuned to one of the cavity resonances. In 1997 Romanini *et al.*,¹⁶ built a setup similar to that of Anderson *et al.*,¹⁴ but used an acousto-optic modulator to interrupt the laser beam rather than a Pockels cell. They measured the overtone transition of acetylene near 570 nm at 5 Torr using a single frequency ring dye laser. The cavity used was

approximately 50 cm long, with one end mounted on a piezoelectric transducer (PZT), to bring the cavity modes into resonance with the laser frequency by periodically modulating the cavity length. A feedback circuit was implemented to monitor drift in the cavity by measuring the distance of the ring-down events from the centre of the modulation range and providing a correction voltage to the PZT. They achieved a sensitivity of 10^{-9} cm^{-1} . They later reported a sensitivity of $2 \times 10^{-10} \text{ cm}^{-1}$ when they recorded part of the rotationally and vibrationally cooled spectrum of NO_2 using an external cavity diode laser (ECDL) at 775 nm.²⁵ An alternative to adjusting the cavity length is to modulate the frequency of the laser.^{25,26} One can only use this technique if the width of the absorption feature is much larger than the FSR of the cavity; it is especially helpful when one is using ECDLs to detect absorptions at atmospheric pressure.²⁶

Some advantages of cw-CRDS are its increase in spectral resolution compared to pulsed CRDS, its ability to detect trace gases, and its potential to make use of cost effective diode lasers and photodiodes. Conversely, its disadvantages are the need for mode matching optics, costly optical isolators, and its limited spectral range. Finally, aligning the cavity is not as simple as it is for pulsed CRDS.³

1.5 Phase Shift - CRDS

Like pulsed CRDS and cw-CRDS, PS-CRDS measures the lifetime of the light in an optical cavity; however, one achieves this in the frequency domain rather than the time domain. PS - CRDS is a truly continuous wave technique since one does not interrupt the laser beam to record a decay trace. The intensity of the laser light is sinusoidally modulated and the shift in phase of the light exiting the cavity relative to the incoming light is measured.^{10,11} In 1933 Duschinsky showed that when an intensity-modulated beam at frequency ω is used to excite an atomic or molecular energy level the resulting fluorescence is still modulated at the frequency ω , but with a phase shift and decreased modulation depth relative to the I_o beam.²⁷ The phase shift, ϕ , of the light relates to the lifetime (i.e. decay time) of the excited state, by Equation 1.5.1 and the modulation depth is decreased as shown in Equation 1.5.2.²⁷

$$\tan \phi = -\omega\tau \quad 1.5.1$$

$$\frac{1}{\sqrt{1 + \omega^2\tau^2}} \quad 1.5.2$$

Thereafter, Herbelin et al. showed that this technique is applicable towards measuring the lifetime of light in optical cavities when he used it to determine the reflectance of his mirror coatings.⁹ Following this, Engeln et al. used the phase shift technique to measure the $b^1\Sigma_g^+(v'=2) \leftarrow X^3\Sigma_g^-(v''=0)$ transition of $^{18}\text{O}_2$.¹⁰ In their experiment they modulated a single mode (sm) ring dye laser using an electro-optic modulator (EOM) and injected the modulated light into a 45 cm long stable optical cavity. They showed that for an intensity modulated cw source, the intensity of the light leaving the cavity at time, t , ($I_{CRDS}(t)$) is given by Equation 1.5.3.

$$\begin{aligned}
I_{CRD}(t) &= \frac{1}{\tau(\nu)} \int_{-\infty}^t I_o (1 + \alpha \sin \omega t') \exp\left[-\frac{t-t'}{\tau(\nu)}\right] dt \\
&= I_o \left(1 + \frac{\alpha}{1 + \omega^2 \tau(\nu)^2} [\sin \omega t - \omega \tau(\nu) \cos(\omega t)] \right) \\
&= I_o \left(1 + \frac{\alpha}{\sqrt{1 + \omega^2 \tau(\nu)^2}} \times \sin[\omega t - \arctan \omega \tau(\nu)] \right)
\end{aligned} \tag{1.5.3}$$

Thus, $\tau(\nu)$ can be determined independently from the intensity by taking a ratio of the in-phase component to the out-of-phase component of the modulated light intensity exiting the cavity as a function of laser wavelength. The highest detection sensitivity occurs when $\tau\omega = 1$ and therefore $\phi = 45$ degrees ($\tan \phi = 1$). A lock-in amplifier was used to determine ϕ , since it is able to measure the in-phase signal, the out-of-phase signal and the shifted phase angle.¹⁰

In 2004 the Loock group adapted this technique to record the considerably shorter decay times in fiber-loop ring-down spectroscopy.¹¹ They note that while the phase-shift technique provides a vastly increased time response in comparison to time resolved CRDS, its shortcomings, such as its inability to deal with multiexponential decays, mode-beating, and its sensitivity to optical and electrical noise, make it the less favoured technique when performing gas phase measurements. Conversely, the increased time response makes the PS technique highly attractive to FLRDS and other waveguide cavities where the ring-down times may only be a few nanoseconds long.²⁸ Additionally the duty cycle of PS-CRDS is unity making this technique the CRDS method with the highest data acquisition rate. High data acquisition rates and fast response times are particularly important in analytical separations. The Loock group derived a

modified relationship between ϕ and $\tau(\nu)$ to include an offset angle, ϕ_o , to account for intrinsic phase delays due to lags in the electronic signal transmission in electronic components, the cables and the laser diode, as well as light transmission in the power delivery fibre. This relationship is shown in Equation 1.5.4.¹¹

$$\phi = \phi_o - \arctan(\omega\tau) \quad 1.5.4$$

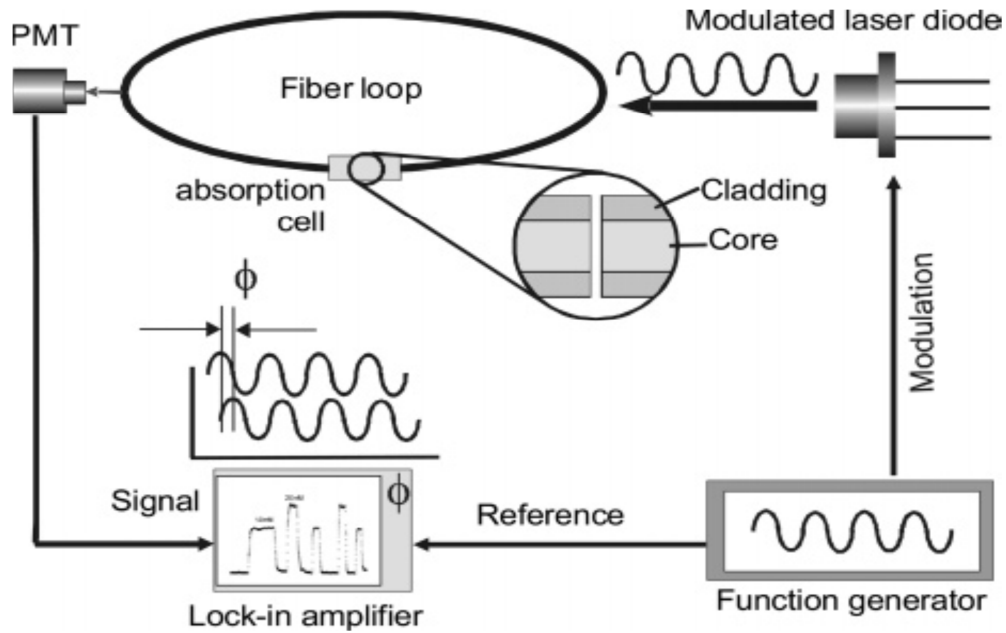


Figure 7. Experimental scheme of a phase-shift fiber loop ring-down experiment. The LeCroy 9100 arbitrary function generator produces two channels of sine waves with the same frequency and phase. One of them is used for the reference of the lock-in amplifier, the other one modulates the output of a laser diode. The modulated laser diode output is coupled through free space into a

power delivery fiber, which is coupled to the fiber loop using index-matching fluid. A photomultiplier tube detects the phase-shifted photon signal and transfers it to the lock-in amplifier. Adapted from Tong et al.¹¹

In 2009 the Loock group modified Equation 1.5.2 to account for multiexponential decays.⁵ Multiexponential decays occur when there are multiple lifetimes of the light in the cavity, rather than one. In optical cavities consisting of mirrors these multiple decays may be due to scattered light, broadband emission (BBE) bypassing the cavity, and amplified spontaneous emission (ASE). Decays resulting from BBE passing through the cavity are comparatively short to ASE (i.e. trapped BBE in the cavity that is amplified alongside the rest of the laser light).^{5,29,30} This approach was inspired by the one Lakowicz et al. took in 1984 to address the issue of biexponential decays in fluorescence spectroscopy when the phase-shift method is used to measure the fluorescence lifetimes.³¹ Lakowicz showed that one could extract two fluorescence decay lifetimes by recording the phase at more than 8 modulation frequencies spread over 2 decades and fitting the resulting phase angles to an analytical expression.⁵ Lakowicz et al.³¹ and Bescherer et al.⁵ assumed that the time it takes for the total light intensity to decay in the time domain can be modeled as a sum of N exponentials as seen in Equation 1.5.5. Thereafter, Equation 1.5.6 shows that one can model the response of this system to an oscillatory input with an angular frequency of $\omega=2\pi f$ by taking a Laplace transform of Equation 1.5.5.^{5,29,31}

$$I(t) = \sum_i^N \alpha_i \exp\left(-\frac{t}{\tau_i}\right) \quad 1.5.5$$

$$\mathcal{L}(I(t)) = \sum_i^N \frac{\alpha_i \tau_i}{\tau_i s + 1} \quad s = i\omega + \sigma \quad 1.5.6$$

σ , is a damping factor that is assumed to be zero. Equation 1.5.6 is separated into its real and imaginary parts (Equations 1.5.7 and 1.5.8); the associated phase angle and absolute modulation depth are given by Equations 1.5.9 and 1.5.10 respectively.

$$\mathcal{L}(I(t)) = iN_\omega + D_\omega \quad 1.5.7$$

$$N_\omega = -\sum_i^N \frac{\omega\alpha_i\tau_i^2}{\omega^2\tau_i^2 + 1} \quad 1.5.8$$

$$D_\omega = \sum_i^N \frac{\alpha_i\tau_i}{\omega^2\tau_i^2 + 1}$$

$$\tan \phi = \frac{N_\omega}{D_\omega} = \frac{-\sum_i^N \frac{\omega\alpha_i\tau_i^2}{\omega^2\tau_i^2 + 1}}{\sum_i^N \frac{\alpha_i\tau_i}{\omega^2\tau_i^2 + 1}} \quad 1.5.9$$

$$m = \sqrt{N_\omega^2 + D_\omega^2} \quad 1.5.10$$

Finally, Bescherer et al.⁵ showed that Equation 1.5.7 is related to Equation 1.5.2 since the phase and modulation of each decay is independent from one another, thus it may be written that

$$\tan(\phi_i - \phi_o) = -\omega\tau_i \quad 1.5.11$$

To prove the validity of these equations with respect to multiexponential decays in PS-FLRD, Bescherer et al. compared the ring-down times measured with a multiexponential fit in the time domain to those calculated in the frequency domain using the equations derived above.⁵ In this experiment a 25.6 m multimode fiber was spliced into a closed loop. Light from an 800 nm laser was coupled into the loop using a 99:1 coupler and a photomultiplier tube (PMT) was

placed next to the fiber to detect scattered light from the loop. The results of this experiment (Figure 8.) show that a tri-exponential model fits the data best in both the time and frequency domain. It was noted that these results are consistent with those reported by Tong et al.³² who noted that the longest ring-down time is associated with the decay in the core modes and that the faster decay process is due to light leaving the cladding modes.⁵ As well, it was noted by Bescherer et al.⁵ that the third decay process is likely due to scattered light. Although the results show that the ring-down times in the time domain were not identical within the fitting error to those in the frequency domain, the accuracy of the fitting parameters were not equal since the time domain had significantly more data points (10,000) compared to the phase shift data (192 points).⁵ On the other hand, they also show that the phase shift measurements were the more reliable of the two for recording the fastest decay process. The rise and fall times of the laser were <20 ns and the ring-down times in both domains were shorter than the response time of the instrument. As a result, one cannot accurately measure this quick decay in the time domain; however, the phase shift method resolves the quick decay by using higher modulation frequencies.⁵

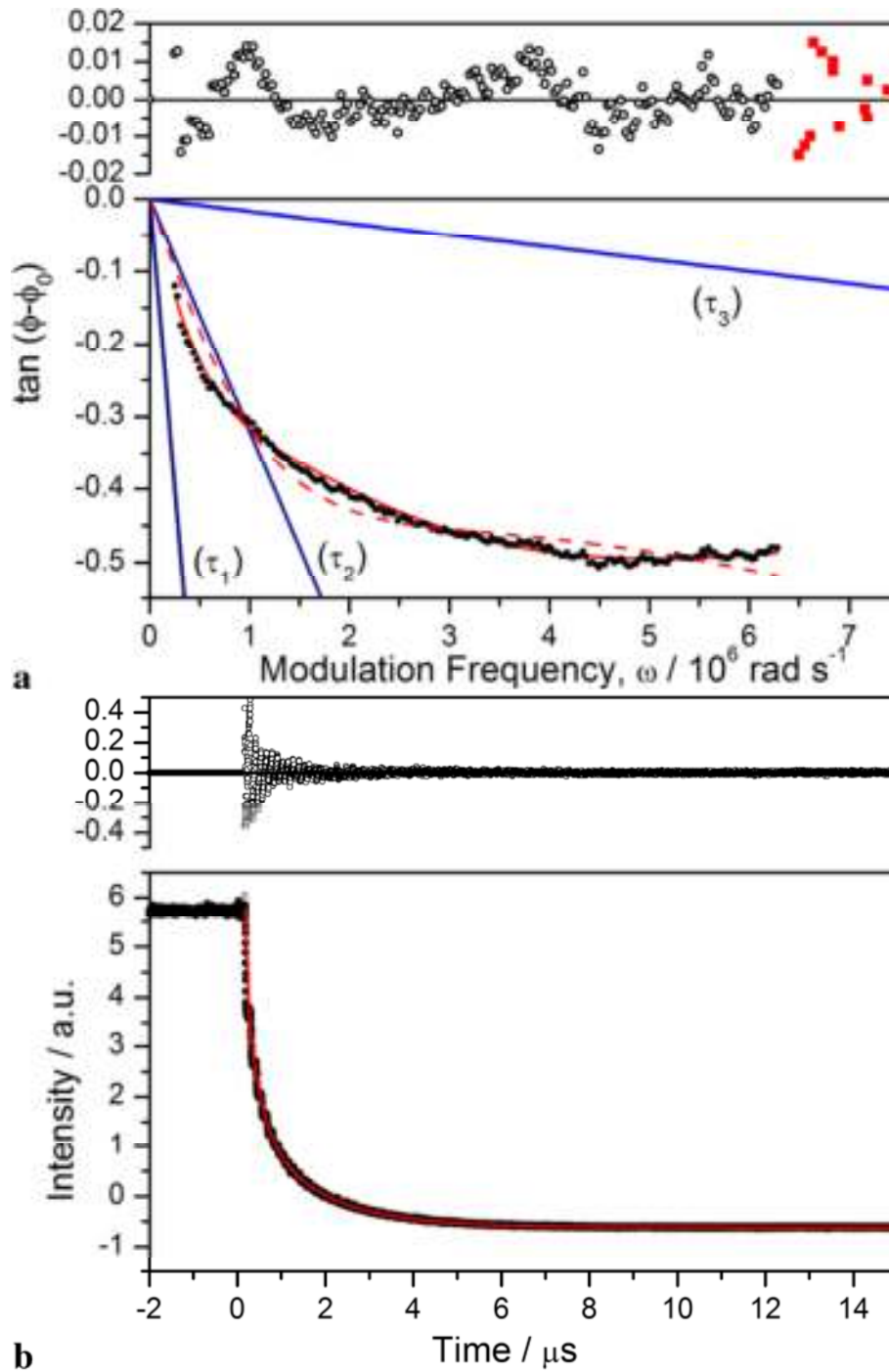


Figure 8. Multiexponential decay of light injected into a 25.6 m multimode fiber loop at $\lambda=800$ nm. (a) A fit of Equation 1.5.7 to the phase angle (*solid line*) yields $\tau_1=1.57(4) \mu\text{s}$, $\tau_2=320(9) \text{ ns}$,

and $\tau_3=17(2)$ ns. The *straight lines* correspond to curves expected for single exponential decays with respective τ . The *dashed line* corresponds to the best fit to a bi-exponential decay function. (b) In the time domain a fit to Equation 1.5.3 yields $\tau_1=1.503(6)$ μ s, $\tau_2=312(2)$ ns, and $\tau_3=7.0(2)$ ns. The residuals for the time domain triexponential fit and the frequency domain biexponential fit are shown above the respective panels. One can see that the triexponential fit is in good agreements with the time domain trace while the frequency domain trace is not well modeled by a biexponential decay. The distribution of measurement errors for the phase angle is described well by a Gaussian function (*red squares*). Reproduced from Bescherer et al. ⁵

1.6 Fiber Cavity Ring-Down Spectroscopy

Fiber cavity ring-down spectroscopy (FCRDS) is an adaptation of CRDS that uses an optical fiber as its waveguide rather than mirrors. FCRDS can be carried out using either a linear cavity and two identical fiber mirrors or a fiber loop cavity.³³ Linear fiber cavities confine light by applying dielectric coatings or fiber Bragg gratings (FBGs) to the fiber ends. One is able to build linear cavities that are only millimeters long; this is at times advantageous to fiber loop cavities, whose shortest length is limited to approximately 30 cm because of macrobending losses.³² Moreover, it is straightforward to couple light into and out of linear cavities since the light source and detector can be placed in line with the cavity. Finally, both cavities with reflective coatings and FBGs exhibit very low round trip losses.³² For example a linear cavity with dielectric coatings on the fiber ends built by von Lerber et al.³⁴ in 2002 achieved roundtrip losses of 0.42%. As well, Gupta et al.³⁵ achieved 2.3% roundtrip losses in a 10 m long hydrogen-loaded single-mode fiber with FBGs on the ends acting as mirrors. Andachi et al.³⁶ compared loop to linear cavities by constructing a linear cavity out of identical FBGs and a loop cavity that used 99:1 couplers to guide light into the loop and out to the detector. The linear cavity was found to have 0.03 dB (0.64 %) roundtrip losses and the loop cavity had round trip losses of 0.25 dB (5.6%) and 0.84 dB (17.6%) for the core and cladding modes respectively. FBGs have a strong wavelength dependent attenuation, which can correspond up to a reflectivity to 99.99%, and most of the light reflects back into the single counter propagating core mode (i.e. the core mode traveling in the respective opposite direction).^{33,36} In addition to the advantages listed, sometimes the FBGs are both the sensing and reflecting element in the fiber cavity, since they are sensitive to thermal expansion and pressure.³⁷ Currently, linear setups use FBGs more

often than reflective coatings since they are commercially available and easy to implement. Conversely, FBGs pose a number of disadvantages, such as their inability to reflect light over a range greater than a few nanometers, the fact that they are commercially available only at telecom wavelengths, and that they are usually designed for single-mode fibers.³³

In contrast to linear cavities, one constructs ring cavities by forming a loop of fiber and splicing the two ends together or by leaving a gap between the two ends where one can inject samples.¹¹ Light is usually coupled into the loop by high split ratio couplers (e.g., 99:1); however alternate methods are possible.³³ In 2002, Brown et al.³⁸ focused a laser beam onto the fiber which resulted in about $1:10^8$ of the light coupling into the loop. To measure the loop's light intensity one may splice a fiber coupler into the loop to guide light to a detector, or place a PMT next to the fiber to detect the scattered light.^{5,33}

Unlike linear cavities, loop cavities are broadband (i.e., 250-1,700 nm) since transmission of the loop is only dependent upon the transmission of the fiber optic material and the components in the cavity loop. At telecom wavelengths (1.3-1.5 μm) fibers exist with losses as low as 5×10^{-4} dB/m; UV-wavelength fibers have considerably higher losses of 0.05 dB/m at 400 nm and 0.3 dB/m at 250 nm; Mid-infrared-wavelength fibers exist up to wavelengths of 9 μm and losses of less than 0.5-0.2 dB/m are specified by the manufacturers.³³

Overall, fiber cavities present themselves as an inexpensive, simple, and rugged alternative to mirror cavities. They use low power lasers (e.g. μW) and inexpensive photodiodes; FLRD-based sensor loops have the ability to be multiplexed due to the uniform sensing scheme and waveguide; finally, the detection scheme for any analyte is uniform, thus FLRD may be

easily configured to detect anything from chemicals to temperatures and pressures by merely changing the sensor head in the fiber loop.³⁹

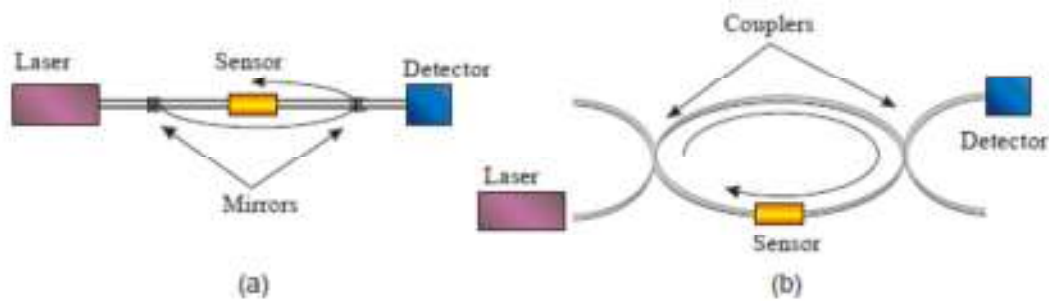


Figure 9. (a) A linear fiber cavity formed by adding two mirror elements, such as fiber Bragg gratings or dielectric coatings, to the ends of the fiber to form an optical cavity. The light is injected through one of the mirrors and is detected behind the second mirror. (b) A fiber ring cavity made by bending the fiber into a loop and implementing fiber couplers with high splitting ratios to inject light into the loop and to direct a small fraction of light to the detector. Adapted from Waechter et al.³³

Since the sensor placed in or on the fiber cavity is not limited to one type of chemical phase or physical process, thus a variety of sensors are available for insertion into the loop or to be constructed out of the fiber itself (Figure 10). The most straightforward “sensor head” is a gap in the fiber where any gas, liquid or particle sample can reduce the ring-down time by absorbing or scattering light. Conversely, one may detect samples by exposing the evanescent field of the core mode(s). This is done by either tapering a region of the fiber, etching away the cladding or by encasing the fiber in a glass block and side-polishing the fiber (Figure 10 (b), (c) and (d) respectively).³³ As well, sensor heads may consist of fiber optic components that react to the refractive index of the sample such as long-period gratings.⁴⁰ Lastly, mechanical and thermal

sensors are implemented into fiber cavities since some fiber optic components (e.g. FBGs) are sensitive to temperature,⁴¹ pressure,^{42,43} bending losses⁴⁴ and strain^{45,46} exerted on the fiber.³³

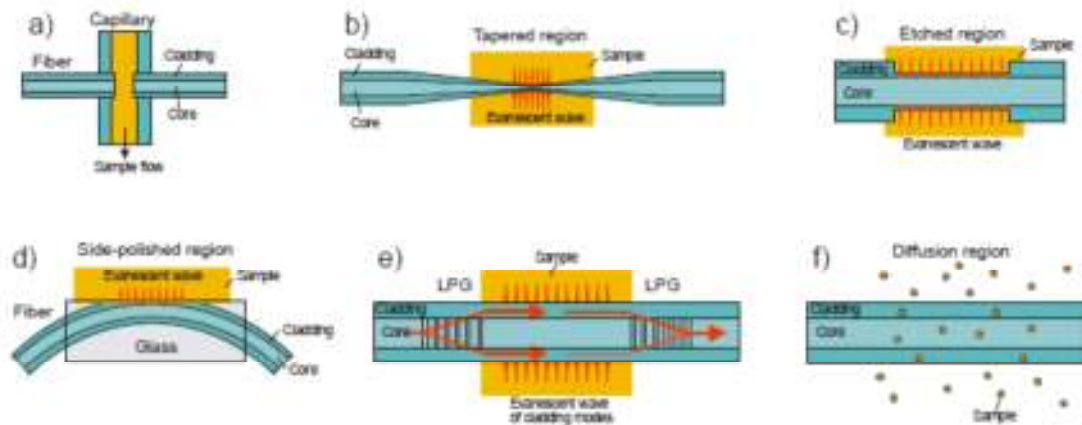


Figure 10. Different types of sensor elements used in fiber cavity ring-down spectroscopy. **(a)** A gap in the fiber is used to measure the direct attenuation from a gas, liquid or solid sample placed between the fibers. **(b)** A tapered fiber allows the evanescent field to extend outside the fiber by converting the core mode into a cladding mode. **(c)** The evanescent field is extended into the sample by etching the cladding. **(d)** The evanescent field is exposed in a field access block by side polishing the fiber to reduce the cladding thickness. **(e)** A pair of identical long-period gratings (LPGs) are used to couple light from the core mode into a single cladding mode and then back into the core. While the light travels in the cladding mode between the two LPGs its large evanescent wave interacts strongly with the surrounding sample. **(f)** The absorption by gases of small molecules such as H_2 can be monitored by allowing them to diffuse into the fiber. Adapted from Waechter et al.³³

1.6.1 Fiber Loop Ring-Down Spectroscopy

Stewart et al.⁴⁷ originally proposed the concept of FLRDS for chemical sensing in 2001. Their setup involved a 50 m fiber loop cavity that contained an erbium doped fiber amplifier (EDFA) and a 5 cm micro-optical gas cell for gas phase absorption measurements in the telecom region. In this fiber loop cavity the circulating light was amplified with every round trip akin to a fiber laser that is operated below the laser threshold.^{47,48} The purpose of this cavity was to demonstrate the cavity ring-down principle while compensating for the intrinsic loop losses due to couplers, splices, etc. Stewart's work will be discussed in greater detail later in this report. This setup was quite complex compared to the succeeding passive (i.e. non-amplified) FLRD setups built in 2002 by Brown et al.³⁸ and Lehmann et al.⁴⁹ As mentioned earlier, Brown et al.³⁸ constructed optical fiber loops ranging in length from 2-77 m that were joined via a splice connector. Light was coupled into the loop by focusing a Nd:YAG pumped dye laser with a width of 500 ps and an energy of 50-200 $\mu\text{J}/\text{pulse}$ onto the fiber loop such that $1:10^8$ of the intensity entered the loop. A PMT was placed at least 50 cm from the excitation region of the fiber to detect the scattered light after each round trip. Their "absorption cell" was approximately 3.8 μm long and was made by replacing the index matching fluid in the fiber splice with their sample solution. They were able to measure the absorption spectrum of a solution of 1,1'-diethyl-4,4'-dicarbocyanine iodide (DDCI) in dimethyl sulfoxide (DMSO) ($n=1.479$) between 740-880 nm and achieved a detection limit of an absorptivity of $\epsilon C = 100 \text{ cm}^{-1}$.³⁸ Thereafter, in 2003 the Loock group characterized the FLRD technique in detail³² and in 2004 demonstrated

this technique with a cw laser ¹¹ where they recorded the decay times at a data acquisition rate close to real time (10-100 ms) using the phase shift technique.

The loop constructed by Lehmann et al. ⁵⁰ had a small tapered region such that the evanescent wave of the core mode was exposed. Rather than placing their sample into the loop, they measured the absorption of the evanescent wave outside the fiber and achieved a minimum detectable concentration of 0.049% 1-octyne per Hz^{-1/2}. ⁵⁰

FLRD has shown itself to be an optimal detection method for real time micro-separation systems such as capillary electrophoresis (CE), micro-liquid chromatography or microfluidic devices (i.e. “lab on a chip” or μ -TAS: micro-total analysis systems). ⁵¹ The aspects that make microfluidic devices advantageous (i.e. their small sample volumes and high separation speeds) are also what challenge most detection systems. While fluorescence spectroscopy is an extremely sensitive option (i.e. allowing for single molecule detection in some cases ⁵²), it is limited by the fact that not all molecules fluoresce and the labeling process of non-fluorescent molecules may introduce errors in the measurements. In terms of chromatographic applications, UV-VIS absorption spectroscopy is commonly used since many analytes absorb in the near UV region. On the other hand, the width of the absorption paths correspond to the width of the separation channels (i.e. 50-100 μm for CE, ⁵³ 30 \times 50 μm for commercial microfluidic devices ⁵⁴) and the time response required is on the order of milliseconds, thereby making it impossible to average multiple separation events. This results in poor sensitivity, especially for analytes with small molar extinction coefficients. A way to increase the absorption path is to implement “Z-cells” ^{55,56}, “U-cells” ⁵⁷ or bubble cells ^{58,59} into the microchannel (Figure 11), however this sacrifices

the temporal resolution since it is not straightforward to interface these cells to a spectrometer. Finally, as mentioned earlier in this report, these absorption techniques suffer from the problem of measuring a small intensity change on top of a large background signal. If the light source is a laser, this problem is further complicated by light intensity fluctuations.⁵¹

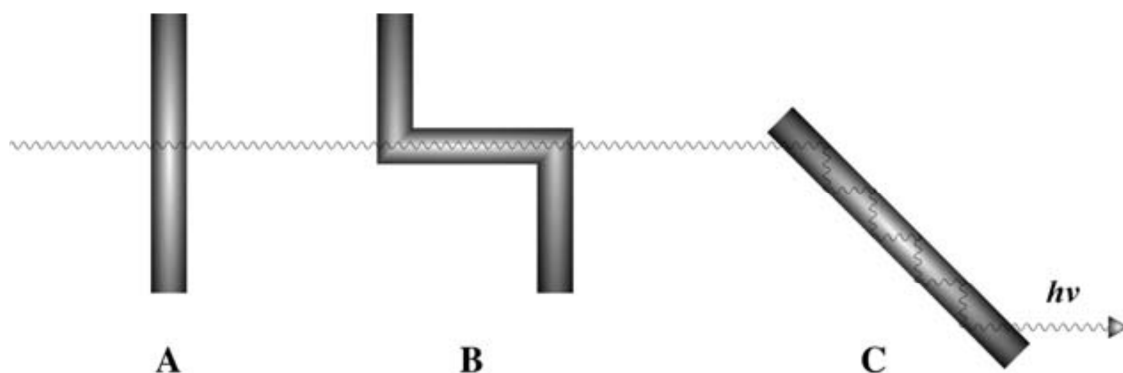


Figure 11. Increase in the absorption path length compared to single pass absorption in microfluidic devices. **(a)** Single pass absorption **(b)** Z-cell **(c)** Multipass reflection cell. Adapted from Wang et al.⁴¹

CRDS is a multiple pass absorption technique that lends itself well to gas phase measurements and has recently been adapted to detect liquid samples. One of the challenges of using CRDS in the condensed phase is getting the liquid into the cavity. In 1995 Zare and coworkers⁶⁰ handled this problem in the most straightforward manner by filling their 20 cm long cavity with 10-1 pM solutions of organic or inorganic absorbers. They achieved a detection limit of $\alpha_{\min} = 10^{-6} \text{ cm}^{-1}$ and ultimately showed that CRDS of solutions can be measured in a standard cavity ring-down configuration.⁶⁰ While effective, this technique is not very practical since the sample volume is rather large and needs to be carefully filtered and exchanged not to disturb the optical alignment. Alternatively, Xu et al.⁶⁰ minimized the detection volume and prevented

mirror damage by inserting two standard UV-VIS cuvettes into a 1 m cavity at the Brewster's angle. This technique worked well for samples with refractive indexes close to that of the cuvette, but fell short for aqueous solutions. Seetohul et al.⁶¹ and Van der Sneppen et al.⁶² performed similar techniques by inserting a HPLC U-cell into the cavity where detection limits of $1.9 \times 10^{-5} \text{ cm}^{-1}$ at 556 nm and $4.1 \times 10^{-4} \text{ cm}^{-1}$ at 355 nm were obtained with detection volumes of 70 μL and 80 μL respectively. Finally, Ubachs and coworkers⁶³ built a flow cell using two cavity mirrors and a rubber spacer. This experiment operated at 532 nm with a sample volume of 12 μL and a detection limit of $1.4 \times 10^{-4} \text{ cm}^{-1}$. While this method was successful, the short cavity length resulted in short ring-down times of 25 ns that needed temporal resolution with accuracy greater than 1 ns. While the reported CRDS techniques achieve very low detection limits, the detection volume is typically on the order of microliters, which is too large to be used in conjunction with micro-HPLC and CE. As well, the mirrors used in CRDS require wavelength specific samples, thus mirrored CRDS would not be the ideal method for resolving the wide variety of samples that HPLC separates.¹²

FLRDS presents itself as a viable absorption detection technique since fiber dimensions are comparable to those of flow channels in micro-separation systems and are a naturally broadband waveguide. The design of the sensor in these systems should resemble Figure 7(a) where light couples from one fiber to another across a gap. While the concept behind this sensor is straightforward, the configuration is not trivial. The fiber ends across the gap must be carefully aligned to achieve a good transmission and the flow channel must be connected without causing a build-up of pressure or introducing a dead volume.³³ If the fibers are laterally misaligned by

10%, they experience transmission losses of >10%. The alignment therefore requires a precision of 5 μm for a 50 μm core diameter multimode fiber, or <1 μm for a single mode fiber.^{32,64}

In one of their first FLRD experiments, the Looock group developed a prototype flow channel by placing a human hair (diameter \sim 50 μm) between the two ends of a 400 μm multimode fiber.³² The fiber ends with the hair were then submerged in a droplet of polydimethylsiloxane (PDMS). Twenty-four hours later, the PDMS solidified and the hair was removed, leaving a \sim 50 μm clear channel. Again, DDCI dye in DMSO was detected with a detection limit of approximately 10^{-10} mol or 7×10^{-8} g. In 2004 they performed a similar experiment using phase-shift FLRDS¹¹ where capillary flow measurements were made by joining the fibers with a commercial four-way microcross. The 100/140 μm fiber ends were inserted through opposite holes and the 100/360 μm capillary ends were inserted into the two other holes, leaving a gap between the fibers of approximately 31 μm . The separation between the fibers was later increased to 140 μm since it was found that shorter absorption paths lead to broader peaks using a 100 μm diameter capillary. A syringe pump with a flow speed of 166 nL/s injected DDCI through the interface and a detection limit of approximately 200 μm or 180 ppm was obtained.

In 2006 a similar system was designed by the Looock group⁶⁵ and used as an online detector for CE of biomolecules. Rather than using a commercial microcross, four holes were drilled into a polymethyl methacrylate (PMMA) block and the fiber and capillary ends were inserted and affixed using epoxy glue. One of the fiber ends was melted in the electric arc of a fusion splicer to form a microlens with a radius of 76 μm . The sample gap was approximately 30 μm and 810

nm light was introduced into the loop using a 99:1 coupler. Human serum albumin (HSA) was separated out from an unbound NIR dye and detected with a detection limit of 1.6 cm^{-1} or $1.67 \text{ }\mu\text{M}$.⁶⁵

The aforementioned experiments detected samples that absorb at approximately 810 nm, which goes hand in hand with the fact that NIR fibers exhibit the lowest losses. On the other hand, using lower wavelengths in the UV-VIS region expands the range of samples to detect. Andachi et al.³⁶ ventured into the visible region by constructing a 4.69 m loop out of multimode fiber (50 μm core diameter) where 660 nm light from a picosecond pulsed diode laser was coupled into the loop and out to a PMT using 99:1 couplers. Before entering the loop, the laser light was fed through two EDFAs in series to obtain stable and intense pulses of 40 ps by gain-switching. The sample, methylene blue, was introduced between the fiber ends via a microcell with a gap width of 100 μm and detection volume of 200 pL. The detection limit was determined to be 6 cm^{-1} or $50 \text{ }\mu\text{M}$.^{33,36}

Recently, the Loock group has configured a FLRD setup that operates at 405 nm.¹² The loop is constructed out of a low loss UV fiber (diameter 200/200 μm , absorption coefficient $\alpha_f = 0.011 \text{ m}^{-1}$ at 405 nm) with a large bend radius to minimize the loop losses. A PMT is mounted on this bend to detect the scattered light and the phase shift was read out by a lock-in amplifier at a sampling rate of 5 or 10 Hz. Phase-shift CRDS was used because of its higher data acquisition rate and because the short ring-down times are compensated with increased modulation frequencies. A special sample interface was constructed such that light could be coupled into the

loop at the same gap in the fiber where the sample is being measured (Figure 12). This was done by cutting two grooves in a PMMA polymer plate. One groove held the two loop fiber ends 190 μm apart from one another, the other groove, which was cut at a 6° angle from the sample gap, held the delivery fiber. This allowed for efficient coupling of light from the delivery fiber into the loop fiber core without the additional losses a commercial coupler would impose.

The sample entered the interface by traveling down a capillary through a hole drilled into the top plate in front of the delivery fiber. It subsequently flowed through the groove into the sample gap and exited through a hole that had been drilled beneath the gap in the fiber. The overall system had a detection volume of 6 nL, a ring-down time of 140 ns and an effective absorption path length of 550 μm . Measurements were taken of both tartrazine and myoglobin with respective detection limits of 5 μm (extinction, 0.11 cm^{-1}) and 1 μm .¹²

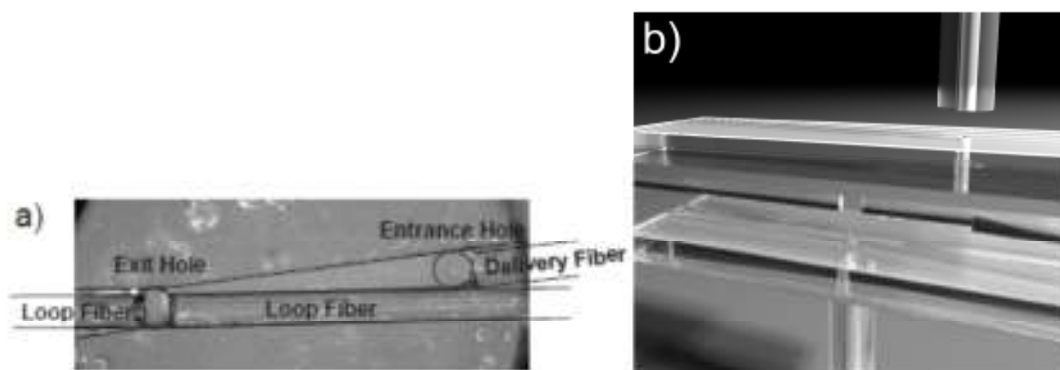


Figure 12. A custom built interface used to direct liquid between fiber ends and to couple light from the light source into the loop. Light enters the loop via the delivery fiber and the sample is injected through a hole in the top plate in front of the delivery fiber. (a) Top view. (b) Computer generated schematic image. Reproduced from Waechter et al.^{12,33}

1.7 Amplified CRDS

With respect to applications in broadband microanalysis, fiber loop ring-down spectroscopy is advantageous to standard CRDS and linear fiber CRDS. On the other hand, high losses due to couplers, splices, sample cells, etc. significantly compromise the loop's ring-down time, sensitivity and detection limit. Already in 2001, Stewart et al.⁴⁷ proposed FLRD in an amplified system since the added gain from a fiber amplifier may be able to compensate for all the undesired losses. In theory, this will result in ultra-long ring-down times and will consequently improve the detection limit and sensitivity. Under these ideal condition, Equation 1.3.2 is rewritten as Equation 1.7.1 to include the roundtrip gain, G , that is theoretically adjusted to exactly compensate the roundtrip losses, L_{sys} , while leaving the sample losses, L_{sample} , uncompensated. Since Equation 1.3.2 defines τ in a passive cavity where the losses are independent of light intensity, Equation 1.7.1 assumes the same towards the gain and that its fluctuations are negligible during the ring-down event.³³

$$\tau = \frac{t_{rt}}{-\ln(L_{sys} + L_{sample} - G)} \quad (1.7.1)$$

In an amplified experiment one may use pulsed CRDS, cw CRDS or ps CRDS to determine the ring-down time; however, if the gain in the loop is larger than the combined losses then the FLRDS system will become a fiber ring laser!⁴⁷

In all amplified FLRD experiments that will be discussed, EDFAs, which operate between 1520 – 1560 nm, are used as fiber amplifiers since their use in the telecommunications industry has made them commercially available. Conversely, other doped fiber amplifiers that

operate in other parts of the electromagnetic spectrum include fibers that are doped with thulium (1,460-1,530 nm or 800-850 nm), praseodymium (~ 1,300 nm), neodymium (~ 1 μm) and ytterbium (~ 1 μm) as the gain medium. Semiconductor optical amplifiers (SOAs) use a semiconductor gain medium to amplify signals – they are much like a laser diode where the mirrors have been replaced with antireflection coatings. SOA's offer gain up to ~15 dB, low polarization dependence (i.e. ~ 0.5 dB), amplification of light in the S, L and C bands and smooth gain profiles. The S, C and L bands are spectral regions spanning from 1460-1530nm, 1530-1565nm, and 1565-1625 nm respectfully. Although they are compact and cost effective, they are noisier and have a lower gain output than Re^{3+} doped amplifiers.

The first amplified FLRD experiment performed by Stewart et al. in 2001⁴⁷ used a 58 m fiber loop that included an EDFA (15-20 m of fiber), a bandpass filter (BPF), a variable optical attenuator (VOA), and a micro-optic cell (Figure 13). The fiber ends that defined the sample gap were fitted with GRIN lenses to increase their transmission efficiency. Amplified FLRD experiments were originally performed by sending in a laser pulse while the gain in the loop was kept below its lasing threshold, such that the decaying pulse was slightly amplified each time it passed through the EDFA. This was done by adjusting the loop losses using the variable optical attenuator. They originally achieved a ring-down time of 2.6 μs (round trip loss: 0.48 dB) and later with an improved setup a ring-down time of $10 \pm 2 \mu\text{s}$ (roundtrip loss $0.12 \pm 0.02 \text{ dB}$), but sample measurements were not taken since drifts in the amplifier gain resulted in variable ring-down times.^{47,48}

A loop with losses of 20.00% requires a gain factor of approximately 1.1999, and Stewart and Culshaw realised that they could circumvent their gain fluctuations by setting the gain *above* the lasing threshold such that the loop becomes a gain clamped free running laser.⁶⁶ In this experiment, the narrow bandpass filter (~ 1 nm) selects the lasing wavelength of the EDFA and the ring-down pulse is set to a slightly different wavelength that is still in the range of the BPF. Under these conditions, they recorded ring-down times ranging from 30 – 200 μ s (roundtrip loss of 0.004 dB) depending on the proximity of the wavelength of the DFB laser to that of the lasing wavelength. The longest ring-down times were recorded when the two wavelengths were near coincidence; however, relaxation oscillations increase in magnitude as the wavelengths approach one another. Fortunately, the excited state lifetime of Erbium is on the order of milliseconds thus they were able to extract the ring-down time from the first half of the oscillation cycle (Figure 14).⁶⁶ Nevertheless, one can see in Figure 14 that the ring-down trace is partially distorted from the oscillations and the unstable environment that they produce, thus limiting the reproducibility of the 200 μ s ring-down time. As well, there is a possibility that by keeping the probe wavelength so close to the lasing one, both loop and sample losses will experience compensation. Finally, one would experience difficulty recording a gas phase spectrum with the narrow BPF since the scanning range of the laser is limited to 1 nm.

Subsequently, to eliminate the low frequency distortion from the relaxation oscillations and the high frequency noise they replaced the BPF with a digital narrow BPF.⁶⁷ Impressive ring-down times of 10 ms were recorded (roundtrip losses of 0.00010 dB) with the consequence of increased variations (up to 30%) in the ring-down time. Much of these variations were caused by drifts in the lasing wavelength with respect to the DFB wavelength and mode-hopping of the

fiber laser.⁶⁷ Moreover, acquiring a spectrum was not trivial since it was necessary for the two wavelengths to be near coincidence; thus if the probe laser was scanned, so must the free running laser wavelength, which often produces more relaxation oscillations. Finally, Stewart et al. described an alternate setup, which could possibly overcome the problems discussed, using two nested loops that share the same amplifier but operate at different wavelengths.^{47,66} While it was noted in their first paper that they were investigating this setup and other variants of it, they later reported that balancing the two loops was not a trivial matter. After this point the two loop setup was abandoned for the simpler one loop setup.

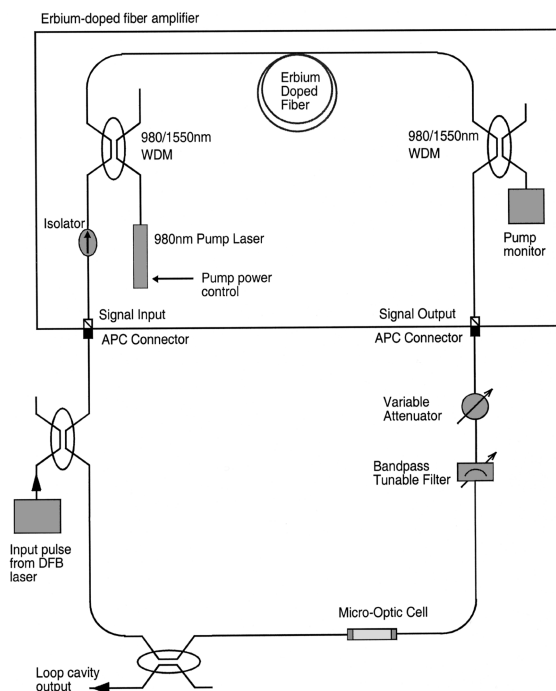


Figure 13. Amplified fiber loop ring-down cavity using an erbium doped fiber amplifier. Reproduced from Stewart et al.⁶⁶

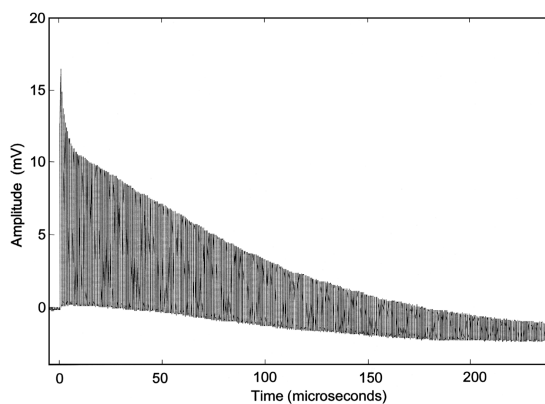


Figure 14. 100 μ s ring-down trace in a gain-clamped fiber cavity when the fiber's lasing wavelength and the pulse's wavelength are near coincidence. The baseline is distorted from the onset of relaxation oscillations in the amplifier gain medium. Reproduced from Stewart et al.⁶⁶

While Stewart et al.^{47,66,67} have not used their setup for analytical or spectroscopic

measurements, recent work by Ni et al. ⁶⁸⁻⁷⁰ adapted their method for gas phase spectroscopy and refractive index sensing.

Ni et al. developed an amplified FLRD setup similar to that of Stewart and co-workers that included two 50:50 couplers, a tunable gain EDFA, a tunable narrow BPF, a VOA, and a NIST standard gas cell. ⁶⁸ What differed was the addition of a digital least-mean-square filter that reduces ASE noise and improves the accuracy of the experiments. It does this by filtering the ring-down event with an estimation of the noise and subsequently, by using the least-mean-square algorithm, the filter improves its coefficients for noise estimation. Originally, the filter reduced the noise by 9 dB at a ring-down time of 2.7 μs and later, on a newer system, obtained ring-down times up to 101.2 μs (roundtrip loss of 0.218 dB). ⁶⁹ Measurements of the P(11) line on the $\nu_1-\nu_3$ combination band of acetylene were taken with a detection limit of 70.1 ppm and an accuracy of 15 ppm. Without the filter, the detection limit was 8.2 times larger. Additionally, Ni et al. used the same setup for refractive index change sensing with a long period grating, ⁷⁰ thus reconfirming the high configurability of FLRD and fiber optic sensors.

This thesis will revisit Stewart and Culshaw's work on the two loop setup with the intention of using it for FLRD measurements in the gas and liquid phases. Additionally, a variety of sensor interfaces will be explored to conduct these measurements, starting with a 6 cm long gas cell, hollow core photonic band-gap fibers and a fiber with a hole drilled in it. Finally, future experiments and alterations to the setup will be discussed.

Chapter 2

Theory

This chapter is organized as follows. First it will investigate the dynamics of the erbium doped fiber amplifier as well as the shape of its homogeneously and inhomogeneously broadened spectrum and how they relate to the experimental system. Thereafter the characteristics of of HC PBGs will be discussed. Finally, an overview of the practical reasons for sensing acetylene and ammonia as well as the relevant spectroscopy pertaining to the compounds will be reviewed.

2.1 The Erbium Doped Fiber Amplifier

The most common fiber in the telecommunications industry is the Corning single-mode fiber (SMF-28) and fibers with similar dimensions (i.e. $10.4 \pm 0.5 \mu\text{m}$ mode core diameter, $125 \pm 0.7 \mu\text{m}$ cladding diameters) and specifications (i.e. attenuations of 0.31-0.35 dB/km at 1380 nm and 0.19-0.20 dB/km at 1550 nm). All conventional silica waveguides have minimal losses at around 1550 nm. To enable long-haul optical data transmission the digitally encoded signal needs to be boosted at regular intervals. Erbium doped fiber amplifiers are one class of devices that helps boost the signal - semiconductor optical amplifiers are another. Erbium is element number 68 and part of the Lanthanide series in the periodic table. The stimulated emission from the $\text{Er}^{3+} \ ^{13}\text{I}_{3/2} \rightarrow \ ^{15}\text{I}_{3/2}$ transition centers around 1.5 μm , thus erbium doped silica fibers are optimal for amplifying attenuated signals in the telecommunication C-band.^{71,72}

2.1.1 Dynamics of Optical Amplification

EDFA's make use of a three level pumping scheme (Figure 15). This means that the Er^{3+} ions are excited from their ground state to the E_2 state through absorption of photons from the pump laser at 980 or 1480 nm. They quickly relax to a lower excited state (E_1). At the highest pump powers population inversion is possible and laser action can be observed throughout the broad gain spectrum of the EDFA at approximately 1.5 μm . The seed beam does not need to be an external source since seeding the amplifier with its own spontaneous emission – as was done by Stewart and co-workers^{47,66} – also induces stimulated emission. Without a signal beam, the stored energy is released as spontaneous emission.⁷³ The spontaneous emission of EDFA is broadband and ranges from approximately 1520 – 1580 nm. Stark splitting, homogenous broadening (i.e. all ions exhibit the same broadened spectrum) and inhomogeneous broadening (i.e. ions in different locations of the glass exhibit different spectra) determine the shape of this spectrum and this occurrence will be discussed later in this report.⁷¹

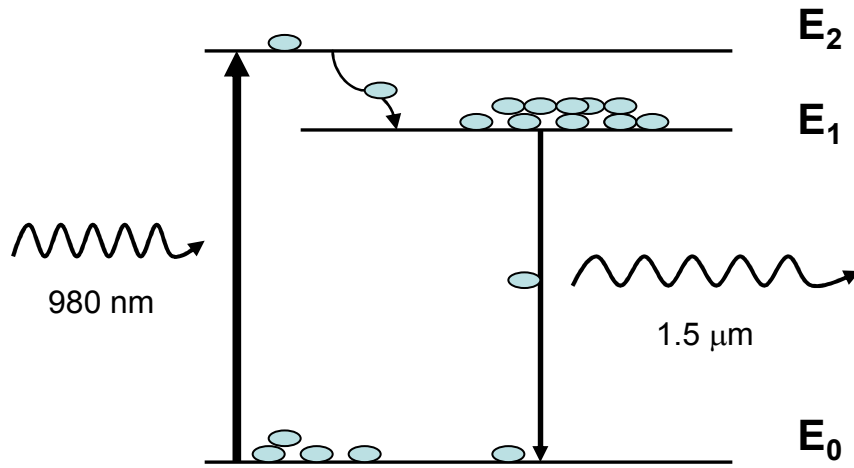


Figure 15. The three level pumping scheme that an EDFA utilizes to produce spontaneous and stimulated emission. 980 nm light excites the electron to E_2 where they quickly relax to E_1 . From there the stored energy is released as a broadband spectrum at $\sim 1.5 \mu\text{m}$.

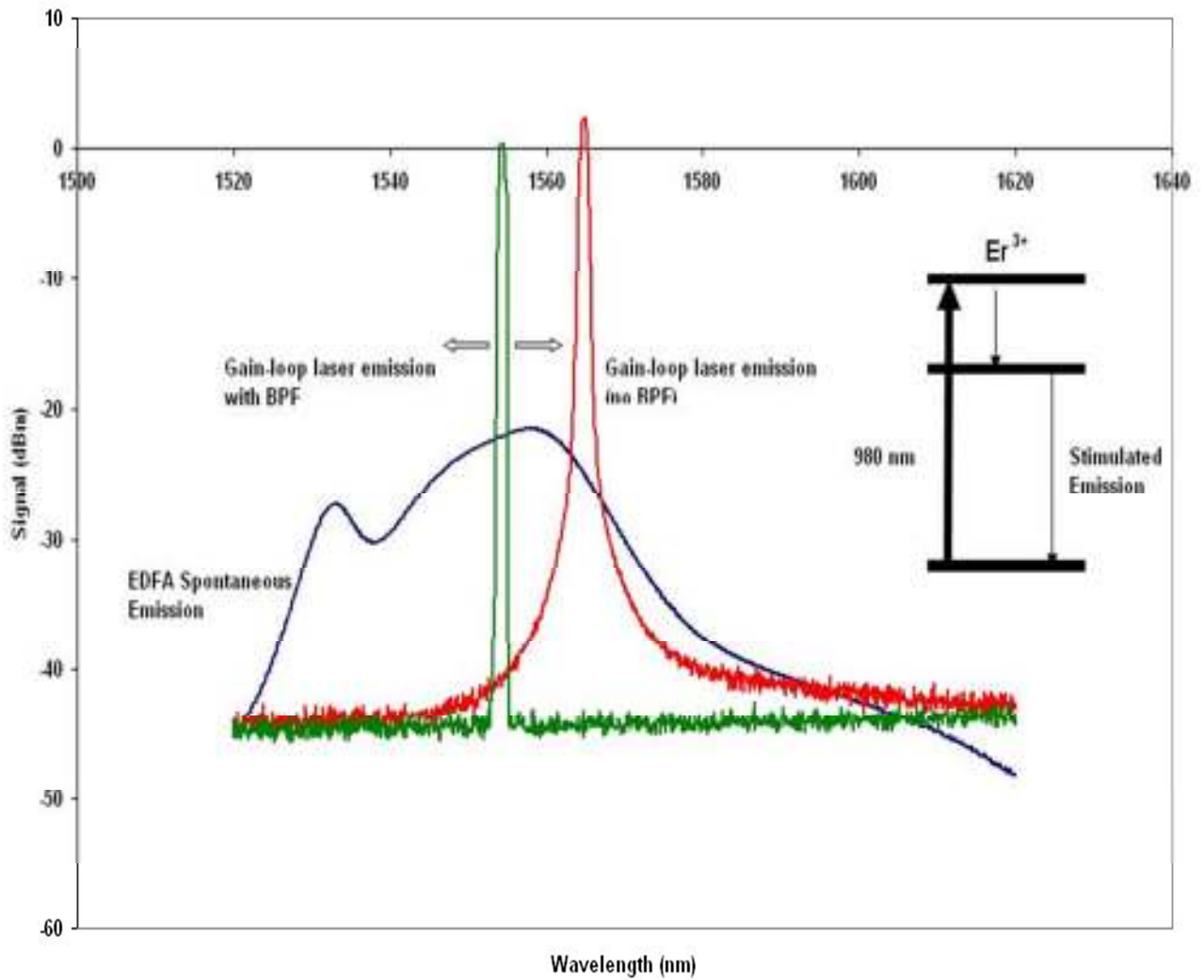


Figure 16. The blue trace shows the spontaneous emission spectrum produced by the EDFA used in our experiment. The red trace shows lasing action from the amplifier at ~1565 nm when the EDFA's output is also used to seed the amplifier. The green trace shows that if a tunable 1 nm BPF is placed in this loop, one can modify the wavelength at which lasing occurs. All spectra were recorded using an optical spectrum analyzer.

Quin ⁷³ used rate equations to model the behaviour of the EDFA population as it undergoes spontaneous and stimulated emission, pumping, and absorption. The rate equations for E_0 , E_1 and E_2 are shown in equation 2.1.1, 2.1.2 and 2.1.3 respectively.

$$\frac{dN_0}{dt} = \frac{N_1}{\tau_{10}} + W_s(N_1 - N_0) - W_p(N_0 - N_2) \quad 2.1.1$$

$$\frac{dN_1}{dt} = \frac{N_2}{\tau_{21}} - \frac{N_1}{\tau_{10}} - W_s(N_1 - N_0) \quad 2.1.2$$

$$\frac{dN_2}{dt} = -\frac{N_2}{\tau_{21}} + W_p(N_0 - N_2) \quad 2.1.3$$

Equation 3.1.1. shows that the population (N_0) on state E_0 is *increased* by spontaneous emission from E_1 with a time constant, τ_{10} as well as stimulated emission from E_1 in dependence on both the difference in population and the seed power W_s at 1.5 μm . The population in E_0 is *decreased* by pumping to E_2 - again a process that depends on the population differences between the respective levels as well as the pump power W_p at 980 nm. Similarly, N_1 is increased by spontaneous emission from E_2 with a time constant τ_{21} and is decreased both by spontaneous emission to the ground state, E_0 , as well as by the desired stimulated emission process (eq 3.1.2.). Finally, fast non-radiative transitions from E_2 to E_1 are responsible for a depopulation of N_2 , a level populated, of course, by pumping at a rate W_p , that depends on the pump photon flux. ⁷³

As mentioned earlier, a population inversion must be obtained for the amplifier to produce gain (i.e $N_1 > N_0$), the extent of the population inversion is expressed by the population inversion factor, n_{sp} , in Equation 2.1.4.

$$n_{sp} = \frac{N_1}{N_1 - N_0} \frac{\sigma_a}{\sigma_e} \equiv \frac{N_1}{N_1 - N_0} \quad 2.1.4$$

σ_a and σ_e are the absorption and emission cross-sections between states 1 and 0 respectively, but since $\frac{\sigma_a}{\sigma_e} \approx 1$ we can approximate the expression. Under steady state conditions, $\frac{dN_0}{dt} = 0$ thus

we write

$$\frac{N_1}{\tau_{10}} + W_s(N_1 - N_0) - W_p(N_0 - N_2) = 0 \quad 2.1.5$$

Since the relaxation from N_2 to N_1 happens extremely fast we will consider it an immediate process for the remainder of these calculations; thus the population N_2 is in thermal equilibrium with N_1 and can be obtained by the Boltzmann distribution.

$$N_2 = N_1 \exp\left\{-\frac{(E_2 - E_1)}{kT}\right\} = \beta N_1 \quad 2.1.6$$

Finally, by inserting equation 2.1.6 into equation 2.1.5, we can write n_{sp} as

$$n_{sp} = \frac{N_1}{N_1 - N_0} = \frac{W_p \tau_{10} + W_s \tau_{10}}{(1 - \beta)W_p \tau_{10} - 1} \quad 2.1.7$$

According to equation 2.1.7, a full population inversion occurs when n_{sp} is equal to one. In our experiment Er^{3+} is pumped with 980 nm light since, under the conditions of strong pumping ($W_p \tau_{10} \gg 1$) and a small signal ($W_s = 2.5 \times 10^{-5}$ W), 980 nm pumping can reach $n_{sp} = 1$, whereas at 1480 nm $n_{sp} < 1.6$.⁷³

2.1.2 The Shape of the Spontaneous Emission Spectrum

The shape of the emission spectrum (the blue curve in Figure 16) varies moderately from EDFA to EDFA, since it is closely related to the fiber composition, the addition of any codopants, and the local structure around the erbium ions. For a given EDFA it also depends on the pump wavelength and pump power. Most of the spectrum is inhomogeneously broadened because of site-to-site variation of rare earth ions (RE^{3+}) in the glass.⁷⁴ In an ideal system, the Er^{3+} ions would be homogeneously distributed in the host glass and fully coordinated to the silicon dioxide.

In reality, silica is a poor host for most RE^{3+} , which causes clustering of the erbium ions at distances of a few Ångstroms and allows them to interact over large distances of about 20-100 Ångstroms.⁷⁵ Homogenous broadening occurs from the ions interacting with the phonons of the glass; whereas inhomogeneous broadening results from Er-Er interactions, and incomplete coordination of the erbium ions to oxygen atoms. The different sites expose the ions to different electric fields, which shifts and splits the energy levels – this phenomenon is known as the Stark effect. The ground state, $J = 15/2$, is split into 8 sublevels and the first excited state, $J = 13/2$, is split into 7 sublevels; the transitions from these two shifted and split states are what are partly responsible for the inhomogeneously broadened part of the spectrum. To increase the coordination of Er^{3+} to oxygen atoms and reduce erbium clustering, most EDFAs are doped with erbium dioxide, which introduces non-bridging oxygen (NBO) atoms.⁷⁶ Still, the number of NBOs that come with erbium dioxide is insufficient for erbium ions to be homogeneously distributed; thus the Er^{3+} form clusters to share their oxygen coordination.⁷⁶ Moreover, studies have shown that sodium silicate glasses, which have a more open network structure, allow erbium ions to obtain higher coordination numbers.^{74,77} As well, co-doping with alumina or phosphorus reduces the Er-Er interactions by forming solvation shells around the Er^{3+} .

Figure 16 shows that our EDFA has quite a broad spontaneous emission spectrum. It is likely that this is because it is one of the earlier models; however we cannot confirm the type of fibers used and the presence of any co-dopants since all of the spec sheets have been lost by the manufacturer.

2.2 Background relating to Hollow-Core Photonic Band-gap Fibers

2.2.1 Overview

Conventional optical fibers guide light through total internal reflection. In a multimode fiber, the solid core has a higher refractive index than the cladding (Figure 17). Light reflects at an angle, θ , which is greater than the critical angle, θ_c , where $\theta_c = \arcsin\left(\frac{n_2}{n_1}\right)$ and is completely conserved – any loss in the light intensity is due to absorption or scattering from the waveguide material. While these fibers exhibit very low optical loss (3dB = 50% over a distance of 5 km), they are not the only option for guiding light. Interference phenomena can be used to guide light in a low refractive index medium; these waveguides have large potential especially for chemical sensing and spectroscopy but are also considered for low loss transmission of UV light. For example, anti-resonant reflecting optical waveguides (ARROW) are designs that consist of precisely manufactured dielectric coatings of alternating refractive indices.⁷⁸ These layers form a Fabry-Perot cavity in the vertical (transverse) direction, trapping the light inside the tube, and allowing single-mode propagation along the length of the ARROW. In 1999 Cregan and co-workers⁷⁹ developed a hollow-core (HC) single-mode waveguide that also uses Bragg interference to guide light in certain well defined wavelength bands (Figure 18). A fully two-dimensional photonic band gap (PBG) acts as the cladding, while the core of the waveguide is an open capillary containing a low refractive index medium such as air. To guide light successfully, the cladding must be a near perfect array of air holes with a small pitch. One can explain the differences in light guiding mechanisms between these fibers in terms of the wave propagation

constant, γ , which determines if the light propagates or is evanescent in any part of the waveguide – it is described as the ratio of the amplitude of the light at its source to its amplitude at distance x (Equation 2.2.1). γ is comprised of an attenuation constant, δ , and a phase constant, κ , as shown in Equation 2.2.2. The attenuation constant represents the decrease in an electromagnetic wave's intensity when traveling through a medium per unit of distance from the source; this relationship is shown in Equation 2.2.3. The phase constant is the imaginary part of γ and it describes the change in phase per meter along the path traveled by the wave at any instance in time – it is measured in units of radians per meter and is equal to the angular wavenumber of the wave (Equation 2.2.4) ⁷⁹

$$\frac{A_o}{A_x} = \exp(\gamma x) \quad 2.2.1$$

$$\gamma = \delta + i\kappa \quad 2.2.2$$

$$\left| \frac{A_o}{A_x} \right| = \exp(\delta x) \quad 2.2.3$$

$$\kappa = \frac{2\pi}{\lambda} \quad 2.2.4$$

If γ is smaller than the vacuum wave number, k , multiplied by the refractive index of the material, n , then $\gamma = kn \cos \theta$; if $\gamma > kn$, θ is imaginary and the light is evanescent. In a traditional single mode fiber, light propagates between kn_1 and kn_2 thus $kn_2 < \gamma < kn_1$; conversely, in a HC PBG $\gamma < kn_2$ since the light is traveling in all sub regions of the fiber and interfering with itself constructively to maintain the core light intensity. Although the transmission in HC PBGs is

limited by the same factors that affect solid core optical fibers (absorption, Rayleigh scattering, bending losses, confinement losses, and variations in the fiber structure), one can theoretically minimize these losses better than a conventional fiber, since scattering and absorption is reduced simply because the mode volume is largely located in the hollow core.^{80,81} While this is theoretically accurate, HC PBGs still have higher losses than conventional fibers because of variations in the fiber structure along its length, and from coupling of light from the air to confined surface modes on the glass.^{80,82}

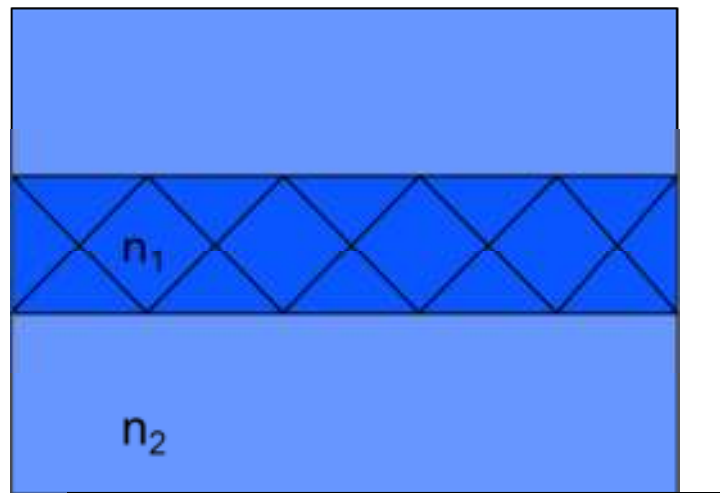


Figure 17. Light being guided in an optical fiber through total internal reflection, where $n_1 > n_2$ and $kn_2 < \gamma < kn_1$.

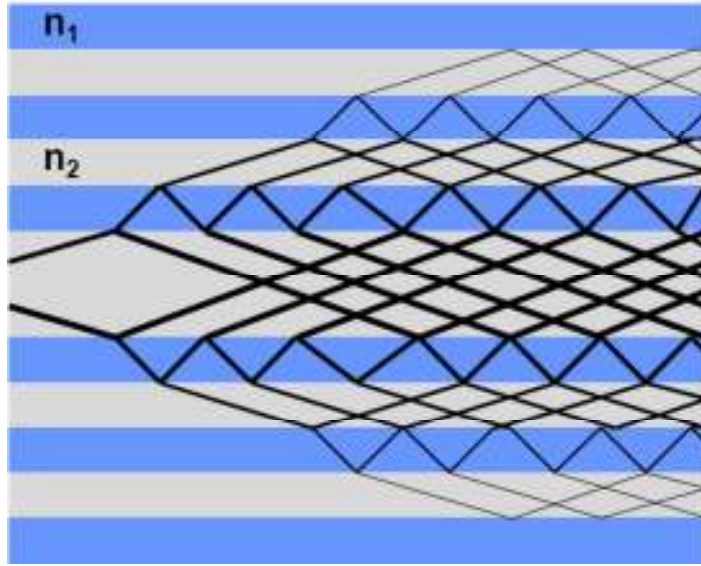


Figure 18. A cross-section of a hollow-core photonic band-gap fiber that guides light through the air filled core by periodic constructive interference of the light in the cladding. $n_1 > n_2$

Adapted from Cregan et al.⁷⁹

Types of HC PBGs

HC PBGs come in a variety of optical designs depending on the manufacturer and peak transmission of the fiber. In addition to the fiber used in the current experimental setup, NKT Photonics manufactures HC PBGs in the visible spectral range at 440, 532, 580 and 633 nm; in the 800 and 1060 nm range, and in the 2000 nm range. A variety of different types are produced for operation near 1550 nm. In general, the near IR and 800 nm fibers have a central hole diameter of $\sim 10.0 \pm 0.5 \mu\text{m}$, a pitch of $\sim 4.0 \pm 0.2 \mu\text{m}$, with losses of $<15\text{-}20 \text{ dB/km}$ at their central wavelengths – microstructured region diameters range from 70-76 μm at 1550 nm, 50 μm at 1060 nm and 40 μm at 800 nm. The HC PBGs operating at 2000 nm have core diameters of approximately $14.5 \pm 0.5 \mu\text{m}$, microstructured region diameters of 90 μm and have comparable losses of $<20 \text{ dB/km}$. Alternatively, the properties of the HC PBGs operating in the visible range differ from fiber to fiber. At shorter wavelengths the core and “holey” region diameter are reduced (i.e. $\sim 4.0 \pm 0.5 \mu\text{m}$ and $\sim 18\text{-}37 \mu\text{m}$ respectively) and the losses are significantly increased (i.e. $<2000 \text{ dB/km}$ at 440 and 532 nm, $<1000 \text{ dB}$ at 580 and 633 nm). Finally, at 1550 nm HC PBGs are available with enlarged core diameters of $\sim 20 \pm 2 \mu\text{m}$ and losses of $<10 \text{ dB/km}$, as well as polarization maintaining fibers with core diameters of $11.8 \pm 0.3 \mu\text{m}$ with losses of $<25 \text{ dB/km}$ – their pitch and holey region diameters are the same as the aforementioned HC PBGs that operate at 1550 nm. In addition to NKT, Corning also produces HC PBGs under the category of specialty fibers at wavelengths of 1060, 1300 and 1550 nm with core diameters of 8.5, 11.4 and 12.5 μm respectively and attenuations of $<100 \text{ dB/km}$.

2.3 Background of Acetylene

The overtone spectrum of acetylene lies in the telecommunication C-band (1530 -1565 nm) and plays an important role in the frequency calibration of many telecom light sources. Some devices even contain small acetylene gas cells and perform automated calibration routines – for example acetylene stabilized diode lasers use the rotational and vibrational transitions between $6493.5\text{-}6622.5\text{ cm}^{-1}$ for $^{12}\text{C}_2\text{H}_2$ and $6451.6\text{-}6578.9\text{ cm}^{-1}$ for $^{13}\text{C}_2\text{H}_2$ to establish working optical frequency standards. Frequency standards are obtained by locking the laser to an external optical cavity containing acetylene and the cavity is then locked to the Doppler-free acetylene signal by modulating the mirror positions.⁸³ Acetylene, $^1\text{H}^{12}\text{C}=\text{}^{12}\text{C}^1\text{H}$, is especially useful for frequency calibration since it has no hyperfine structure on the $\nu_1+\nu_3$ combination band, and consequently there is only one peak within each Doppler broadened transition.

2.3.1 The Ro-Vibrational Acetylene Spectrum

Acetylene, C_2H_2 , is a linear molecule with $D_{\infty h}$ symmetry and seven vibrational modes (Table 1). The three high-frequency modes are the symmetric C-H and C-C stretches (ν_1 and ν_2) and the C-H asymmetric stretch (ν_3). The remaining two modes are the doubly degenerate symmetric and asymmetric bends (ν_4 and ν_5).

Option	etry	l Mode	n
etric C-H Stretch			m ⁻¹
etric C-C Stretch			m ⁻¹
netric C-H Stretch			m ⁻¹
etric Bend			-1
netric Bend			-1

Table 1. Fundamental vibrational modes of acetylene. The arrows in the diagram refer to the most significant motions of the molecule. Adapted from Steinfeld, p. 245-248 ⁸⁴

In a normal vibrational mode all the atoms oscillate in phase and with the same frequency, and the vibrational motion of the molecule as a whole is described as a linear combination of these individual modes. ⁸⁵ The low-lying vibrational transitions of acetylene follow the selection rules for the harmonic oscillator (i.e. $\Delta v = \pm 1$), however it should be noted that anharmonicity in the potential well allows for other transitions to occur. ⁸⁵ The fundamental bands in a spectrum result from transitions from the ground state to the first excited state of a normal mode; overtone bands result from transitions from the ground state to the second (or higher) vibrationally excited state ($\Delta v > \pm 1$); combination bands result from one photon exciting two vibrational modes simultaneously. Finally, hot bands arise from transitions from one excited vibrational state to another, i.e. they follow the $\Delta v = \pm 1$ selection rule. In our experiments we recorded a portion of the $\nu_1 + \nu_3$ acetylene combination band. The spectrum that we will discuss

arises from photons in the near-IR region exciting electrons from the ground state of the ν_1 and ν_3 modes to their first excited state.

For a rigid linear molecule with no net orbital and spin angular momentum, the *classical* kinetic energy is equal to the square of the total angular momentum, J , (exclusive of nuclear spin) divided by two times the moment of inertia, I (Equation 2.3.1).⁸⁶

$$E_k = \frac{J^2}{2I} \quad 2.3.1$$

For a rigid rotor in free space there is no potential energy and the Hamiltonian operator only contains the kinetic energy term: $\hat{H} = \frac{\hat{J}^2}{2I}$. Schrödinger's equation is therefore:

$$\frac{\hat{J}^2 \psi_{MJ}}{2I} = \frac{J(J+1)\hbar^2 \psi_{MJ}}{2I} = BJ(J+1)\psi_{MJ} \quad 2.3.2$$

The energy eigenvalues are determined from the properties of the rotational wavefunctions, ψ_{MJ} , (spherical harmonic functions) and the rotational energy levels, $F(J)$ are quantized as $B J(J+1)$ (Equation 2.3.4), where J is the rotational (angular momentum) quantum number and B is the rotational constant

$$B = \frac{h}{8\pi^2 I} (\text{Hz})$$

$$B = \frac{h}{8\pi^2 c I} \times 10^{-2} (\text{cm}^{-1}) \quad 2.3.3$$

$$B = \frac{\hbar^2}{2I} (\text{joules})$$

$$F(J) = BJ(J+1) \quad 2.3.4$$

The selection rules for a rigid rotor molecule are $\Delta M = \pm 0, 1$ and $\Delta J = \pm 1$, however the molecule must have a permanent dipole moment, μ_0 , in order for any transitions to occur. Acetylene does not have a permanent dipole moment; therefore, it does not have a pure rotational spectrum.

Abiding by the selection rules, the rotational transition frequencies for linear molecules are equal to:

$$\begin{aligned} \nu_{J+1 \leftarrow J} &= F(J') - F(J'') \\ &= B(J+1)(J+2) - BJ(J+1) \\ &= 2B(J+1) \end{aligned} \quad 2.3.5$$

where each absorption line is separated by multiples of $2B$.⁸⁶

Moreover, the rigid rotor approximation does not take the effects of centrifugal distortion and vibrational coupling when determining the energy of the rotational transitions. Centrifugal distortion is accounted for by adding D , the centrifugal distortion constant, into Equation 2.3.4,

$$F(J) = BJ(J+1) - D[J(J+1)]^2 \quad 2.3.6$$

where,

$$D = \frac{4B_e^2}{\omega_e^2} \quad 2.3.7$$

ω_e is the equilibrium vibrational frequency and B_e is the equilibrium rotational constant.

Furthermore, the rotational constant also depends on the vibrational and electronic state.

Vibrations affect rotational transitions since they can change the molecule's moment of inertia. As one can see in Equation 2.3.3, B is dependent upon I , which depends on r , thus one must take vibrational coupling into account when calculating rotational transitions.

For a linear polyatomic and/or diatomic molecule, whose vibrational energy levels are modeled by an anharmonic oscillator, the average internuclear separation $\langle r \rangle$ of the atoms increase at

higher vibrational levels, v , thus each vibrational level has its own rotational constant, B_v , and centrifugal distortion constant, D_v .

$$B_v = \frac{h^2}{8\pi^2 \mu} \left\langle \frac{1}{r^2} \right\rangle \quad 2.3.8$$

So,

$$B_v = B_e - \alpha_e \left(v + \frac{1}{2} \right) + \gamma_e \left(v + \frac{1}{2} \right)^2 + \dots \quad 2.3.9$$

and

$$D_v = D_e + \beta_e \left(v + \frac{1}{2} \right) + \dots \quad 2.3.10$$

The rotational energy for a particular vibrational level v is now written as shown in Equation 2.3.11.⁸⁶

$$F_v(J) = B_v J(J+1) - D_v [J(J+1)]^2 + \dots \quad 2.3.11$$

The selection rules for ro-vibrational transitions are a combination of the vibrational and rotational selection rules. For a harmonic-oscillator rigid-rotor molecule they are simply, $\Delta v = \pm 1$ and $\Delta J = \pm 1$. For acetylene and other linear molecules with $X^1\Sigma^+$ symmetry, the rovibrational transitions form P and R branches, but lack a Q-branch. The R-branch is made up of $\Delta J = +1$ transitions and the P-branch lines of $\Delta J = -1$ transitions. Ignoring centrifugal distortion, the line positions for R and P transitions are given by:

$$\begin{aligned} \nu_R(v', J+1 \leftarrow v'', J) &= \nu_0 + 2B' + (3B' - B'')J + (B' - B'')J^2 \\ \nu_P(v', J-1 \leftarrow v'', J) &= \nu_0 - (B' + B'')J + (B' - B'')J^2 \end{aligned} \quad 2.3.12$$

where ν_0 is the band origin, as defined in Equation 2.3.13.

$$\nu_0 = G(v') - G(v'') \quad 2.3.13$$

where

$$G(v) = \omega_e \left(v + \frac{1}{2} \right) - \omega_e x_e \left(v + \frac{1}{2} \right)^2 + \omega_e y_e \left(v + \frac{1}{2} \right)^2 + \dots$$

As mentioned earlier, some vibrations change the molecule's moment of inertia, thus it is possible for a molecule that does not have a permanent dipole moment (i.e. acetylene) to have vibrational transitions. The molecular axis of acetylene lies along the z coordinate (Figure 19) so the transition dipole moment is parallel (μ_z) for stretching modes (i.e. $\Sigma - \Sigma$ transitions) and perpendicular (μ_x and μ_y) for bending modes (i.e. $\Pi - \Sigma$ transitions). One can see in Table 1 that ν_3 and ν_5 are the only IR active fundamental modes because of their u (ungerade = odd) symmetry. This may be best understood when considering that allowed vibrational transitions require that the integral $\langle v' | \mu | v'' \rangle$ has to have gerade symmetry, i.e. with a transition dipole moment which is ungerade by definition, the allowed transitions must obey the $u \leftrightarrow g$ selection rule.⁸⁶

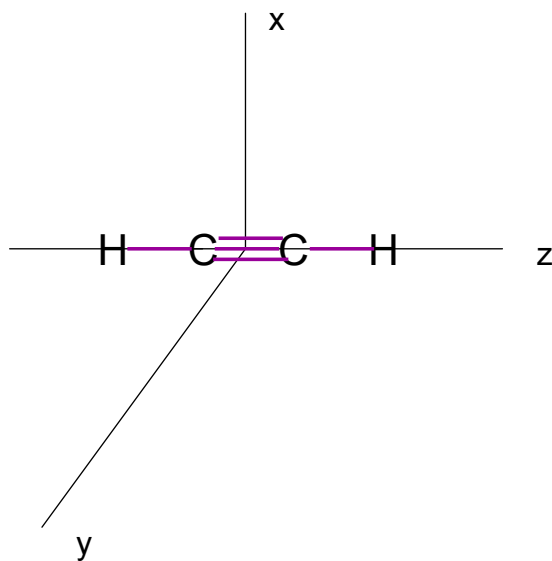


Figure 19. The molecular axis of acetylene, lying along the z coordinate.

2.3.2 Nuclear Spin Statistics of Acetylene

The dominant isotopomer of acetylene consists of ^1H and ^{12}C , which have respective nuclear spins, I , of $\frac{1}{2}$ and 0. Since ^{12}C has a nuclear spin of 0 the molecule exhibits the same nuclear spin statistics as $^1\text{H}_2$, the major difference being that acetylene's rotational levels are more closely spaced. The total wavefunction of this $D_{\infty h}$ molecule can be separated into electronic, vibrational, rotational and nuclear spin components (Equation 4.1.14). For $D_{\infty h}$ linear molecules $I = n + \frac{1}{2}$ where I is the nuclear spin and n is any integer or zero. Molecules with half integer nuclear spins are Fermions, thus exchanging any two nuclei that are equidistant from the centre of the molecule changes the sign of the total wavefunction.

$$\Psi_{total} = \Psi_e \Psi_v \Psi_r \Psi_{ns} \quad 2.3.14$$

Conversely, if I is a full integer value (i.e. $I = n$) then it is a boson and the total wavefunction is symmetric to nuclear exchange (i.e. Ψ_{total} does not change sign). In the case of acetylene, where Ψ_e and Ψ_v are in their ground states and symmetric to nuclear exchange, one must only consider the antisymmetric behaviour of Ψ_r and Ψ_{ns} . For even values of the rotational quantum number, J , Ψ_r is symmetric to exchange and for its odd values Ψ_r is antisymmetric.

Equation 2.3.15 shows the magnitude of the angular momentum due to nuclear spin; since ^1H has $I = \frac{1}{2}$, its quantum number, M_I , is either equal to $\frac{1}{2}$ or $-\frac{1}{2}$. The nuclear spin wavefunction is written as α or β , α corresponding to $M_I = \frac{1}{2}$ and β to $M_I = -\frac{1}{2}$. To differentiate between the two ^1H nuclei they are labeled as 1 & 2 and can have either α or β nuclear spin

wavefunctions. Equation 2.3.16 shows the four possible forms of ψ_{ns} for the molecule – it is apparent that three are symmetric and one is asymmetric to nuclear exchange.

$$P_l = [I(I + 1)^{\frac{1}{2}}] \hbar \quad 2.3.15$$

$$\psi_{ns} = \frac{1}{2^2} \left[\overbrace{\alpha(1)\alpha(2)}^{\text{Symmetric}} + \beta(1)\alpha(2) \right] \quad 2.3.16$$

$$\psi_{ns} = \frac{1}{2^2} \left[\overbrace{\alpha(1)\beta(1) - \beta(1)\alpha(2)}^{\text{Asymmetric}} \right]$$

In order for the nuclear exchange to be antisymmetric, the positive J values must be paired with the antisymmetric nuclear spin wavefunction and the negative J values are paired with the symmetric nuclear spin wavefunctions.

In other words, since there are three times as many symmetric spin wavefunctions, the antisymmetric rovibrational wavefunctions have a three-fold higher statistical weight compared to the symmetric rovibrational wavefunctions. Thereafter, it should be noted that the symmetry of the pure vibrational wavefunction is ungerade (odd) for the $v=0$ ground state and gerade (even) for the excited state of the combination band. As mentioned earlier, a change in the u/g symmetry of the vibrational wavefunction is imperative to induce a transition dipole moment such that combination band is IR active.

The selection rules for transitions from either odd or even- J rotational levels are given by $\Delta J = \pm 1$. Considering the symmetry selection rules for the vibrational transition itself ($u \leftrightarrow g$ and $g \leftrightarrow u$)

and the rovibrational transition including spin ($a \leftrightarrow a$, $s \leftrightarrow s$) it also is apparent that the spin states change as ($+ \leftrightarrow -$ and $- \leftrightarrow +$).⁸⁶

Figure 20 shows the allowed J transitions that would occur on the ν_3 fundamental mode and Figure 21 shows a portion of the $\nu_1 + \nu_3$ acetylene combination band where one can see the influence of nuclear spin statistics on the P- and R-band transitions.

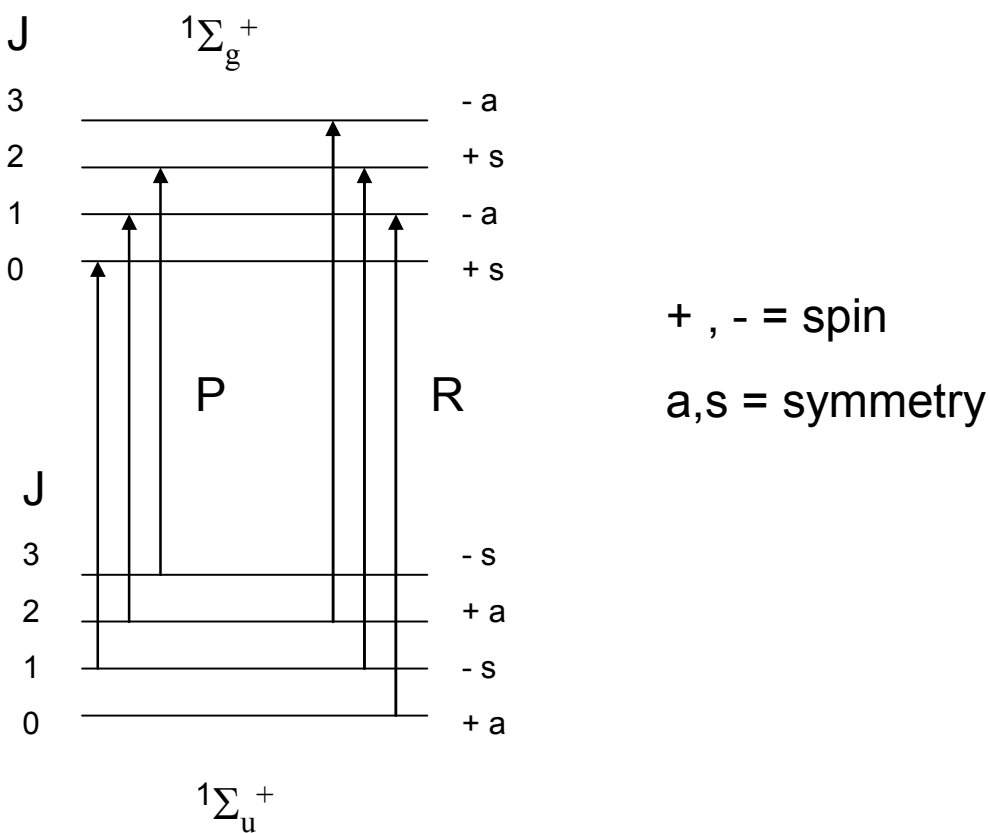


Figure 20. ν_3 fundamental mode P and R branch transitions. Selection rules of $\Delta J = \pm 1$, $+\leftrightarrow-$, $a \leftrightarrow a$, and $s \leftrightarrow s$ are maintained.

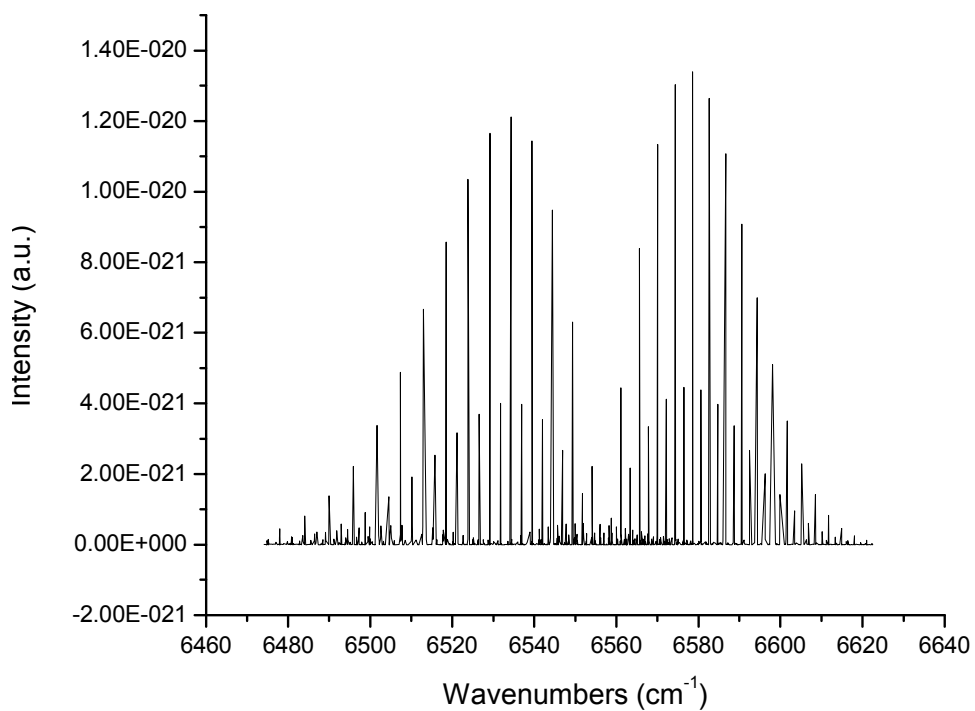


Figure 21. The P and R branches of the acetylene $\nu_1 + \nu_3$ combination band at 298 K, adapted from the HITRAN database.⁸⁷ One can see the effect of nuclear spin statistics on the even- J P and R branch transitions, which are three times less intense than the odd- J P and R transitions.

2.4 Background of Ammonia

Ammonia is a hazardous (i.e. Workplace exposure limit: 25 ppm time weighted average in an 8 hour work shift) and widely used gas in the fertilization and refrigeration industries. Additionally, it is used to remove NO_x produced from postcombustion gases and SO₂ that is created from burning fossil fuels; it is an anti-microbial agent for food products. As a result of its many applications ammonia is one of the most highly produced inorganic chemicals; nevertheless it is caustic and hazardous in nature and in industrial settings its concentration must be monitored. Ideally ammonia should be monitored *in situ* rather than along sampling lines where the sensor's ability to track transients can be hindered by salts formed by reactions between NH₃ and other flue gas constituents; ammonia decomposing in the sampling probes; and long gas transport times. FLRDS offers a sensitive and low cost solution for ammonia *in situ* monitoring in the near-IR region where some fairly intense and water-free rotational transitions on the $\nu_1 + \nu_3$ combination band and $2\nu_3$ overtone are found.⁸⁸ More so, the ability to detect ammonia in small volumes has a variety of biological applications. Neurochemical processes produce extracellular ammonia in submicromolar levels.^{89,90} At the present time fiber optic probe type sensors and flow-through fiber optic sensors are used to detect the ammonia in these processes by single pass absorption spectroscopy after it reacts with an indicator dye to in the following manner: $\text{NH}_3 + \text{HIn} \rightarrow \text{NH}_4^+ + \text{In}^-$.⁸⁹ Rather than sensing ammonia directly, the nonprotonated form of the indicator is detected. While the current flow-through systems are advantageous to the probe-type sensor configurations since they do away with the fragile tips and need for frequent calibration, they still use relatively large sample volumes (100 μL).⁹⁰ Chapter 3 of this report presents a fiber sensor interface with a 5.65 pL interrogation volume – this would

allow for higher concentrations of ammonia to be collected and detected without the use of an indicator by FLRDS, thus removing the need for instrument calibration and making routine operation easier.

Furthermore, there have been recent endeavours to detect ammonia in small volumes in the gas phase for breath analysis.^{91,92} It has been shown that patients with disturbed urea balance from kidney disorder and who suffer from *Helicobacter Pylori* bacterial stomach infections can exhale up to several hundred ppm of ammonia.⁹² CRD apparatuses present themselves as useful sensors since they can be selective to ammonia rather than the more prevalent oxygen and carbon dioxide lines.⁹¹ In this report two types of small volume gas interfaces will be discussed – a gas cell and a hollow-core photonic band gap fiber. These fiber CRD interfaces provide a low cost alternative to the mirror based interfaces that have been previously developed and may further be applied to the study the breath of small creatures.⁹³

2.4.1 Ammonia Ro-Vibrational Transitions

Ammonia is described by the C_{3v} symmetry group and has six fundamental vibrational modes, two of which are degenerate (Table 3). ν_1 is the doubly degenerate asymmetric stretch ν_2 is the symmetric stretch, ν_3 is the doubly degenerate bending mode, and ν_4 is the deformation mode.

Mode	Description	Symmetry Type	Normal Mode	Position
ν_1	Asymmetric Stretch	E		3464 cm^{-1}
ν_2	Symmetric Stretch	A ₁		3534 cm^{-1}
ν_3	Bend	E	<p>Top View</p>	1765 cm^{-1}

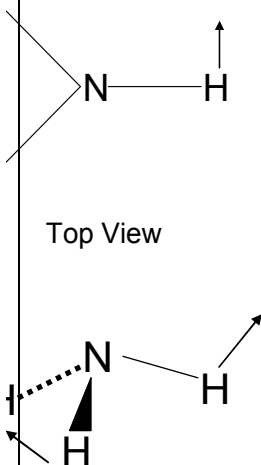
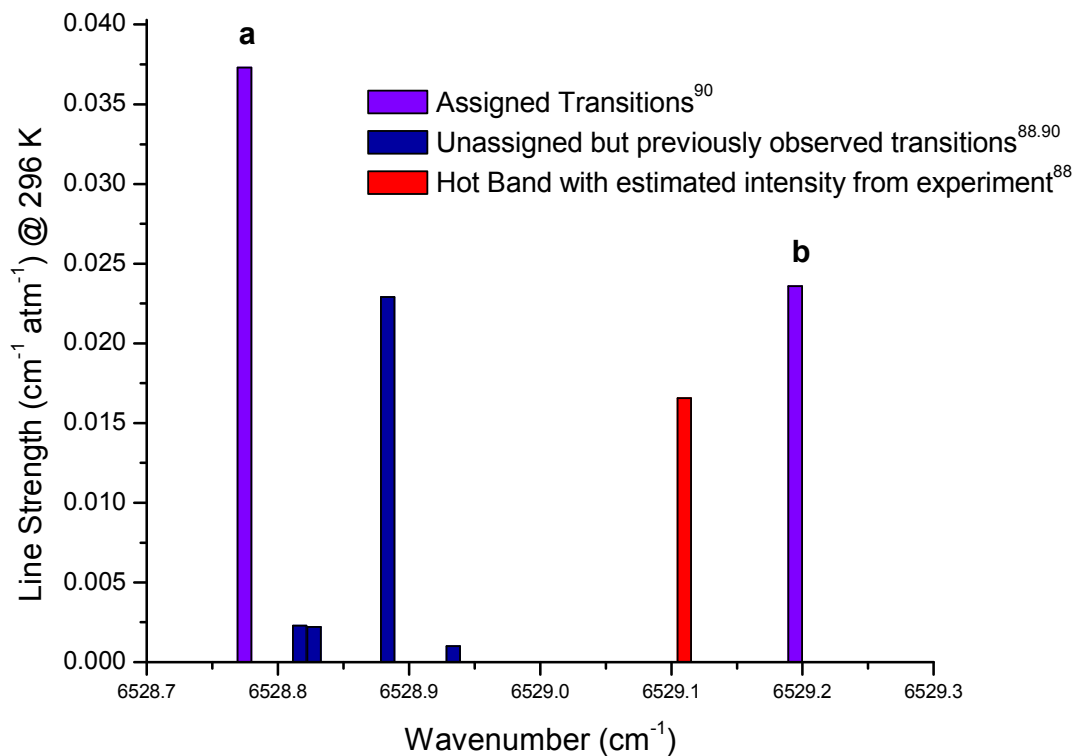
Mode	Description	Character Type	Normal Mode	Position
ν_4	umbrella inversion	A_1		1139 cm^{-1}

Table 2. Fundamental vibrational modes of ammonia. The arrows in the diagram refer to the most significant motions of the molecule. Adapted from Kiprof. ⁹⁴

In the near IR region ammonia has a very dense spectrum, due to numerous overtone and combination bands. Between 1450-1560 nm (i.e. $\sim 6400\text{--}6900\text{ cm}^{-1}$) Lundsberg-Nielsen et al.⁹⁵ identified 1710 absorption lines and assigned 381 of them to rovibrational transitions of the $2\nu_3$ overtone and $\nu_1+\nu_3$ combination band. Later, Webber et al.⁸⁸ determined which lines have the least interference with the water absorption spectrum and would be most suitable for monitoring ammonia. We have chosen to look at the lines in the region of $\sim 6528.7 - 6529.3\text{ cm}^{-1}$ (i.e. $\sim 1531.558 - 1531.699\text{ nm}$) since they are relatively intense transitions that fall within the range of our BPF, and are free of overlap with any water lines (Figure 22).^{88,95}

Ammonia $\nu_1-\nu_3$ combination band and $2\nu_3$ overtone transitions



Line	J	K'	J''	K''	σ	Transition	E''
a	4	2	5	3	a	$\nu_1-\nu_3$	265.23
b	4	2	5	3	s	$2\nu_3$	264.52

J',K' - upper-state symmetric top rotational quantum numbers⁸⁸

J'',K'' - lower-state symmetric top rotational quantum numbers⁸⁸

E'' - lower-state energy (cm^{-1}) based on transition assignment⁸⁸

Figure 22. The assigned, unassigned and calculated $2\nu_3$ and $\nu_1+\nu_3$ transitions for ammonia. The assigned lines, a and b, have asymmetric and symmetric nuclear symmetry, respectively.

As mentioned earlier, B is dependent upon I , which has three principal axes: I_c , I_b and I_a . Where c the axis about which I has its maximum value, a is the axis about which it has a minimum value (they lie perpendicular to one another) and b is the axis perpendicular to the both c and a .

Equation 2.4.1 shows that in a linear molecule there is only one value for I , thus the term values, $F(J)$, are only dependent upon one set of rotational quantum numbers, J .

$$I_c = I_b > I_a = 0 \quad 2.4.1$$

On the other hand, oblate symmetric rotors like ammonia have two I values since

$$I_c > I_b = I_a \quad 2.4.2$$

Thus the rotational quantum number J corresponds to I_c , and the rotational quantum number K corresponds to I_a and I_b – thereby making it doubly degenerate with respect to the clockwise or anticlockwise rotation about the a or b axes. When $K=0$ it is not degenerate since there is no angular momentum about the a or b axes. Equation 2.4.3 gives the rotational term values for ammonia.

$$F(J, K) = BJ(J + 1) + (C - B)K^2 \quad 2.4.3$$

2.4.2 Determining the partial pressure of Ammonia in an ammonium hydroxide solution

The experiments that required ammonia were conducted by bubbling helium through different concentrations of ammonium hydroxide (i.e. different percent weights of ammonia dissolved in water). By interpolating and extrapolating the results collected by Perman,⁹⁶ who measured the partial pressures of ammonia and water in different aqueous ammonia solutions at temperatures ranging from 0 – 60 °C, we were able to determine the concentrations of gaseous ammonia swept through the gas cell. Perman's results can be seen in Table 1. An alternative method for determining the ammonia partial pressures would be to calculate them using Henry's Law (Equation 2.2.1), which assumes a linear relationship between the concentration of the gas dissolved in water and its vapour pressure with respect to Henry's law constant, k_H . k_H is a function of the temperature, the solute and the solvent – it is experimentally determined and its values for different gases can be found on the NIST chemistry webbook.

$$p = k_H c \quad 2.2.1$$

When plotted, Perman's results show that the vapour pressure of ammonia does not increase linearly with respect to its concentration in solution; rather the relationship can be fitted using a second-order polynomial. This phenomenon is due to the formation of hydrogen bonds between the water and ammonia molecules, which limits the amount of ammonia vapour at lower ammonia concentrations.

°C		
H ₃		

Table 3. Experimental values of partial pressures (pp) of ammonia and water (in units of Torr) with respect to the percent weight of ammonia dissolved in water at 19.9°C. Adapted from Perman.⁹⁶

Chapter 3

Experimental

This chapter will describe the experimental setup as a whole and take a more detailed look at the individual sensor interfaces – their construction and the computer programs used for data acquisition.

3.1 Experimental Overview

In 2001 Stewart and Culshaw explored the properties of an amplified fiber loop ring-down setup.⁴⁷ Their setup was based on a modified fiber ring laser that was operated below the lasing threshold, i.e. instead of a loop gain the fiber ring cavity exhibited a gradual ring-down time of $\tau = 2.6 \mu\text{s}$, and with an improved setup $10 \pm 2 \mu\text{s}$.^{47,66} This setup can be seen in Figure 13, where a narrow tunable bandpass filter is used to select the output wavelength of the EDFA and a variable attenuator is used to control the amount of gain in the loop. In this first paper, they note that the instability of the system due to gain fluctuations can be solved in one of two ways. The first method was the one that they pursued; the gain of the loop was set above the lasing threshold at a wavelength set by a bandpass filter, and the laser loop was seeded by a probe laser tuned to a slightly different wavelength within the pass band of the bandpass filter. Since the gain is clamped by the amplified spontaneous emission, the loop cavity rings down at a slightly different seed laser wavelength.⁶⁶ The second method proposed the construction of two nested loops that share the same EDFA gain medium; one loop acted as the gain stabilization loop, in which gain clamping was again achieved through laser action, and the other loop, which may be equipped with a sample cell, could be used for ring-down measurements (Figure 23).

Balancing the gain such that the ring-down loop operates just below the lasing threshold will compensate for all intrinsic losses; thus, all recorded losses will be due to sample absorption. While this setup appeared theoretically sound, in practice Stewart, Culshaw and coworkers found that balancing the stabilization loop above the lasing threshold with the ring-down loop just below threshold was not a trivial matter; therefore their project was abandoned.⁶⁶

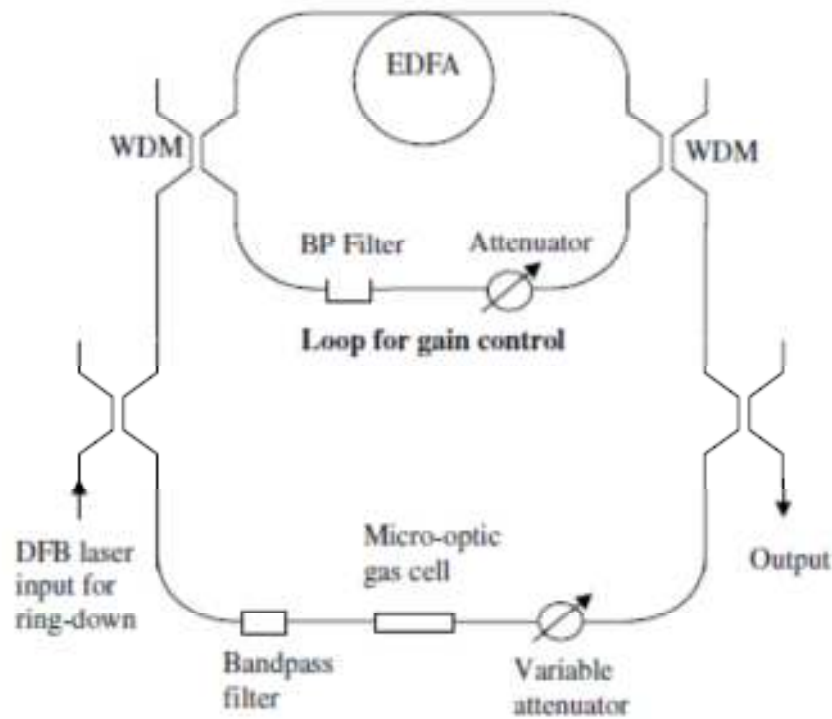


Figure 23. Gain stabilization using a secondary lasing loop. Reproduced from Stewart et al.⁴⁷

Upon the commencement of my graduate studies we revisited Stewart et al.’s nested loop setup (Figures 24 and 25). Like their original proposal, we used a variable optical attenuator to modify the balance in gain between the two loops by increasing or decreasing the amount of loss in the inner loop. Two tunable narrow band-pass filters (Newport TBF-1550-1.0) were used to

prevent cross-talk between the two loops with the outer one set to the same wavelength as the tunable diode laser (TDL) (Ando AQ 4320 D). On average, to achieve maximum amplification of the laser light, the EDFA (Keopsys, model number OI-BT-C-18-Sd-B-GP-FA), was pumped at 0.55 A (maximum 0.60 A). The light from the inner loop, outer loop and TDL were coupled out to an optical spectrum analyzer (OSA) (Anritsu Model MS9710C) so that the relative intensity of the signals could be monitored as well as their respective wavelengths. We performed experiments by modulating the intensity of the TDL intensity with its “internal chop” setting and by splitting the detector signal to both a lock-in amplifier (Stanford Research Systems SR830) and an oscilloscope – this allowed for both time and frequency domain experiments to be conducted. Moreover, we recorded ϕ_0 by disconnecting the fc connector that joined the 95/5 coupler after the detector to the sensor interface. Finally, at ~1530-1540 nm the BPF exhibits substantial polarization sensitive losses, a polarization controller (Thorlabs FPC030) was inserted in the outer loop to rectify any birefringence induced by the 50/50 coupler.

This setup originally contained a 6 cm gas cell enclosed around the two graded-index (GRIN) rod lenses that were mounted on an x-y-z-translation stage. Subsequently, we replaced the gas cell with a photonic band-gap fiber to perform gas phase measurements in a smaller volume with an increased path length. Later this was replaced by a fiber with a hole drilled in it for the detection of liquids in pico-liter volumes.

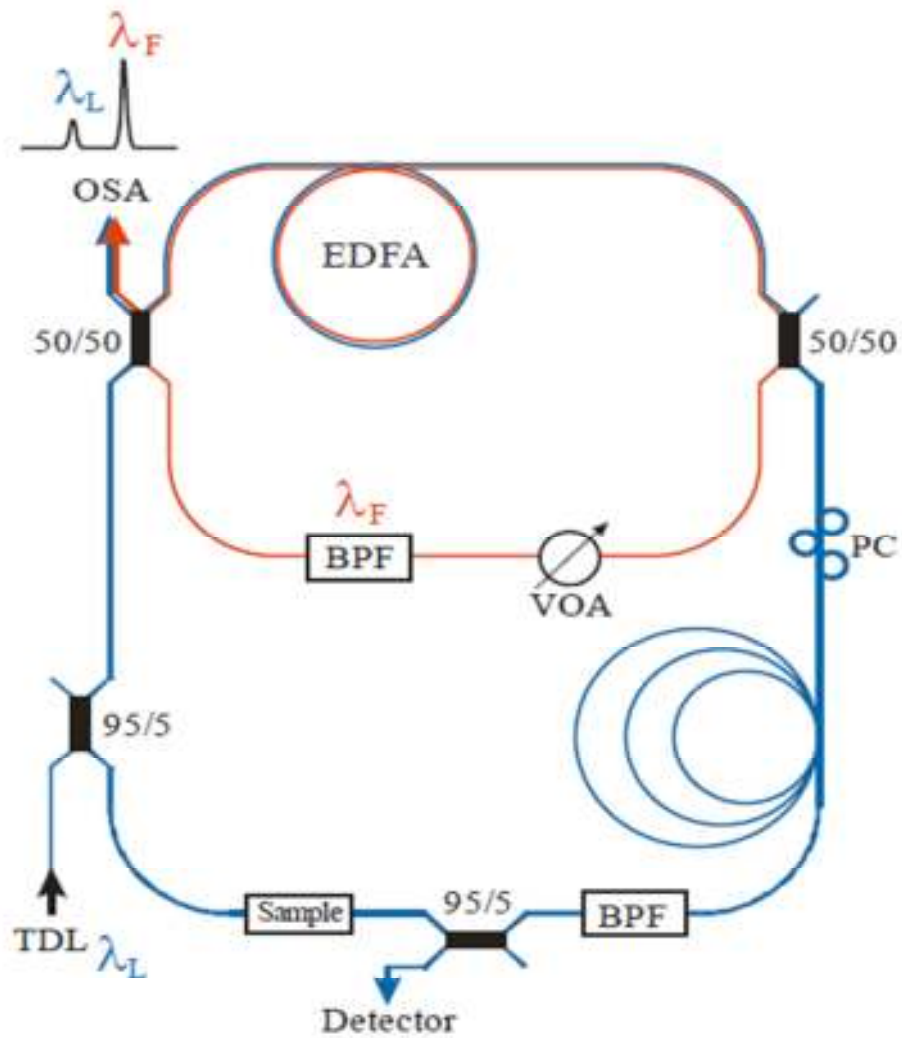


Figure 24. The amplified two loop setup. The inner-loop is clamped to its gain threshold, while the outer -loop is used for sample measurements and operates just below its gain threshold.

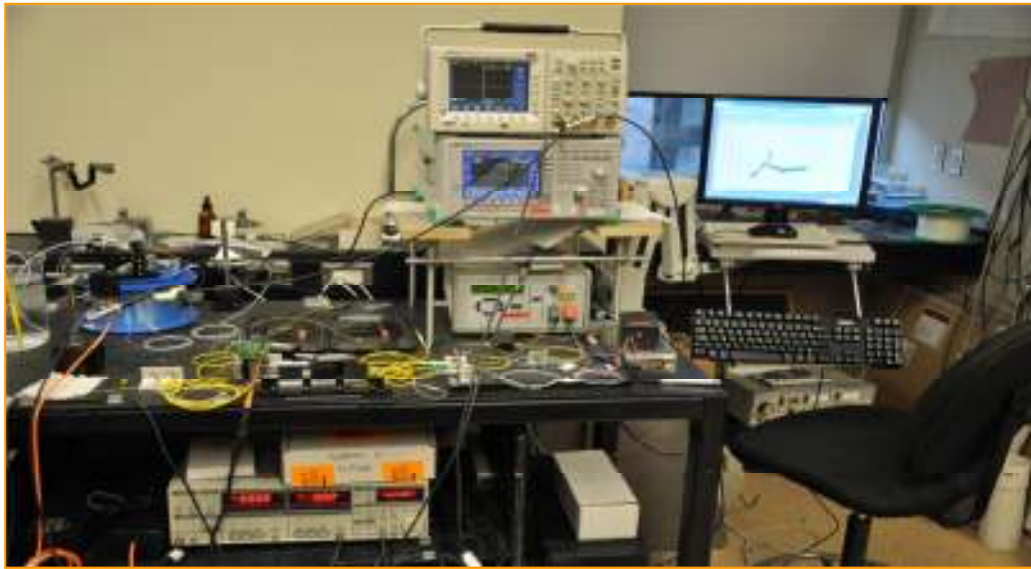


Figure 25. A photo of the experimental setup.

3.2 The Gas Cell

As previously stated, the gas cell was constructed around two fibers with GRIN lenses on an x- y-z-translation stage. Initially we tried to couple light across a ~1 cm gap using fibers with microlenses, similar to those used by Li et al. on a 30 μm gap,⁶⁵ however the transmission across the gap was too small at this larger distance. Fibers with GRIN lenses were then used because of their ability to collimate light from one fiber to the other over centimeter-long distances (Figure 26).⁹⁷ Unlike a confocal arrangement, for which the gap between the fibers is fixed at a distance that is identical to the lenses' focal distances, the refractive index of the GRIN lens varies – this bends the light exiting the fiber at different trajectories such that they rays are largely parallel to one another – thus allowing for a wider separation between the fibers. To reduce the sample gap losses, lateral offsets in the x and y directions were minimized and the stage was manually adjusted to remove any angular tilt. Finally, the fibers were set 6 cm apart and encased in a gas cell.

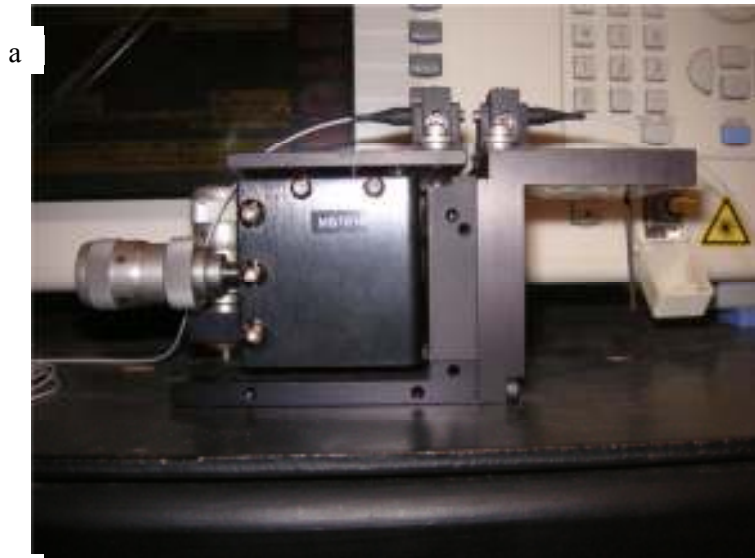


Figure 26. (a) side and (b) top view of the stage. The left platform is mobile in the x, y and z directions and can be adjusted using the three micrometer screws. (c) Photo of the 6 cm gas cell encasing the two fiber ends.

In chapter 4, experiments are described that measured the intensity and lineshape of transitions on the acetylene and ammonia $\nu_1+\nu_3$ combination bands as well as lines on the ammonia $2\nu_3$ overtone. We used a gas cylinder containing a mixture of 1000 ppm of acetylene in helium as our acetylene source (PRAXAIR, 1000 ppm C_2H_2 in He, non-certified standard grade), and used a flow meter to dilute the gas down to the desired concentrations. On the other hand, we obtained gaseous ammonia by bubbling helium through different concentrations of ammonium hydroxide and used Perman's experimental results to check our vapour pressures (see section 2.4.2). The ammonium hydroxide used was from Sigma-Aldrich, ACS reagent grade, with 28.0-30.0 % NH_3 by weight.

3.3 Hollow-Core Photonic Band-Gap Fibers as Gas Sensors

HC PBG Fibers are naturally air- or gas-filled optical waveguides, thus they can also be filled with analyte gases and be used to conduct spectroscopy of e.g. acetylene, hydrogen cyanide,⁹⁸ ammonia⁹⁹ and methane.¹⁰⁰ These gases have absorption features in the wavelength regions of commercial HC PBG fibers.

Implementing HC PBGs as a gas cell in any fiber optic sensing device faces the challenges of efficiently coupling light into the HC PBG from the delivery fibers, as well as filling the fiber with gas to a desired pressure.¹⁰¹ In general, this is done by using optics to couple light from one type of fiber to the other, or by splicing the two together.^{102,103} If a good splice is achieved (i.e. <1 dB loss) one can be assured that light will be efficiently coupled into the HC PBG; on the other hand, it is very difficult to properly splice a single-mode fiber to a HC PBG fiber. Most importantly, the HC PBG can only be filled once and to a single pressure with little precision.

In the experiment described in chapter 4 we constructed a gas cell with 60 cm of HC-1550-04 PCF from NKT Photonics (core diameter of $10.6 \pm 0.3 \mu\text{m}$, pitch of $4.1 \pm 0.1 \mu\text{m}$, and center wavelength of $1535 \pm 5 \text{ nm}$). Our interface is modeled after the one presented by Feurer and coworkers in 2010¹⁰¹ where both the traditional SM fiber and the HC PBG were sealed in a polished fiber optic ferrule. Much like an fc connector, the two fibers were aligned and held together by a split ceramic sleeve. The interface was then confined within a gas tight adaptor, which was attached to a pump, a pressure gauge and a gas inlet flow tube.

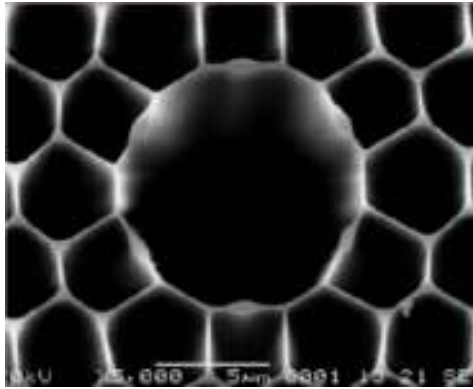


Figure 27. A photograph of the HC PBG used as the gas-sensing device in the current setup. Core diameter of $10.6 \pm 0.3 \mu\text{m}$, pitch of $4.1 \pm 0.2 \mu\text{m}$, centre hole diameter of $76 \mu\text{m}$, cladding diameter of $121 \pm 2 \mu\text{m}$, coating diameter of $220 \pm 50 \mu\text{m}$ and a transmission maximum centered around $1535 \pm 5 \text{ nm}$.

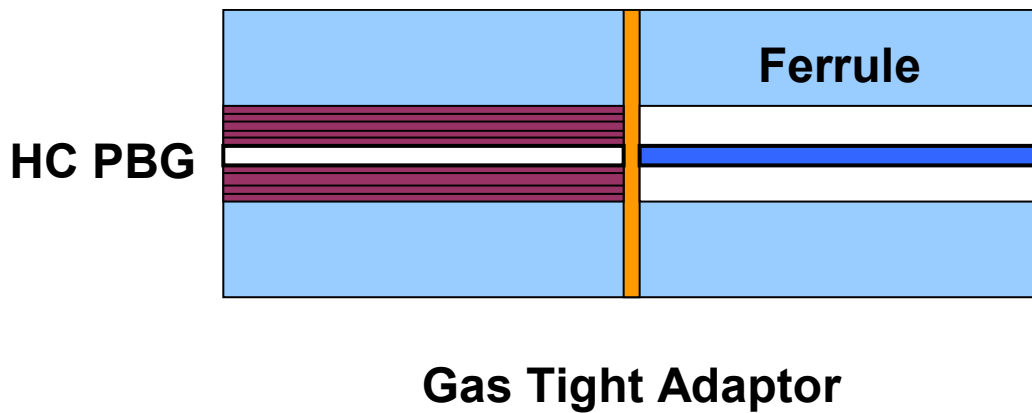


Figure 28. HC PBG – SM fiber interface modeled after the one used by Feurer and coworkers.¹⁰¹

3.4 Fiber with a Hole

The third sensor interface was a single mode fiber with a hole drilled in it (Figure 29) – this was made by researchers at the Institute National d'Optique (INO, Quebec, QC) using laser-drilling with a pulsed CO₂ laser. The hole has a diameter of ~30 μm and the interrogation volume is calculated as 5.65 pL.¹⁰⁴

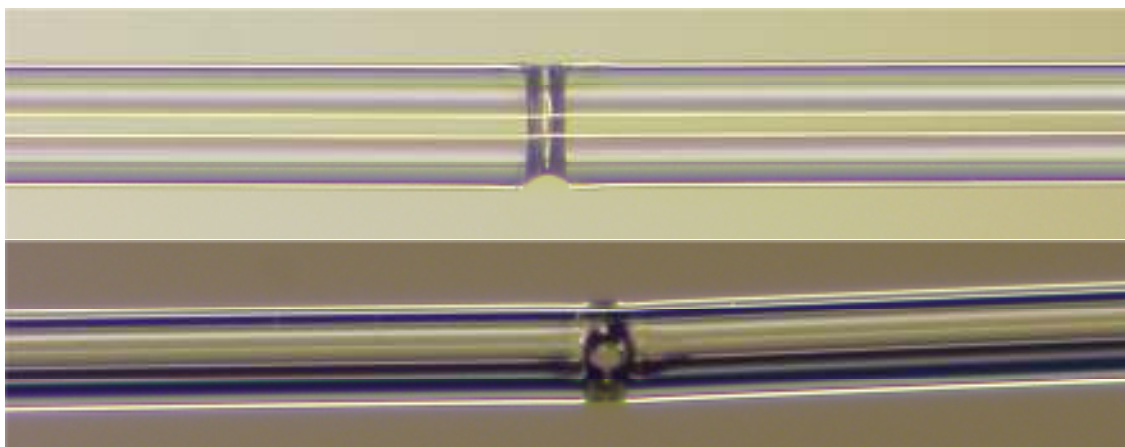
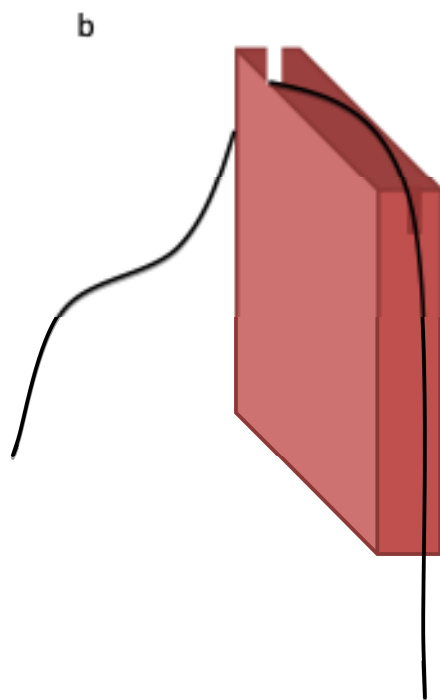
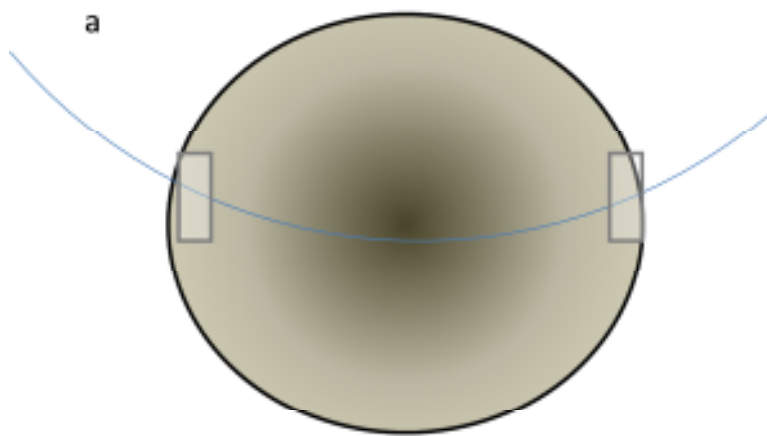


Figure 29. A single mode fiber with a hole drilled in it, supplied by INO. The fiber has a calculated interrogation volume of ~5.65 pL.

Measurements were originally taken by taping the highly delicate fiber onto a watch glass and submerging the hole in different solvents. Thereafter, we placed the sensor in a Teflon trough with grooves down the sides so the fiber could lay flat while being submerged in liquid (Figure 30).



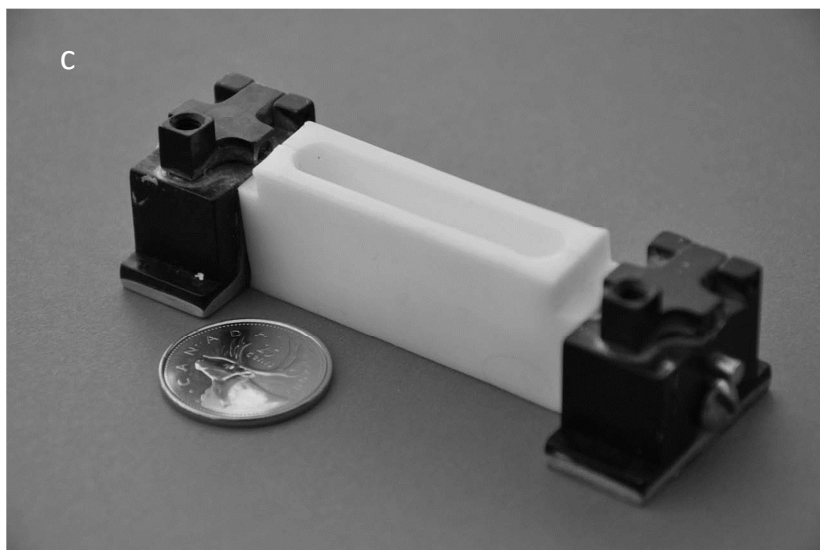


Figure 30. (a) The fiber with a hole taped down onto a watch glass. Chemicals were poured on top of the hole until it was completely submerged. (b) The Teflon trough with side grooves to thread the fiber through. This interface allowed for the exchange of chemicals without having to remove the fiber. (c) A photo of the Teflon trough.

3.5 Measurements

The experiments in this report were conducted using LabVIEW programs that I wrote by incorporating the data acquisition (DAQ) hardware's LabVIEW programs – the so-called Virtual Instruments (VI) - into larger programs that both recorded data and stepped the laser (DAQ used – Measurement and Computing USB-1408FS). The laser was controlled via a GPIB to USB connection - National Instruments GPIB-USB-HS, part number 778927-01). We recorded the ring-down times by copying the time traces from the oscilloscope onto a USB stick and fitting them with the bi-exponential decay fitting parameter found in *Microcal Origin 6.0* software. Gas phase measurements were conducted using the phase shift technique: the modulation frequency was set close to $\frac{2\pi}{\tau}$; the laser was stepped across the wavelength of the absorption feature; 10 phase shift measurements were recorded at each wavelength step; the lock-in amplifier was set to a time constant of 100 ms. The program used to record these results is titled 'single peak scans.vi.' Its front panel allows the user to enter a file path for the collected data to be saved to; as well there are boxes where one must enter the sampling rate per second, the total number of samples to collect, which channel on the DAQ one is using, the starting wavelength of the laser, the total number of wavelength steps and their step size. The program is set up in two steps – the first one sets the wavelength of the laser and the second one acquires the data. Initially, the laser wavelength is set to whatever the user has defined the starting wavelength to be, and then the total number of samples is collected at the rate that is defined by the user on the front panel. For this experiment we chose to sample 10 samples per second with the total number of samples to collect being 10, thus one sample was collected every 100 ms.

Thereafter, the laser wavelength is stepped by one user-defined increment and another 10 samples are collected – this loop repeats itself until the desired number of wavelength steps have been completed.

On the other hand, liquid phase measurements were conducted at a single wavelength. We recorded the phase shift every second over the course of 3 minutes and then averaged the values. These measurements were conducted using the program titled ‘Pressure vs time.vi.’ This program was initially designed to measure the pressure off the pressure gauge on the HC PBG sensor interface and was later applied to measure the phase shift from the lock-in amplifier for the liquid phase experiments. The front panel of this program allows one to set a file path, the DAQ channel that is being used, the sample rate per second, the total number of samples to collect per loop interval, and the final number of samples to collect. The sampling rate per second and the number of samples per loop interval are both set to one, such that one sample is collected every second. Thus to collect samples over 3 minutes, the final number of samples must be set to 180. For these measurements the lock-in amplifier was set to a time constant of 300 ms.

Chapter 4 will discuss the experiments conducted to measure the filling time and efficiency of the HC PBGs with acetylene gas. While these experiments were conducted using the ‘Pressure vs time.vi’ program, the voltage being recorded was read out from the pressure gauge rather than the lock-in amplifier. In accordance with the liquid phase experiments, the sampling rate was set to 1 sample per second and the total running time in seconds was entered into the front panel.

3.6 Equipment Used

Optical Components

Tunable diode laser (Ando, AQ 4320 D) 1520-1620 nm range

Erbium doped fiber amplifier (Keopsys, OI-BT-C-18-Sd-B-GP-FA)

Optical spectrum analyzer (Anritsu, MS9710C) 600-1750 nm range

Lock-in Amplifier (Stanford Research Systems, SR830) 0.001 Hz – 102.4 kHz range

DAQ (Measurement and Computing, USB-1408FS)

GPIB-USB connector (National Instruments, GPIB-USB-HS, 778927-01)

Narrow tunable band-pass filter (Newport, TBF-1550-1.0) 3.0 dB insertion loss, 1535- 1565 nm range, 0.3 dB at 1535 nm polarization loss.

Polarization controller (Thorlabs, FPC030)

Optical Fibers (Corning, SMF 28e+) 0.19-0.20 dB/km max attenuation at 1550 nm

Hollow-core photonic bandgap fibers (NKT Photonics, HC-1550-04 PCF) $10.6 \pm 0.3 \mu\text{m}$ core diameter, $4.1 \pm 0.1 \mu\text{m}$ pitch, $1535 \pm 5 \text{ nm}$ center wavelength, $<15 \text{ dB/km}$ max attenuation at 1550 nm

Gases

Acetylene gas (PRAXAIR, noncertified standard grade) 1000 ppm C₂H₂ in He

Liquid Phase Materials

Ammonium hydroxide (Sigma-Aldrich, ACS grade) 28.0-30.0% NH₃ by weight

Benzylamine (aminotoluene), C₆H₅CH₂NH₂ (Sigma-Aldrich, 99%)

LabVIEW Programs

Single peak scans.vi – Steps the laser across a user defined wavelength range and records the phase shift after each step.

Pressure vs time.vi – Records the voltage from the DAQ in time increments defined by the user – this program may be used to record the phase shift during liquid phase measurements or the pressure from a pressure gage.

Chapter 4

Results and Discussion

In this chapter the characteristics of the optical system with respect to the three different sensor interfaces will be discussed. Results of measurements taken with the interfaces will be displayed and there will be a brief discussion on experimental improvements. A detailed explanation of experimental improvements is given in Chapter 5.

4.1 The Experimental Setup with the Gas Cell Interface

4.1.1 Optimization at 1550 nm

Upon insertion and alignment of the gas cell we were able to achieve ring-down times of approximately 200 μs at 1550 nm (Figure 31) using time-domain measurements

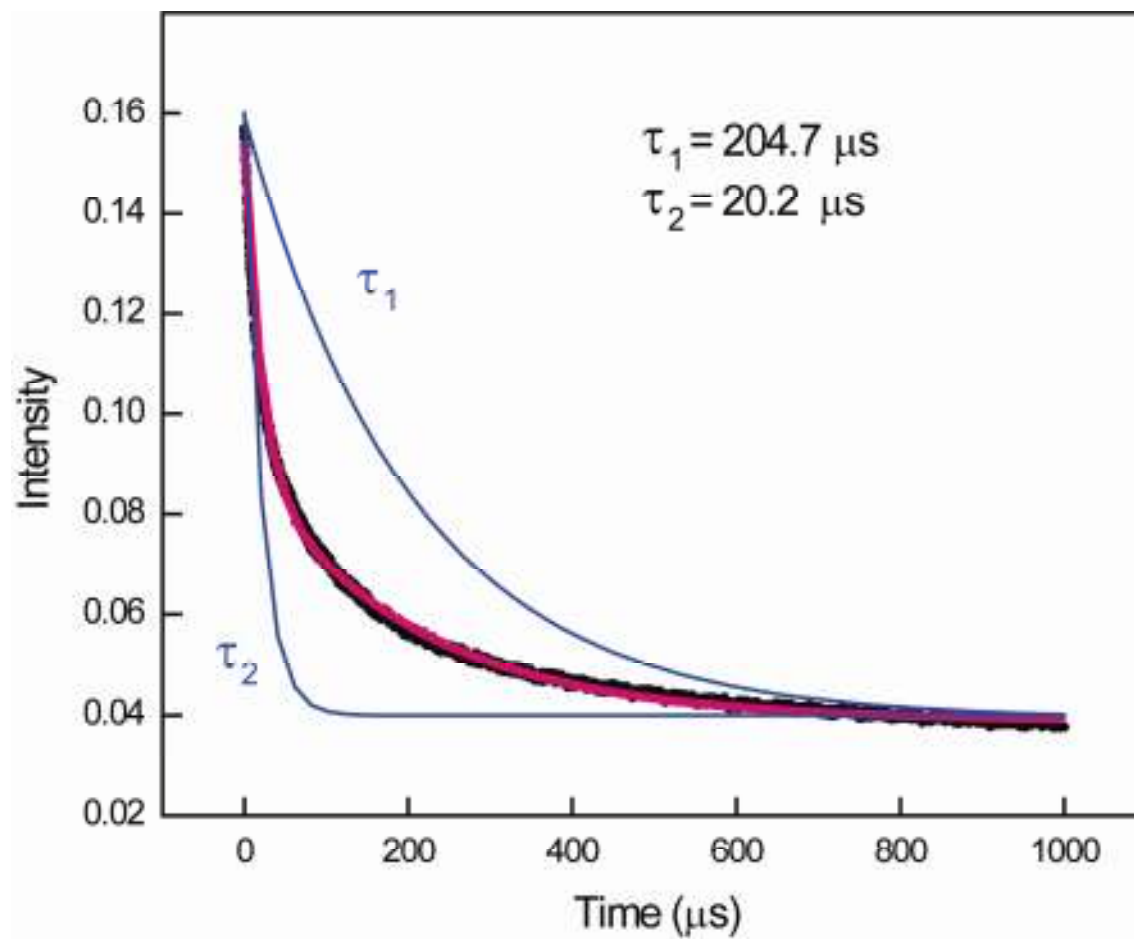


Figure 31. One of the highest ring-down times obtained with the gas cell as the sensor interface. The core of the fiber experienced a lifetime of $\sim 204.7 \mu\text{s}$, and the cladding had a decay time of $\sim 20.2 \mu\text{s}$.

We were able to measure the loop length and round trip time of the light by looking at the “steps” seen in Figure 32. The width of each step represents the time taken for light to make one round trip through the outer loop until it recombines with itself. By multiplying this step time by the speed of light in silica, we obtained the loop’s length (~ 155 m). The round trip time in this setup is ~ 750 ns and with a ring-down time of ~ 200 μ s, the effective absorption path of the setup is 16 m (i.e. an absorption enhancement by a factor of $16/0.06 = 267$) and round trip losses are 0.03 dB.

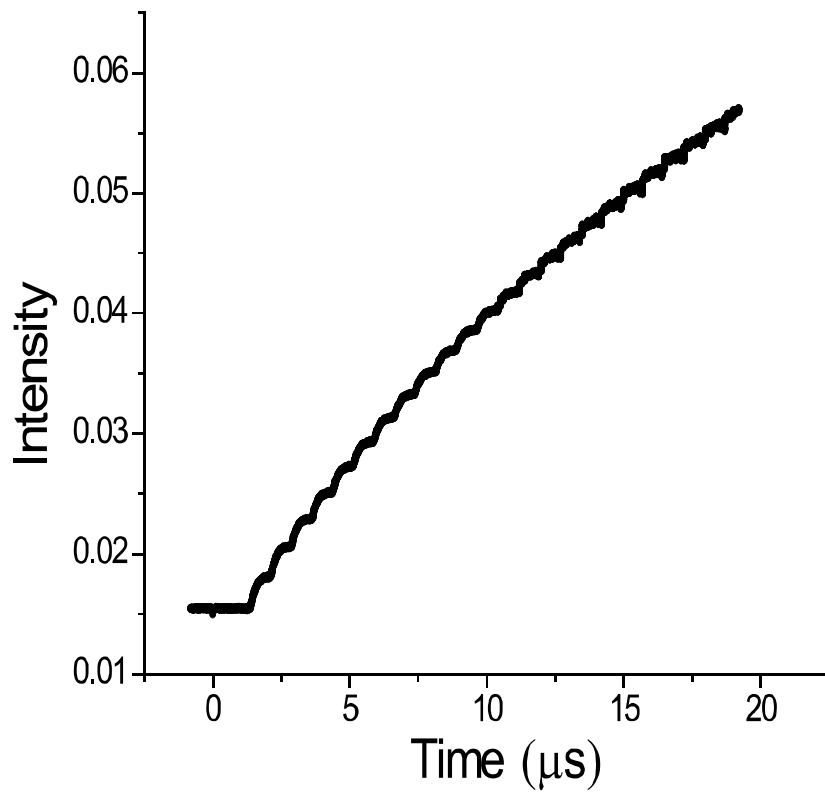


Figure 32. Ring-up trace of the outer-loop. The “steps” seen here are caused by the time it takes for light to travel once through the loop before it can recombine with itself and increase the loop intensity.

4.1.2 Optimization at 1530-1535 nm

At 1530-1535 nm, where both acetylene and ammonia absorb, ring-down times of ~ 30 - $50 \mu\text{s}$ were observed. Losses are increased by 1% (0.0174 dB) as a result of decreased transmission through the BPF and a reduction in gain, which can be seen in the erbium gain spectrum between 1530-1540 nm – thus the effective absorption path length is decreased to ~ 4 m. Additionally, an Allan variance plot was recorded such that the stability of the setup could be evaluated (Figure 33). One can see that the setup is mostly stable, with a slight fluctuation that was caused by a significant outlier (i.e. a very loud background noise caused by people in the same lab working on a different experiment).

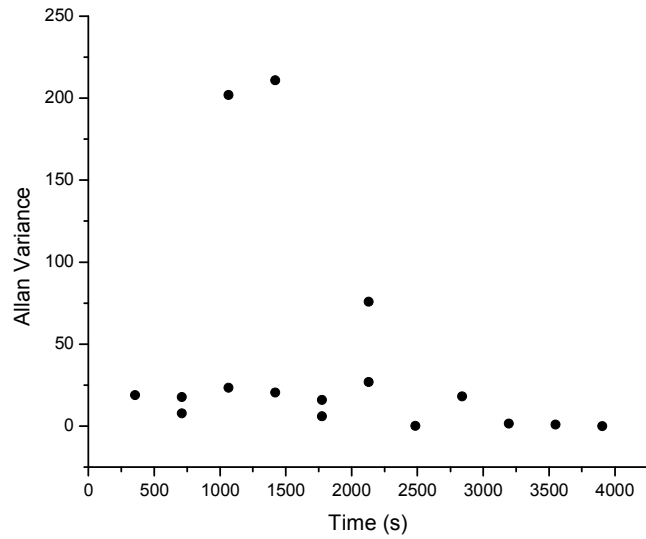


Figure 33. An Allan Variance plot - this shows the stability of the setup over time. The fluctuations in stability at $t \approx 1200$ were caused by exceptionally loud noises in the lab. Thus one can conclude that the experiment is stable under normal working conditions.

4.1.3 Relaxation Oscillations

Stewart and co-workers noted in their single loop experiments that the probe laser induced relaxation oscillations in the erbium when it neared coincidence with the lasing wavelength.⁶⁶ On the other hand, they were still able to record ring-down traces since these relaxations had a frequency of a few kilohertz and their amplitude decayed exponentially over a period of less than a few milliseconds. The same phenomenon was observed in our experiment when the gain in the outer loop approached the lasing threshold (Figure 34). Like Stewart et al.⁶⁶ we minimized the amplitudes of the oscillations by reducing the power of our TDL to 0.025 mW; however our time-domain traces were strongly distorted at the high gain levels needed. We overcame this problem by measuring absorption features using the phase shift cavity ring-down method, since the lock-in amplifier is then forced to record the phase shift only at the reference frequency and is therefore biased against the much smaller frequency of the relaxation oscillations. The gain in the outer loop was increased until the time trace on the oscilloscope became convoluted with relaxation oscillations, and then we run the phase shift LabVIEW program to record the optical loss of our sample loop. As far as we know, we are the first lab to record spectra in the gas and liquid phase using a nested loop form of amplified fiber loop ring-down spectroscopy.

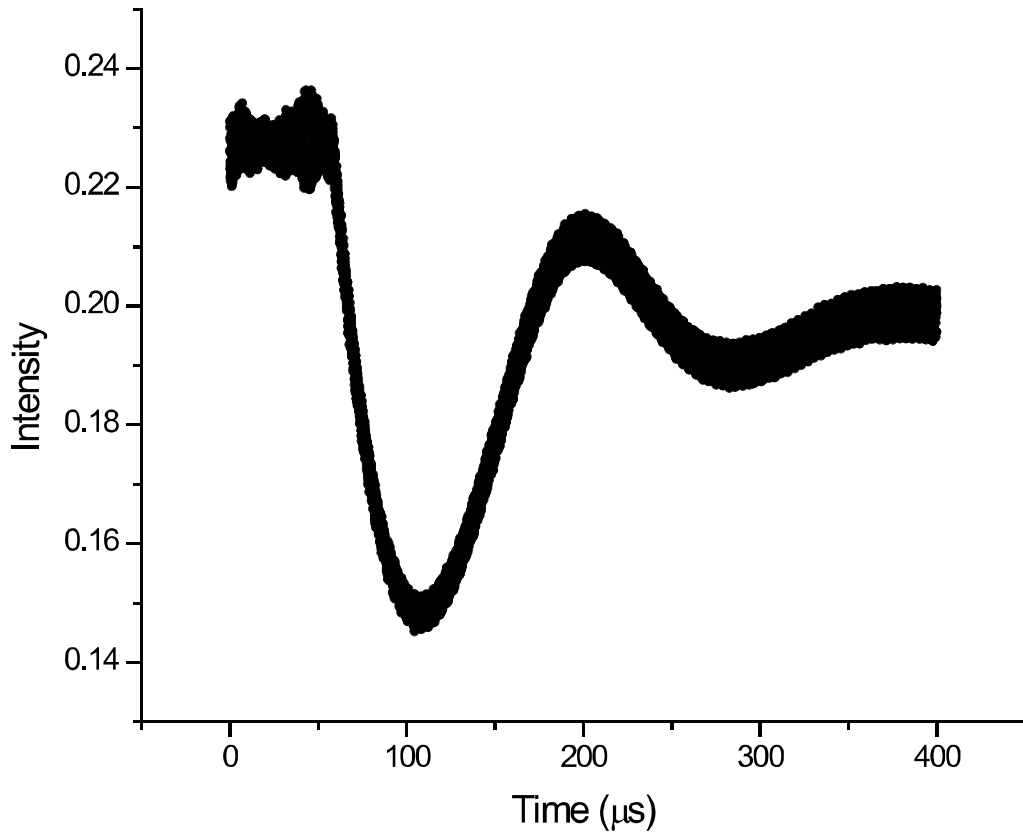


Figure 34. A relaxation oscillation seen in the outer loop. Similar to prior experiments by Stewart et al., the oscillation decays over a much greater period than the ring-down time.⁴⁷

4.1.4 Detection of Acetylene

Measurements were taken with the gas cell by setting the band pass filter over a known rotational transition taken from the HITRAN database (Figure 21). Figure 35 shows a spectrum of the P(11)-P(15) lines at 1000 ppm. The intensities of the peaks in this graph are not to scale with their actual intensities at ~ 298 K since the intensities of the measured transitions are a function of the ring-down times achieved at their respective wavelengths. P(11) should have the most intense peak but since it falls at the edge of the BPF (i.e. at the transmission minimum of the BPF) its intensity is reduced. Conversely, the ring-down time at P(15)'s wavelength was considerably higher than that of P(11), thus their intensities appear to be almost the same. Figure 36 (a) shows a close up of the P(13) line overlaid with a fit to a Voigt lineshape function. The Lorentzian contribution was calculated using a pressure broadening coefficient, b , that was experimentally determined by Arteaga et al.¹⁰⁵ - its relationship to the Lorentzian FWHM is shown in Equation 4.1.17 where p is the pressure. The Gaussian contribution was calculated using Equation 4.1.18, which expresses the FWHM due to Doppler broadening as a function of temperature, T , molar mass, M , and the central wavelength of the transition, λ_o . The Lorentzian and Gaussian contributions were calculated to be $\Delta\nu_L = 8.73 \times 10^{-2} \text{ cm}^{-1}$ and $\Delta\nu_D = 1.573 \times 10^{-3} \text{ cm}^{-1}$ respectively.

$$\Delta\nu_L = bp \tag{4.1.17}$$

$$\Delta\nu_D = 7.16 \times 10^{-7} \times \frac{c}{\lambda_o} \sqrt{\frac{T}{M}} \tag{4.1.18}$$

Figure 36 (b) shows the same spectrum; however, that has been iteratively fit with a Voigt lineshape. The Lorentzian contribution to this fit was $\Delta\nu_L = 1.0085 \times 10^{-1} \pm 1.84 \times 10^{-3} \text{ cm}^{-1}$, which is minimally higher than the calculated contribution. Conversely, the Gaussian contribution, $\Delta\nu_D = 2.259 \times 10^{-2} \pm 4.88 \times 10^{-3} \text{ cm}^{-1}$, is found to be an order of magnitude higher than the calculated contribution. There are two reasons for this – the first being a slight shoulder on the peak, which is best seen in Figure 36 (a), caused by multimode effects in what should have been a single mode laser. The second explanation is that the collision broadening at 1 atmosphere dominates over any noticeable Doppler broadening. When the latter is the case the peak can be fit with a Lorentzian peak rather than a Voigt one. To verify this, the peak was fit with a Lorentzian curve and a FWHM of $0.10471 \pm 7.032\text{E-}4 \text{ cm}^{-1}$ and an R^2 value of 0.98358 was obtained. By comparison, the Voigt fit returned an R^2 value of 0.98363; thus they do not significantly differ from one another. In order to determine which explanation is correct these experiments could be conducted using a truly single mode laser or at lower total pressures such that one could see exactly when pressure broadening overshadows the Doppler broadening.

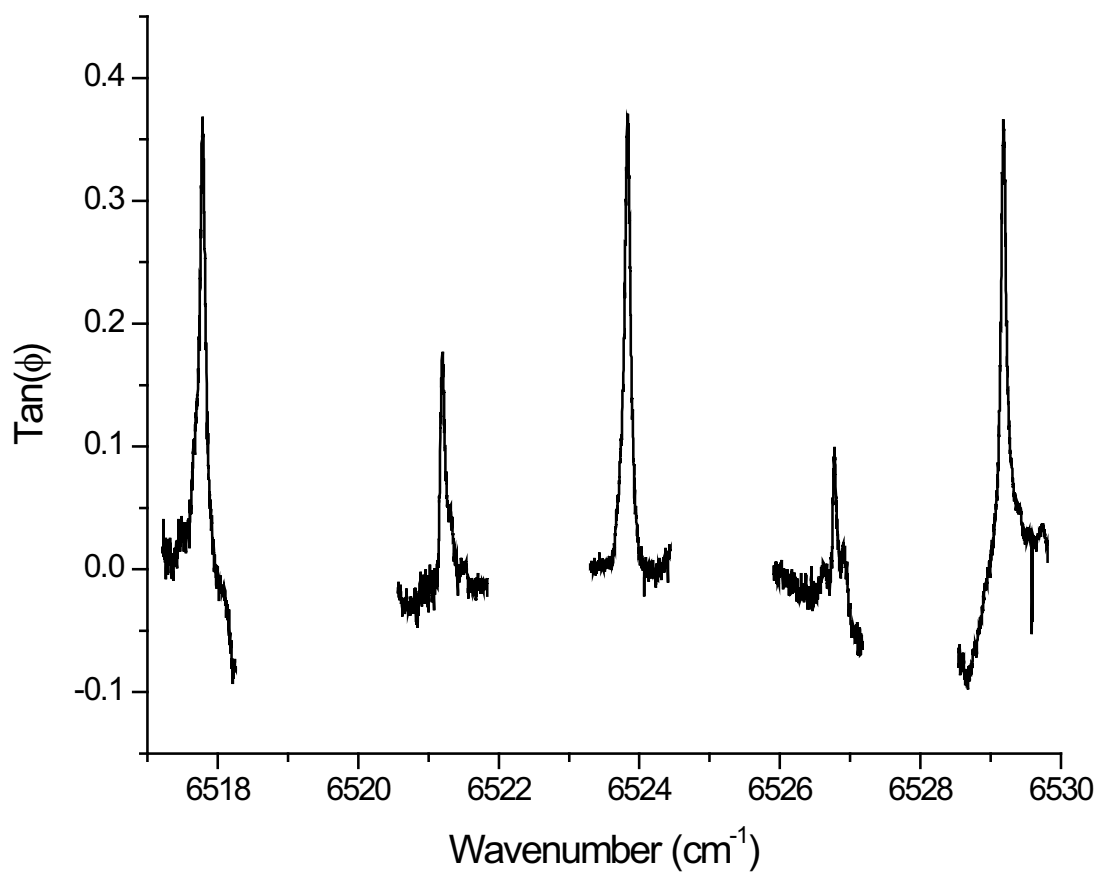


Figure 35. Spectrum of the acetylene P(11) – P(15) rotational lines on the $\nu_1+\nu_3$ combination band.

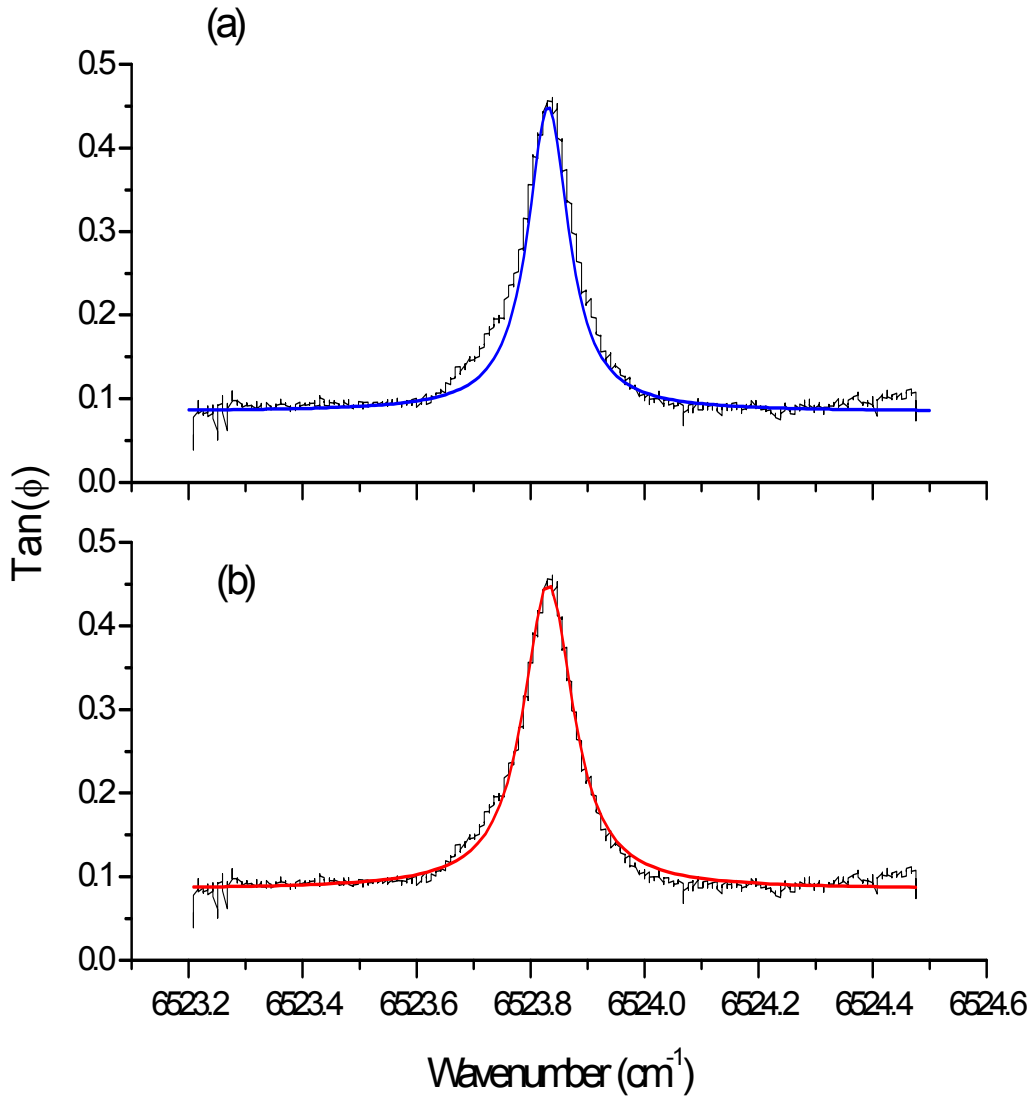


Figure 36. (a) The experimentally recorded P(13) line of acetylene at a concentration of 1000 ppm overlaid with a calculated Voigt lineshape in which $\Delta\nu_L = 8.73 \times 10^{-2} \text{ cm}^{-1}$ (i.e. 2.62 GHz) and $\Delta\nu_D = 1.57 \times 10^{-3} \text{ cm}^{-1}$ (i.e. 47.2 MHz) where each contribution was calculated from Equations 4.1.17 and 4.1.18 respectively. (b) The same experimentally recorded acetylene P(13) line with an iteratively fit Voigt lineshape. Here $\Delta\nu_L = 1.0085 \times 10^{-1} \pm 1.84 \times 10^{-3}$ (i.e. 3.0255 GHz) and $\Delta\nu_D = 2.259 \times 10^{-2} \pm 4.88 \times 10^{-3} \text{ cm}^{-1}$ (i.e. 677.7 MHz) was obtained by fitting.

Finally, absorption measurements of the P(13) line at different concentrations were taken down to pressures of 25 ppm (Figure 37). The measured detection limit of ~25 ppm is in good agreement with the calculated detection limit of 17 ppm (i.e. three times the standard deviation of the background noise).

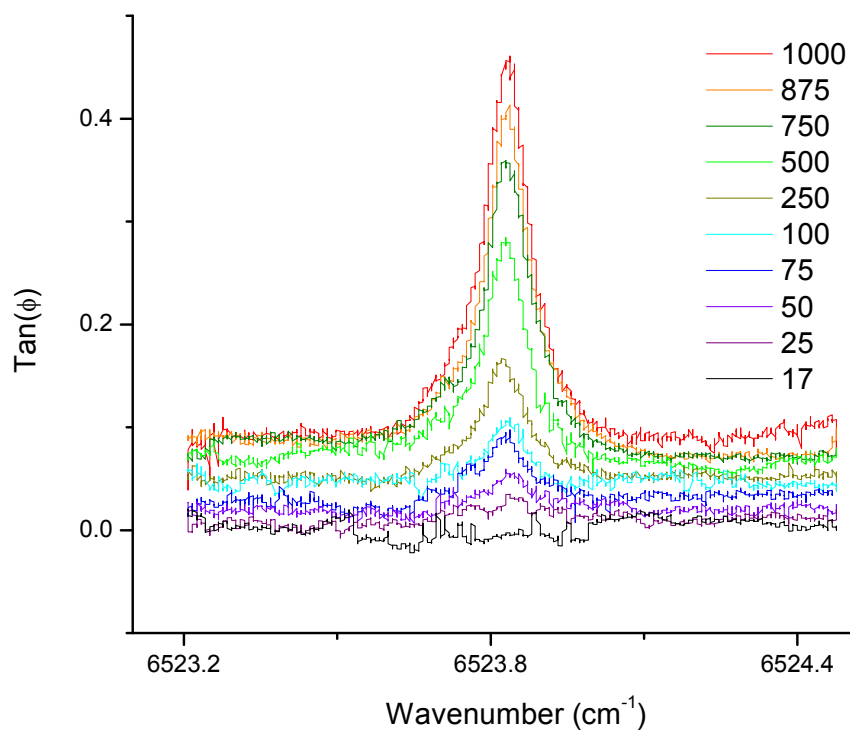


Figure 37. P(13) line taken at concentrations ranging from 1000 ppm to 17 ppm. The observed detection limit of 25 ppm is in good agreement with the calculated detection limit of 17 ppm.

4.1.5 Detection of Ammonia

Experiments were conducted using the same 6 cm gas cell as described above to measure ammonia at partial pressures ranging from 78.9 Torr to 5.9 Torr (i.e. $9.41 \times 10^4 - 7.7 \times 10^3$ ppm). We estimated a detection limit of 0.5 Torr, which is lower than the experimental detection limit of 5.9 Torr. The spectra are shown in Figure 38. The observed spectral lines were matched to the assigned, unassigned and calculated lines observed by Lundsberg-Nielsen et al. and Webber et al. in Figure 39.^{88,95} All of the peaks were in good agreement with the observed transitions; however, the suspected hot line was shifted with respect to the calculated wavelength by $\sim 0.01 \text{ cm}^{-1}$. To our knowledge this is the first observation of this transition, thus the error in its associated wavelength may be due to theory vs. experimental accuracy.

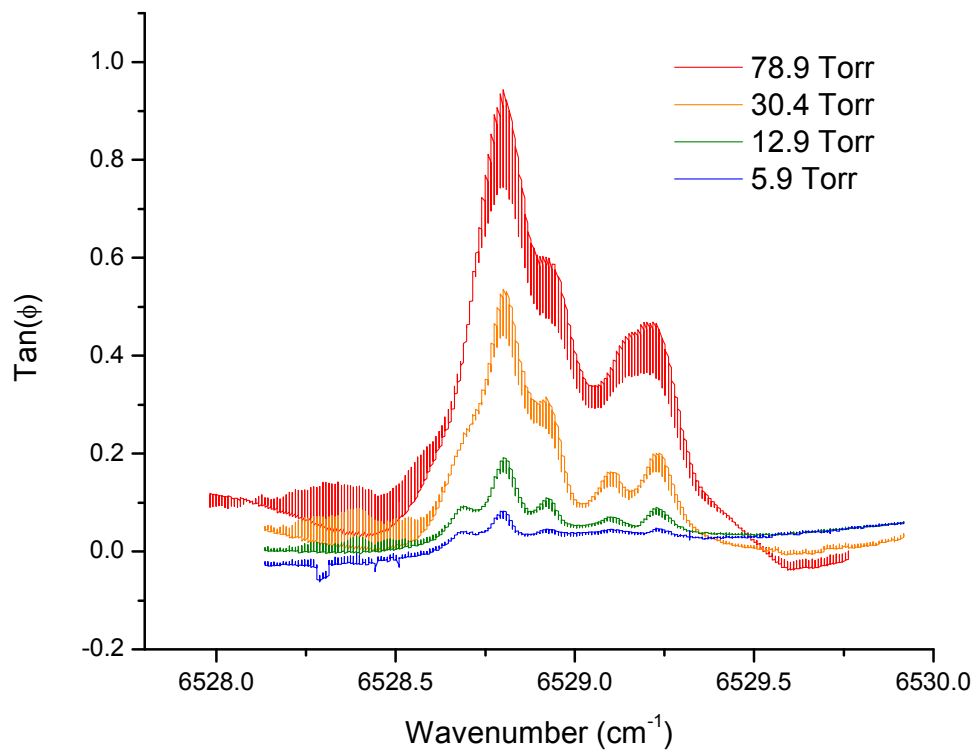


Figure 38. The ammonia $2\nu_3$ and $\nu_1+\nu_3$ lines at partial pressures between 78.9 Torr and 5.9 Torr. The experimental detection limit of 5.9 Torr is somewhat higher than the calculated detection limit of 0.5 Torr.

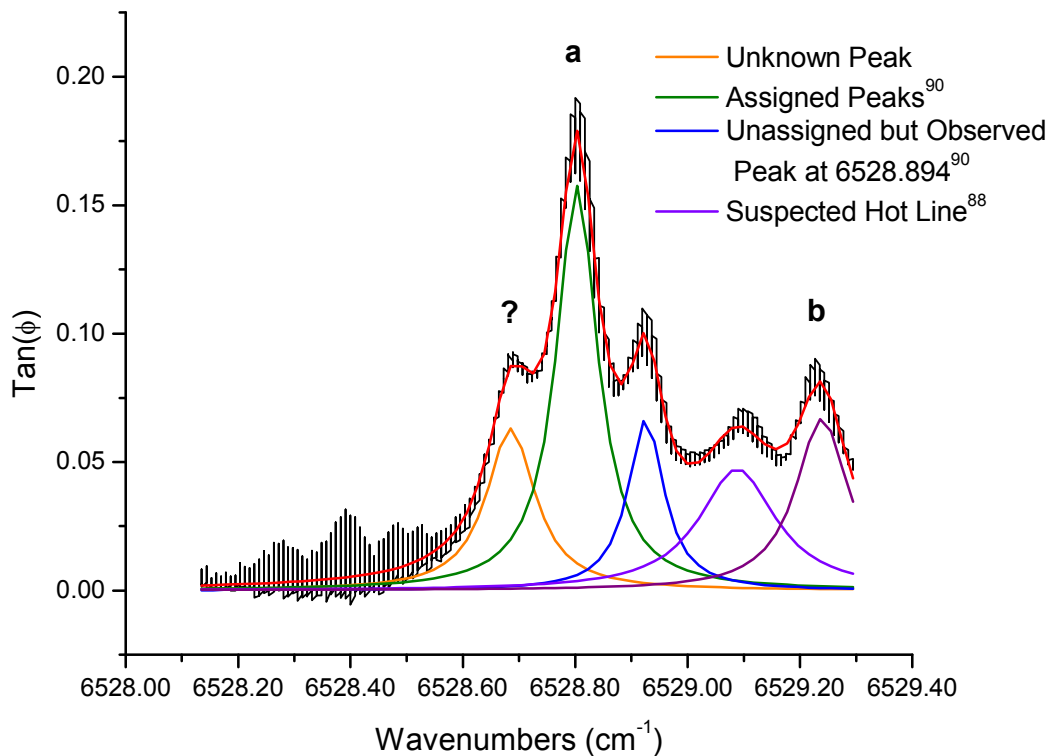


Figure 39. The fitted ammonia spectrum at 12.9 Torr. Peaks a and b correspond to the previously assigned peaks in Figure 22. The hot line is slightly shifted with respect to the calculated hot line wavelength, and two unassigned peaks were recorded at ~ 6528.64 and 6528.894 cm^{-1} .

4.2 The Experimental Setup with the Hollow-Core Photonic Band-Gap Sensor

Two different versions of the interface between the nested amplified fiber loop ring-down setup with HC PBGs were made.

4.2.1 The Initial HC PBG Interface

In the first interface, light was coupled from the single mode fiber (Corning SMF-28) to the HC-PBG fiber by aligning them using an x-y-z-translation stage and sealing the aligned assembly in a gas-tight adapter. Both the single mode fiber and the HC PBG were cut using a guillotine fiber cleaver. Each HC PBG to single-mode fiber interface was sealed in its own gas tight chamber with a valve connecting the two compartments (Figure 40). One chamber was connected to a membrane pump and the other to a gas inlet valve. Although the insertion losses were 8.34 dB, ring-down times of $\sim 20\text{-}25\ \mu\text{s}$ were recorded at 1532.83 nm. We performed a number of tests to determine whether detectable amounts of acetylene gas had entered the fiber.

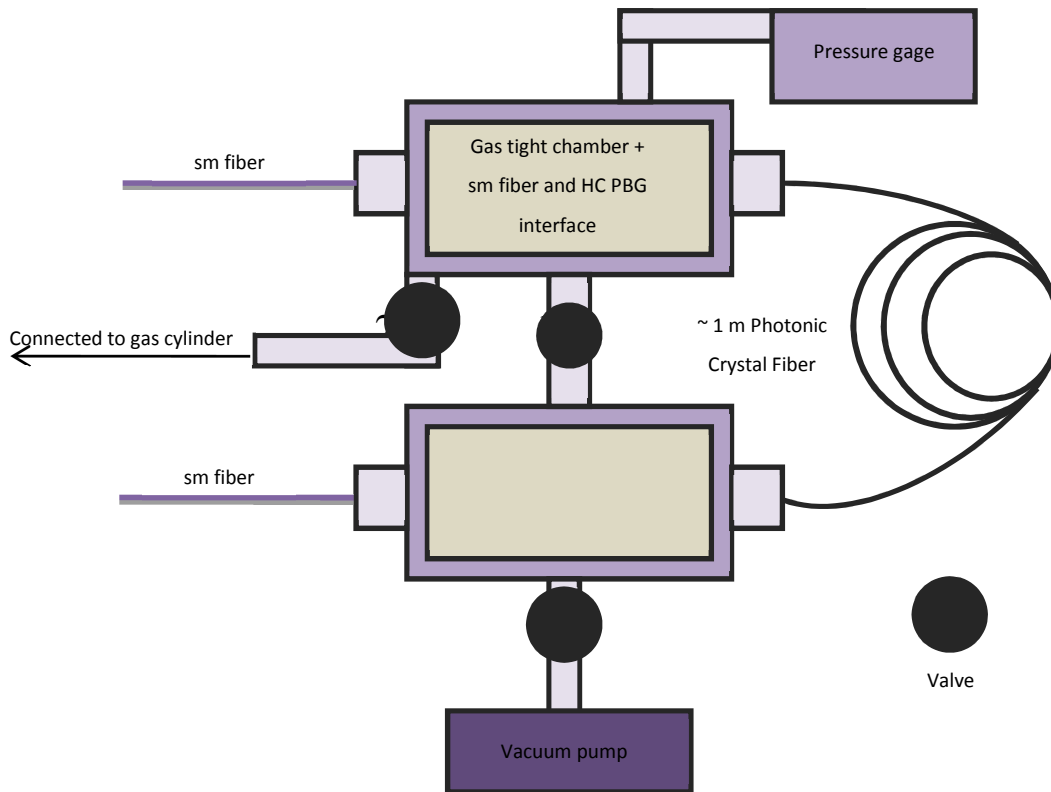


Figure 40. The first HC PBG – SMF28 interface. The ends of the ~ 1 m of HC PBG were coupled to conventional SM fiber in each of the gas tight chambers. A vacuum pump was able to lower the pressure in the chambers down to ~1.7 Torr, and a needle valve with a line connected to the gas cylinder on the top chamber allowed for gas to be added to the system. The chambers could be separated by closing the valve between them, thereby forcing any gas in them to travel through the HC PBG.

Initially, both chambers were evacuated to 1.7 Torr, the BPF was detached from the outer loop, and the nested loops were removed from the EDFA input connector. This enabled us to view the broadband spontaneous emission from the EDFA after it had done a single pass through the HC PBG on the OSA. From this we could see that the spontaneous emission spectrum of the EDFA had changed with respect to the transmission maximum of the HC PBGs (Figure 41).

Thereafter, we attempted to fill the HC PBG with acetylene using two different techniques. The first method involved opening the connecting valve between the two chambers and pumping both chambers down to 1.7 Torr - we continued to pump the chambers overnight in an attempt to completely evacuate the fibers. Afterwards, both chambers were filled to ~ 800 Torr with 1000 ppm of acetylene in helium and the OSA was monitored over different time intervals, the maximum being two days, for the appearance of any absorption lines; unfortunately, none were observed. This experiment was repeated with a slight alteration; after evacuating both chambers to 1.7 Torr, valve 1 was closed, thus only the first chamber was filled to ~ 800 Torr. Valve 2 was left open such that the vacuum pump could help the acetylene diffuse through the HC PBG into the second chamber. Once again the OSA was monitored for the appearance of the $\nu_1+\nu_3$ combination band, however it was not observed. More so, we recorded a decrease of 33 Torr in the first chamber after the first 13 hours and after ~ 72 hours a final change of ~ 150 Torr. Since the pressure change was minimal over long time spans we performed a similar test to check for leaks over 13 hours by evacuating both chambers down to 1.7 Torr, closing all the valves and measuring any increase in pressure. The results of these experiments concluded that while there was a small leak in the system, it would only have increased the pressure in the first chamber by a few Torr, therefore it was not enough to account for the minimal drop in pressure seen over the experimental time span. From these experiments we concluded that if any acetylene was entering the fibers it was not at a detectable concentration and that this was likely due to damage and clogging of the central hole in the HC PBG.

The cleaved surface of HC PBGs is susceptible to clogging from any dirt particulates flowing into or already existing in the chamber, it damages easily if it encounters any other

surface, and the act of splicing the fiber can distort the pitch or collapse the central hole (Figure 42). Currently, the recommended method for cleaving fibers is to use a guillotine fiber cleaver, since no special HC PBG cleavers are commercially available.

4.2.2 The Second HC PBG Interface

For a second version of the interface between SMF-28 and HC-PBG fiber, we experimented with using a focused ion beam (FIB) to cleave a HC PBG and found this method to be more successful. Figure 43 shows that the FIB made a clean cleave, with the exception of the bottom pitch holes, which were filled with sputter. While a superficial clogging of the pitch holes should not affect the fiber's transmission or ability to be filled with gas, this problem can be circumvented by using the FIB on the end of an already cleaved fiber, thus preventing sputter from collecting between the two ends. The shortcoming of this technique is the time it takes to cleave through the HC PBG. This experiment took approximately 13-15 hours to complete, but has the potential to be completed in 8-9 hours now that we know which aperture to use and to cleave the fiber at its ends.

While the FIB results were promising, due to their time consuming nature a guillotine fiber cleaver was used to cut the fiber ends, however special care was taken to ensure that the fiber ends did not touch anything before and after they were threaded through the ceramic ferrule. The new sensor interface had transmission losses of 4.81 dB and achieved ring-down times of approximately 15-20 μ s at 1532.83 nm. Once again, we attempted to measure the acetylene spectrum using single pass absorption spectroscopy, however none was observed. In this case we believe that gas had entered the fibers, just not at a high enough concentration – this

may be because the interface losses were too high to measure 1000 ppm of acetylene. The reason we believe this is because the background phase shift measurements were reproducible before and after the fiber was filled with gas, whereas the filled fiber induced a different phase shifts at wavelengths that are not part of the P(13) line. We can attribute this to slight movements and increased tensions in the filled fiber altering the outer loop losses, thus resulting in different phase shifts. If no gas was entering the fiber, this phenomenon would not occur. To rectify this problem Dr. Jack Barnes and Camiel van Hoorn (exchange student from Vrije Universiteit Amsterdam) are currently rebuilding the interface with a 19 μm core diameter HC PBG to increase its transmission and gas volume. In addition, we intend to use higher concentrations of acetylene.

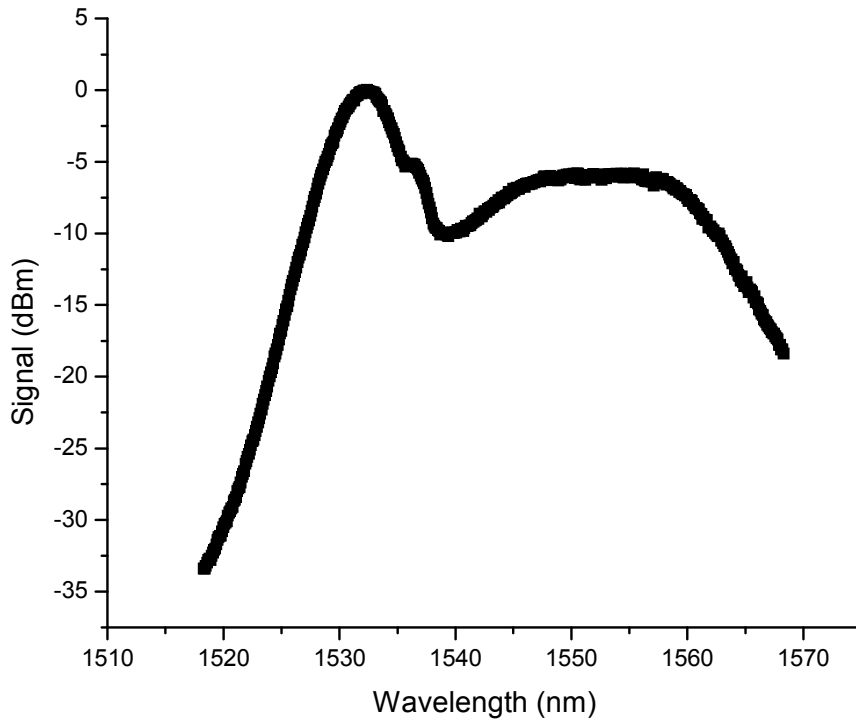


Figure 41. The EDFA spontaneous emission curve when the HC PBG sensor is inserted in the outer loop. Transmission is highest at the transmission maximum of the fiber (~ 1535 nm), and transmission is damped at 1550-1560 nm where the EDFA spontaneous emission is most intense.

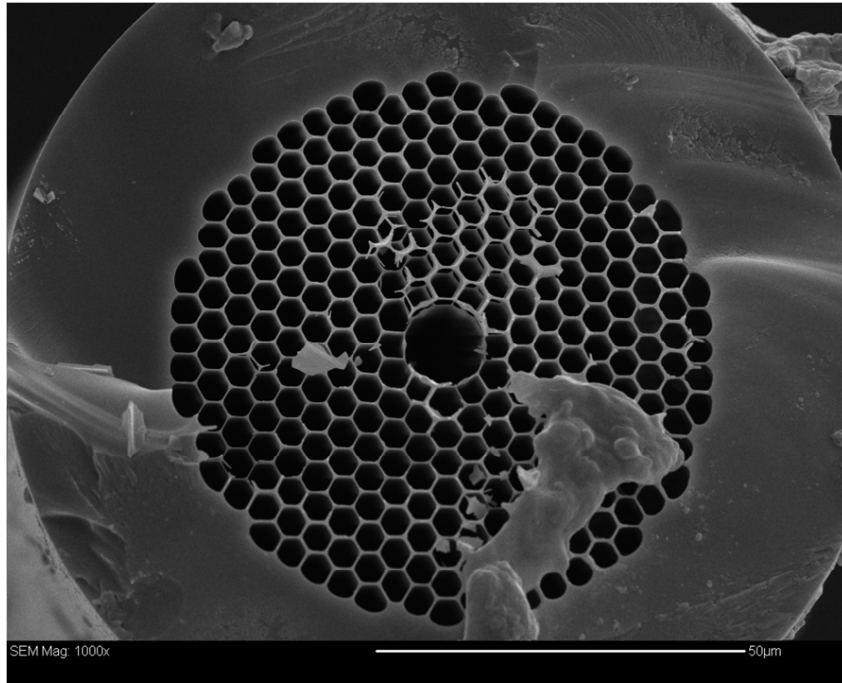
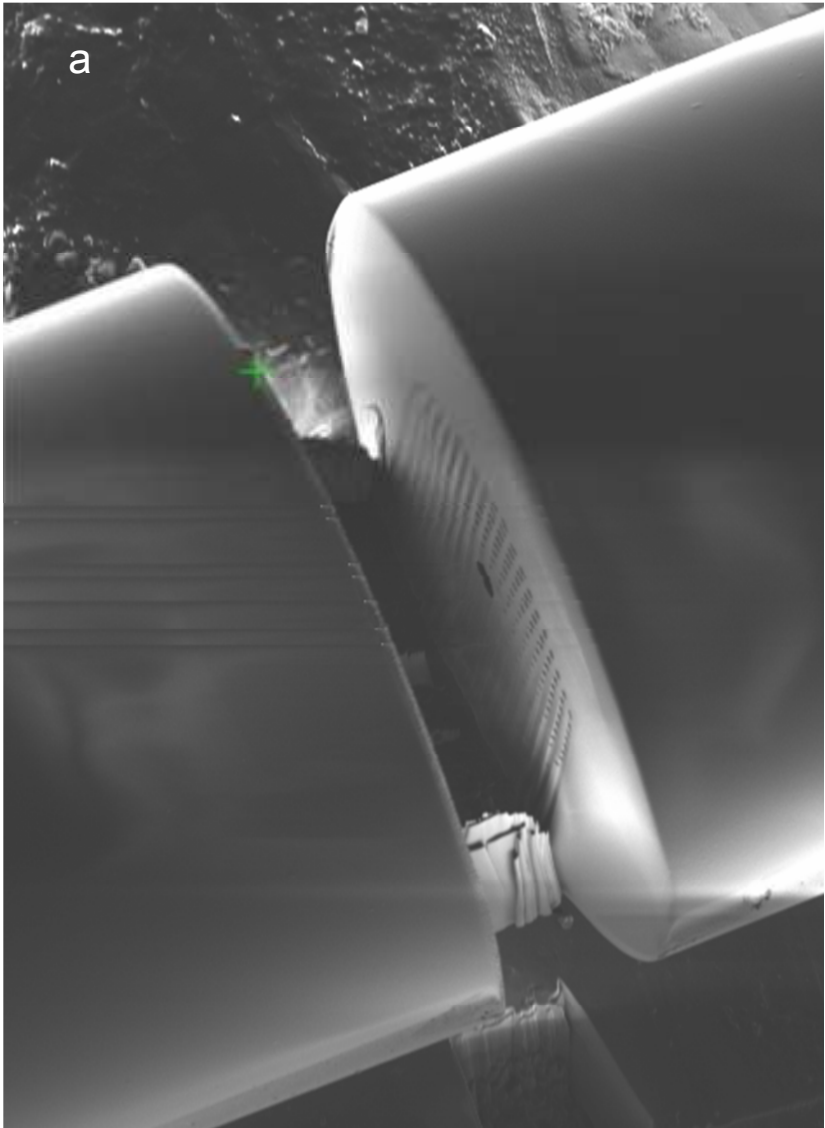


Figure 42. A HC PBG end that has been cleaved using a guillotine fiber cleaver. While in this case the center hole is unclogged, one can see debris blocking some of the small holes forming the cladding and the fiber is not uniformly cleaved.



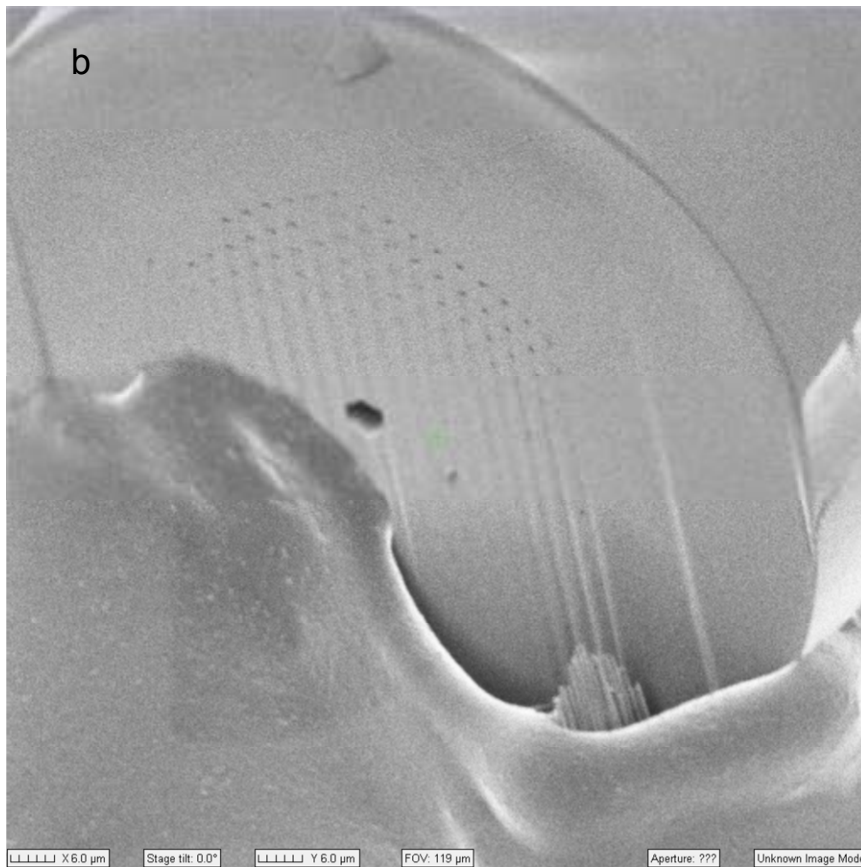


Figure 43. (a) The nearly cleaved HC PBG **(b)** The cleaved HC PBG on carbon tape, one can see that the center hole remains open while a lot of the small holes are clogged. This photo was taken after the HC PBG had been moved, so some of the clogging may be from damage caused by the carbon tape.

4.3 The Experimental Setup with the Fiber with a Hole Interface

The initial fiber-with-a-hole setup on the watch glass yielded the same ring-down times as the second setup in the Teflon trough at 1550 nm. In air, the ring-down time was approximately 60 μs ; in toluene decay times of $\sim 120 \mu\text{s}$ were recorded. The refractive index (RI) of toluene (1.496 at 20° C) is closer to that of silica (1.4601) than that of air (1.0003), thus explaining why light was transmitted more effectively through it.

Toluene was chosen as a background solvent since it has a similar RI to our sample, aminotoluene; it does not absorb strongly at 1550 nm; it is non-polar, thus it can be easily removed and will not stick to the silica. Unfortunately, the acrylate coating on the fibers dissolves easily in toluene so one must be cautious when handling the fibers since they become very delicate and brittle.

Aminotoluene (Also known as Benzylamine), is a clear to slightly amber liquid with a melting point of -10 °C and a boiling point of 182-185 °C (Figure 44). Its refractive index, 1.5430, is close to that of toluene. In our detection of picoliter volumes of liquid in a fiber that has been perforated by a cylindrical $\sim 30 \mu\text{m}$ hole we chose aminotoluene as our compound since N-H bonds exhibit a stretching vibration overtone near 1530 with an absorption coefficient of about $275 \text{ L mol}^{-1} \text{ cm}^{-1}$.^{46,106} In the liquid phase, this peak is broad with a FWHM spanning $\sim 50 \text{ nm}$.¹⁰⁶ We have chosen to look at the absorption of aminotoluene at 1550 nm ($\epsilon = 550 \text{ L mol}^{-1} \text{ cm}^{-1}$ at 1530 nm) since our experiment has recorded its longest ring-down times at this wavelength and because toluene does not absorb at this wavelength. Additionally, we chose an oxygen-free solvent because O-H groups show a small absorption in this range ($\sim 36 \text{ L mol}^{-1} \text{ cm}^{-1}$). Any

absorption found in our experiment can then be attributed to absorption of the aminotoluene sample.¹⁰⁶

4.3.1 The Watch Glass Setup

With the watch glass setup, we were able to record preliminary results since the open nature of the setup enabled the hole to be completely submerged in a pool of solvent. Air bubbles did not clog the hole, and there was a substantial amount of solvent on the watch glass - therefore evaporation did not affect the measurements. However, we needed to remove the brittle and stripped fibers from the glass when the aminotoluene was discarded. After breaking one fiber, the risk of breaking another was too great, so we designed the Teflon trough interface.

We saw that a 1% solution of aminotoluene yielded a substantial phase shift of $\sim 26^\circ$; thus, by assuming a linear relationship between concentration and phase shift, this phase shift was extrapolated down to the calculated phase shift at three times the standard deviation of the background noise. From here we calculated an estimated detection limit of a 0.10 % solution (Figure 45).

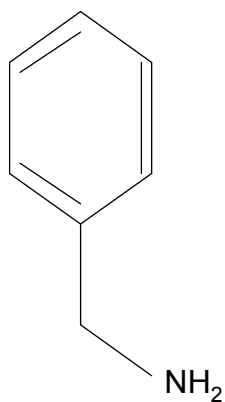


Figure 44. The chemical structure of aminotoluene (benzylamine).

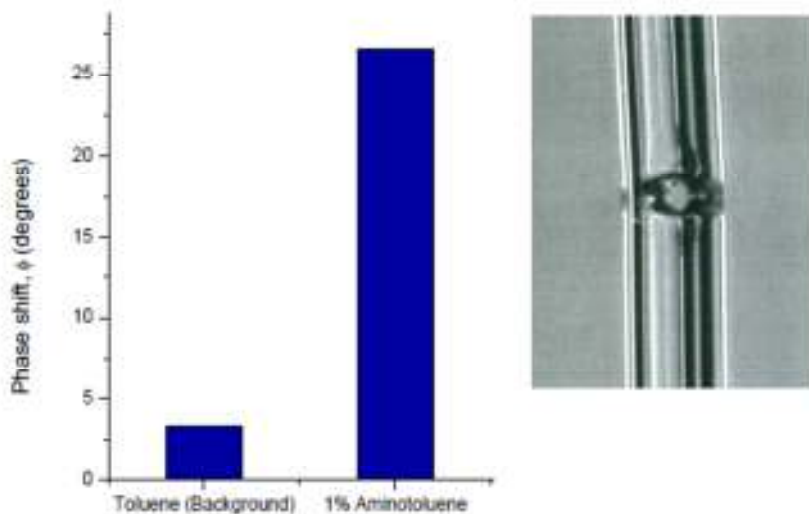


Figure 45. Preliminary results for the detection of a 1% solution of aminotoluene. From this, the predicted detection limit is a 0.10% aminotoluene solution.

4.3.2 The Teflon Trough Interface and Improvements

In comparison to the watch glass interface, the setup using the Teflon trough was better at facilitating the removal of chemicals; however, the fiber did not lay deep enough in the well to avoid effects of evaporation on the quantity of sample in the hole. Additionally, air bubbles were prominent in this setup, but were removed by placing a vibrating device on the interface.

For future experiments it would be beneficial to design an interface that would allow for flow measurements to be conducted – this would circumvent the effects of evaporation from volatile substances like toluene. More so, one can use the backing pressure on the flow inlet to force air bubbles and any precipitates out of the interface. Since the fiber is so delicate when it

has been stripped of its acrylate coating it may be beneficial to encase the fiber on either side of the hole in polymethyl methacrylate (PMMA) such that the hole remains exposed but the rest of the fiber will not break as easily when perturbed. Finally, an alternative to having the fibers manufactured by INO is desirable. At the present time Camiel van Hoorn, Dr. Andrew Brzezinski and Dr. Jack Barnes use the FIB to mill a hole in the fiber since it is a more cost effective option.

Chapter 5

Conclusion and Future Endeavours

In this chapter the optical setup in general and with respect to the three sensor interfaces used will be briefly summarized and improvements for the near and far future will be discussed.

5.1 The optical setup

In this thesis it has been shown that an amplified FLRD setup with consisting of two nested loops that share the same optical amplifier is a successful instrument for measuring the weak optical absorption of, both, gases and liquids in small volumes and with comparatively short absorption paths. One can see that the setup is readily adaptable to a variety of sensor interfaces – in this case a gas cell, HC-PBGs and a fiber with a hole. Although Stewart and coworkers have not reported their sensitivities for specific loop lengths in their two loop setup, they do mention that they obtained ring-down times on the order of several tens of microseconds. Their project was abandoned because it was thought to be too unstable.⁴⁷ Their single loop setup yielded impressive ring-down times of 200 μs in a 38 m loop (i.e. ~ 1100 round trips); however, reproducibility was difficult and none of their setups were stable enough to conduct their intended gas phase measurements.⁶⁶ While the two-loop setup described in this report suffers from lower sensitivity than Stewart and co-workers' instruments (i.e. $\tau=200 \mu\text{s}$ corresponds to ~ 267 round trips), it is stable over the course of hours - as verified using Allan Variance analysis - and generates reproducible results. Moreover, in Chapter 1 it was mentioned that Ni et al.⁶⁸ developed an amplified FLRD setup similar to that of Stewart and co-workers that included two 50:50 couplers, a tunable gain EDFA, a tunable narrow BPF, a VOA, and a NIST standard gas

cell. They reduced ASE noise and improved the accuracy of the experiments by using a digital least-mean-square filter that filters the ring-down event with an estimation of the noise, and uses the least-mean-square algorithm to improve its coefficients for noise estimation. This system was used to measure the P(11) line on the $\nu_1 + \nu_3$ combination band of acetylene and achieved a detection limit of 70.1 ppm. At the present time Ni and co-workers are the only other group to have measured chemical compounds using amplified FLRDS and it can be seen that the setup using two loops is able to achieve a lower detection limit compared to their single loop setup with noise reduction (i.e. 25 ppm for the weaker P(13) line on the acetylene $\nu_1 + \nu_3$ combination band).

One can decrease the detection limit of the current setup with respect to ammonia and acetylene by expanding the tuning range of the outer loop's narrow bandpass filter. The current BPF is centered at 1550 nm – a transmission maximum – while the water free ammonia lines and the intense region of the acetylene $\nu_1 + \nu_3$ combination band are located below 1535 nm – a transmission minimum. The specifications of the bandpass filter suggests that there is 0% transmission of light below ~ 1533 nm, however, 0% transmission is actually achieved at wavelengths below 1529 nm. Due to this wavelength restriction one may only sample a portion of the P-branch, thus a BPF centered at 1530-1535 nm would allow for one to sample a greater variety of rotational lines. Moreover, polarization dependent losses in the BPF increase as the wavelength approaches 1535 nm to a maximum of 0.3 dB, and sensitivity may therefore be increased by implementing a polarization controlling paddle after the 50/50 coupler in the inner loop. This would allow for a more stable gain clamping loop in the BPF transmission minimum, which is also a local minimum in the EDFA gain spectrum (i.e. Figure 16). Finally, to increase

the universal nature of this experiment it may be beneficial to switch the EDFA to a SOA such that compounds in the S, L and C bands can be detected at a considerably lower price and with a more compact setup. In general, compared to doped fiber amplifiers SOAs have a lower and noisier gain output but a smooth gain profile – unlike the homogeneously and inhomogeneously broadened EDFA gain spectrum. Theoretically the reduction in amplification should not affect the system as long as the inner loop has the ability to lase. The smoother gain profile will be beneficial for uniform sampling across a rotational spectrum, such that the line intensities correspond to the actual line strengths as opposed to the change in gain at each wavelength.

5.2 The Gas Cell

The initial sensor interface implemented in the two loop setup was a 6 cm long gas cell – this type of absorption cell was chosen since it could be used as a point of comparison to the setups developed by Stewart,^{47,66} Ni and coworkers.⁶⁸ At a wavelength of 1550 nm the maximum ring-down time achieved with the gas cell was approximately 200 μs – this corresponds to an effective path length through the 6 cm gas cell of 16 m, i.e. 266 passes until the intensity had decayed to 1/e of its initial value. At 1530-1535 nm, the ring-down times recorded ranged from 30-50 μs , corresponding to an effective path length of ~ 4 m. We were able to measure the acetylene P(11)-P(15) rotational transitions on the $\nu_1+\nu_3$ combination band down to an experimental detection limit of 25 ppm, which is in close agreement with the calculated detection limit of 17 ppm. Moreover, assigned and unassigned rotational lines on the ammonia $2\nu_3$ overtone and $\nu_1+\nu_3$ combination band were detected down to a partial pressure of 5.9 Torr, which was in relatively good agreement with the calculated detection limit of 0.5 Torr. The gas cell allowed us to determine if the nested loop setup was viable for detecting chemical compounds in the telecom region, thus we can conclude that the endeavour was successful. While the sensitivity of this interface pales in comparison to that of CRDS performed in a high finesse cavity, it is good for detecting small volumes of gas in relatively “high” concentrations without the easily dirtied optics. For example, this method may be used to monitor for source leaks of ammonia, methane, and/or formaldehyde sensing *in situ* or to study the breath of small creatures.⁹³

5.3 The HC-PBG fiber Interface

The second HC-PBG fiber interface that was constructed had only half of the transmission losses compared to the first interface; however, we have yet to detect the absolute presence of acetylene in the fibers. Currently, we are reconstructing the interface with HC-PBG fibers that have a 19 μm core diameter, as opposed to the current $\sim 10.1 \mu\text{m}$, since experiments conducted by other groups have had more success with larger core volumes.¹⁰⁷

Moreover, at the present time Camiel van Hoorn and Dr. Jack Barnes have successfully measured the acetylene $\nu_1 + \nu_3$ combination band at 1000 ppm in the 7 cell HC PBG using single pass absorption spectroscopy. They realised that although it is deemed ‘single-mode’ the HC PBG exhibits multiple core and cladding modes that interfere with one another. The interference effects result in an oscillating baseline but this was removed by attaching the fiber to a speaker and playing a tone such that the fiber was stretched and compressed. Since much of the interference pattern is dependent on the alignment of the SM fiber with the HC PBG, the sensor is very sensitive to vibrations, especially when coupled into the ring-down loop. As a result of this instability, it is not always possible to subtract the baseline from measurements and the noise levels are approximately ten times higher than those recorded with the gas cell. To rectify these issues they are currently looking into ways to make the experiment more stable – i.e. by reducing its exposure to vibrations, increasing the length of the HC PBG, using 19 cell HC PBGs, and finding a more stable way to couple the HC fiber to the SM fiber. Once this technique is improved it will have similar applications as the gas cell interface, however since it is theoretically a more sensitive technique it may be applied towards trace gas sensing in small volumes.

5.4 The Fiber with a Hole Interface

The very preliminary results recorded with the fiber with a hole interface showed great promise with a calculated detection limit of only 0.10% (1000 ppmv) aminotoluene solution and a phase shift of 26.2° (5.17×10^{-13} absolute moles). At present, we are attempting to construct more perforated fibers by milling conventional single-mode fibers with a focused ion beam. Once this task is completed, designing a flow interface where the fiber does not need to be submerged in the highly non-polar solvents would be optimal for achieving the expected detection limit while preserving the fibers integrity. In Chapter 4 it is mentioned that the fiber with a hole interface may be best suited to a flow system. In this type of setup one can use the interface in conjunction with separation techniques that require sensitive detection of small sample volumes (i.e. micro HPLC and capillary electrophoresis). This type of sensitivity is especially important for industries synthesizing new types of anti-cancer drugs where the final product is produced in limited quantities.¹²

5.5 Final comments

Overall one can see that amplified FLRDS using a nested two loop setup that shares the same optical amplifier is a stable and comparably sensitive technique to similar detection methods. The main advantage of this technique is its adaptability. It has been shown that one can detect compounds in both the gas and liquid phases using a gas cell and fiber with a hole, thus it theoretically can be modified to accommodate any sensor interface in the same way that passive FLRDS can. More so this setup has a large well of potential to be extended to new wavelength regions either by implementing SOAs or different RE³⁺ doped amplifiers. At the moment this technique is strictly designed for absorption measurements on small sample volumes, however the implementation of different amplifiers may change the gain and seeding dynamics seen in this setup. An amplifier that produces less ASE than the current EDFA would allow for increased sensitivity that will hopefully be comparable to mirrored CRDS in terms of detection limits.

References

- (1) Berden, G.; Engeln, R. *Cavity Ring-down Spectroscopy: Techniques and Applications*; Wiley, U.K., 2009.
- (2) Atkins, P.; de Paula, J. *Atkins Physical Chemistry*; 7th ed. Oxford University Press: New York, 2002.
- (3) Berden, G. Peeters, R.; Meijer, G. *International Reviews in Physical Chemistry* **2000**, *19*, 565-607.
- (4) Orr-Ewing, A. J. Cavity Ring-down Spectroscopy
<http://www.chm.bris.ac.uk/pt/ajoe/crds/crdintro.htm>.
- (5) Bescherer, K. Barnes, J. a; Dias, S. Gagliardi, G. Loock, H.-P. Trefiak, N. R. Waechter, H.; Yam, S. *Applied Physics B* **2009**, *96*, 193-200.
- (6) Huang, H.; Lehmann, K. K. *Optics Express* **2007**, *15*, 8745-8759.
- (7) Hodges, J. T. Looney, J. P.; van Zee, R. D. *The Journal of Chemical Physics* **1996**, *105*, 10278-10288.
- (8) Meijer, G. Boogaarts, M. G. H. Jongma, R. T.; Parker, D. H. *Chemical Physics Letters* **1994**, *217*, 112-116.
- (9) Herbelin, J. M. McKay, J. a; Kwok, M. a; Ueunten, R. H. Urevig, D. S. Spencer, D. J.; Benard, D. J. *Applied Optics* **1980**, *19*, 144-147.
- (10) Engeln, R. von helden, G. Berden, G.; Meijer, G. *Chemical Physics Letters* **1996**, *262*, 105-109.
- (11) Tong, Z. Wright, A. McCormick, T. Li, R. Oleschuk, R. D.; Loock, H.-P. *Analytical Chemistry* **2004**, *76*, 6594-6599.
- (12) Waechter, H. Bescherer, K. Dürr, C. J. Oleschuk, R. D.; Loock, H.-P. *Analytical Chemistry* **2009**, *81*, 9048-9054.
- (13) Hallock, A. J. Berman, E. S. F.; Zare, R. N. *Analytical Chemistry* **2002**, *74*, 1741-1743.
- (14) Anderson, D. Z. Frisch, J. C.; Masser, C. S. *Applied optics* **1984**, *23*, 1238-1245.

- (15) O'Keefe, A.; Deacon, D. A. G. *Review of Scientific Instruments* **1988**, *59*, 2544-2551.
- (16) Romanini, D. A, K. A. Sadeghi, N.; Stoeckel, F. *Chemical Physics Letters* **1997**, *264*, 316-322.
- (17) Romanini, D.; Lehmann, K. K. *The Journal of Chemical Physics* **1993**, *99*, 6287-6301.
- (18) Romanini, D.; Lehmann, K. K. *The Journal of Chemical Physics* **1995**, *102*, 633-642.
- (19) Scherer, J. Voelkel, D. Rakestraw, D. J. Paul, J. B. Collier, C. P. Saykally, R. J.; O'Keefe, A. *Chemical Physics Letters* **1995**, *245*, 273-280.
- (20) Pearson, J. Orr-ewing, A. J. Ashfold, M. N. R.; Dixon, R. N. *J. Chem. Soc., Faraday Trans.* **1996**, *92*, 1283-1285.
- (21) Zalicki, P. Ma, Y. Zare, R. N. Wahl, E. H. Dadamio, J. R. Owano, T. G.; Kruger, C. H. *Chemical Physics Letters* **1995**, *234*, 269-274.
- (22) Kotterer, M. Conceicao, J.; P, M. J. *Chemical Physics Letters* **1996**, *259*, 233-236.
- (23) Hodges, J. T. Looney, J. P.; van Zee, R. D. *Applied Optics* **1996**, *35*, 4112-4116.
- (24) Martin, J. Paldus, B. A. Wahl, E. H. Owano, T. G. Harris Jr, J. S. Kruger, C. H.; Zare, R. N. *Chemical Physics Letters* **1996**, *258*, 63-70.
- (25) Romanini, D. Kachanov, A. A.; Stoeckel, F. *Chemical Physics Letters* **1997**, *270*, 538-545.
- (26) Schulz, K.; Simpson, W. R. *Chemical Physics Letters* **1998**, *297*, 523-529.
- (27) Duschinsky, F. *Z. Phys.* **1933**, *81*, 7-22.
- (28) Barnes, J. Carver, B. Fraser, J. M. Gagliardi, G. Looock, H.-P. Tian, Z. Wilson, M. W. B. Yam, S.; Yastrubshak, O. *Optics express* **2008**, *16*, 13158-13167.
- (29) Camparo, J. *Contemporary Physics* **1985**, *26*, 443-447.
- (30) Wieman, C. E.; Hollberg, L. *Review of Scientific Instruments* **1991**, *62*, 1-20.

- (31) Lakowicz, J. R. Gratton, E. Laczko, G. Cherek, H.; Linkeman, M. *Biophysical Journal* **1984**, *45*, 34a.
- (32) Tong, Z. Jakubinek, M. Wright, A. Gillies, A.; Loock, H.-P. *Review of Scientific Instruments* **2003**, *74*, 4818-4826.
- (33) Waechter, H. Litman, J. Cheung, A. H. Barnes, J. a; Loock, H.-P. *Sensors* **2010**, *10*, 1716-1742.
- (34) von Lerber, T.; Sigrist, M. W. *Applied Optics* **2002**, *41*, 3567-3575.
- (35) Gupta, M. Jiao, H.; O'Keefe, A. *Optics Letters* **2002**, *27*, 1878-1880.
- (36) Andachi, M. Nakayama, T. Kawasaki, M. Kurokawa, S.; Loock, H.-P. *Applied Physics B* **2007**, *88*, 131-135.
- (37) Kashyap, R. *Fiber Bragg Gratings*; Academic Press, Elsevier: San Diego, CA, 1999.
- (38) Brown, R. S. Kozin, I. Tong, Z. Oleschuk, R. D.; Loock, H.-P. *The Journal of Chemical Physics* **2002**, *117*, 10444-10447.
- (39) Wang, C. *Sensors* **2009**, *9*, 7595-7621.
- (40) Barnes, J. Dreher, M. Plett, K. Brown, R. S. Crudden, C. M.; Loock, H.-P. *The Analyst* **2008**, *133*, 1541-1549.
- (41) Wang, C.; Mbi, A. *Measurement Science and Technology* **2006**, *17*, 1741-1751.
- (42) Wang, C.; Scherrer, S. T. *Applied Optics* **2004**, *43*, 6458-6464.
- (43) Wang, C.; Scherrer, S. T. *Optics Letters* **2004**, *29*, 352-354.
- (44) Vogler, D. Lorencak, A. Rey, J. M.; Sigrist, M. W. *Optics and Lasers in Engineering* **2005**, *43*, 527-535.
- (45) Gagliardi, G. De Nicola, S. Ferraro, P.; De Natale, P. *Optics Express* **2007**, *15*, 3715-3728.
- (46) Trefiak, N. R. *Ringdown Spectroscopy in Optical Waveguides*, Queens University, 2007.

- (47) Stewart, G. Atherton, K. Yu, H.; Culshaw, B. *Measurement Science and Technology* **2001**, *12*, 843-849.
- (48) Atherton, K. Stewart, G.; Culshaw, B. *Proceedings of SPIE* **2002**, *4577*, 25-31.
- (49) Tarsa, P. B. Lehman, K. K.; Rabinowitz, P. In *ACS National Meeting in Boston, MA, USA*; 2002.
- (50) Tarsa, P. B. Rabinowitz, P.; Lehman, K. K. *Chemical Physics Letters* **2004**, *383*, 297-303.
- (51) Loock, H.-P. *Trends in Analytical Chemistry* **2006**, *25*, 655-664.
- (52) Foquet, M. Korlach, J. Zipfel, W. R. Webb, W. W.; Craighead, H. G. *Analytical chemistry* **2004**, *76*, 1618-1626.
- (53) Taylor, J. a; Yeung, E. S. *Journal of Chromatography* **1991**, *550*, 831-837.
- (54) Poppe, H. *Analytica Chimica Acta* **1980**, *114*, 59-70.
- (55) Chervet, J. P. Van Soest, R. E. J.; Ursem, M. *Journal of Chromatography* **1991**, *543*, 439-449.
- (56) Wang, T. Aiken, J. H. Huie, C. W.; Hartwick, R. a *Analytical Chemistry* **1991**, *63*, 1372-1376.
- (57) Petersen, J. Mogensen, K. B.; Kutter, J. P. *Electrophoresis* **2002**, *23*, 3528.
- (58) Lin, Y.-W. Huang, C.-C.; Chang, H.-T. *Analytical and Bioanalytical Chemistry* **2003**, *376*, 379-383.
- (59) Tseng, W.-L. Lin, Y.-W. Chen, K.-C.; Chang, H.-T. *Electrophoresis* **2002**, *23*, 2477-2484.
- (60) Xu, H. Shafer-Ray, N. E. Merkt, F. Hughes, D. J. Springer, M. Tuckett, R. P.; Zare, R. N. *The Journal of Chemical Physics* **1995**, *103*, 5157-5160.
- (61) Seetohul, L. N. Ali, Z.; Islam, M. *Analytical Chemistry* **2009**, *81*, 4106-12.
- (62) van der Sneppen, L. Ariese, F. Gooijer, C.; Ubachs, W. *Journal of chromatography A* **2007**, *1148*, 184-188.

- (63) Bahnev, B. van der Sneppen, L. Wiskerke, a E. Ariese, F. Gooijer, C.; Ubachs, W. *Analytical Chemistry* **2005**, *77*, 1188-91.
- (64) Tong, Z. No Title, Queens University, 2004.
- (65) Li, R. Loock, H.-P.; Oleschuk, R. D. *Analytical Chemistry* **2006**, *78*, 5685-5692.
- (66) Stewart, G. Atherton, K.; Culshaw, B. *Optics Letters* **2004**, *29*, 442-444.
- (67) Stewart, G. Shields, P.; Culshaw, B. *Measurement Science and Technology* **2004**, *15*, 1621-1628.
- (68) Ni, N.; Chan, C. C. *Measurement Science and Technology* **2006**, *17*, 2349-2354.
- (69) Ni, N. Chan, C. C. Chuah, T. K. Xia, L.; Shum, P. *Measurement Science and Technology* **2008**, *19*, 1-6.
- (70) Ni, N. Chan, C. C. Xia, L.; Shum, P. *IEEE Photonics Technology Letters* **2008**, *20*, 1351-1353.
- (71) Becker, P. C. Olsson, N. A.; R, S. J. *Erbium-doped fiber amplifier: Fundamentals and technology*; Academica Press: San Diego, CA, 1999.
- (72) Miniscalco, W. J. *Journal of Lightwave Technology* **1991**, *9*, 234-250.
- (73) Qian, L. *Experiment on Erbium-Doped Fiber Amplifiers*; Toronto, 1998.
- (74) Du, J.; Cormack, A. N. *Journal of Non-Crystalline Solids* **2005**, *351*, 2263-2276.
- (75) Desurvire, E. *Erbium-doped fiber amplifiers: Principles and Applications*; Wiley: New York, 1994.
- (76) Afify, N.; Mountjoy, G. *Physical Review B* **2009**, *79*, 1-12.
- (77) Marcus, M. A.; Polman, A. *Journal of Non-Crystalline Solids* **1991**, *136*, 260-265.
- (78) Yin, D. Schmidt, H. Barber, J.; Hawkins, A. *Optics Express* **2004**, *12*, 2710-2715.
- (79) Cregan, R. F. Mangan, B. J. Knight, J. C. Birks, T. A. Russel, P. S. J. Roberts, P. J.; Allan, D. C. *Science* **1999**, *285*, 1537-1539.
- (80) Knight, J. C. *Nature* **2003**, *424*, 847-851.

- (81) Temelkuran, B. Hart, S. D. Benoit, G. Joannopoulos, J. D.; Fink, Y. *Nature* **2002**, *420*, 650-653.
- (82) Muller, D. In *CLEO*; 2003; p. 2003.
- (83) Nakagawa, K.; Onae, A. *Proceedings of SPIE* **2001**, *4269*, 41-49.
- (84) Steinfeld, J. I. *Molecules and Radiation: An Introduction to Modern Molecular Spectroscopy*; Dover Repr. 2005.
- (85) Garland, C. W. Nibler, J. V.; Shoemaker, D. P. *Experiments in Physical Chemistry*; 7th ed. McGraw-Hill: New York, 2003.
- (86) Bernath, P. F. *Spectra of Atoms and Molecules*; Oxford University Press: New York, 1995.
- (87) Rothman, L. S. Gordon, I. E. Barbe, A. Benner, D. C. Bernath, P. F. Birk, M. Boudon, V. Brown, L. R. Campargue, A. Champion, J.-P. Chance, K. Coudert, L. H. Dana, V. Devi, V. M. Fally, S. Flaud, J.-M. Gamache, R. R. Goldman, A. Jacquemart, D. Kleiner, I. Lacome, N. Lafferty, W. J. Mandin, J.-Y. Massie, S. T. Mikhailenko, S. N. Miller, C. E. Moazzen-Ahmadi, N. Maumenko, O. V. Nikitin, A. V. Orphal, J. Perevalov, V. I. Perrin, A. Predoi-Cross, A. Rinsland, C. P. Rotger, M. Simeckova, M. Smith, M. A. H. Sung, K. Tashkun, S. A. Tennyson, J. Toth, R. A. Vandaele, A. C.; Vander Auwera, J. *Journal of Quantitative Spectroscopy and Radiative Transfer* **2009**, *110*, 533-572.
- (88) Webber, M. E. Baer, D. S.; Hanson, R. K. *Applied Optics* **2001**, *40*, 2031-2042.
- (89) Kar, S.; Arnold, M. a *Analytical chemistry* **1992**, *64*, 2438-2443.
- (90) Spear, S. K. Patterson, S. L.; Arnold, M. a *Analytica Chimica Acta* **1997**, *357*, 79-84.
- (91) Hancock, G. Peverall, R.; Ritchie, G. A. D. <http://ip.com/patent/US7300408> **2007**, 1-11.
- (92) Timmer, B. H. van Delft, M. Koelmans, W. W. Olthuis, W.; van den Berg, a *IEEE Sensors Journal* **2006**, *6*, 829-835.
- (93) van Herpen, M. M. J. W. Ngai, A. K. Y. Bisson, S. E. Hackstein, J. H. P. Woltering, E. J.; Harren, F. J. M. *Applied Physics B* **2006**, *82*, 665-669.
- (94) Kiprof, P. Molecular Vibrations
<http://www.d.umn.edu/~pkiprof/ChemWebV2/Vibrations/vib1.html>.

- (95) Lundsberg-Nielsen, L. Hegellund, F.; Nicolaisen, F. M. *Journal of Molecular Spectroscopy* **1993**, *162*, 230-245.
- (96) Perman, E. *J. Chem. Soc.* **1901**, *79*, 718-725.
- (97) Gilsdorf, R. W.; Palais, J. C. *Applied optics* **1994**, *33*, 3440-3445.
- (98) Henningsen, J. Hald, J.; Peterson, J. C. *Optics Express* **2005**, *13*, 10475-10482.
- (99) Cubillas, A. M. Hald, J.; Petersen, J. C. *Optics Express* **2008**, *16*, 3976-3985.
- (100) Cubillas, A. M. Lazaro, J. M. Silva-Lopez, M. Conde, O. M. Petrovich, M. N.; Lopez-Higuera, J. M. *Electronics Letters* **2008**, *44*, 5-6.
- (101) Marty, P. T. Morel, J.; Feurer, T. *Journal of Lightwave Technology* **2010**, *28*, 1236-1240.
- (102) Benabid, F. Couny, F. Knight, J. C. Birks, T. a; Russell, P. S. J. *Nature* **2005**, *434*, 488-491.
- (103) Thapa, R. Knabe, K. Corwin, K. L.; Washburn, B. R. *Optics Express* **2006**, *14*, 9576-9583.
- (104) Cournoyer, A. Antonov, D. Levesque, L. Cantin, D.; Levesque, M. *Proceedings of SPIE* **2004**, *5578*, 596-604.
- (105) Arteaga, S. W. Bejger, C. M. Gerecke, J. L. Hardwick, J. L. Martin, Z. T. Mayo, J. McIlhattan, E. a; Moreau, J.-M. F. Pilkenton, M. J.; Polston, M. J. *Journal of Molecular Spectroscopy* **2007**, *243*, 253-266.
- (106) Buback, M.; Vogele, H. P. *FT-NIR Atlas*; VCH Publishers: Weinheim, 1993.
- (107) Carvalho, J. P. Magalhães, F. Frazão, O. Santos, J. L. Araújo, F. M.; Ferreira, L. a *Solid State Phenomena* **2010**, *161*, 43-49.